

Symmetry-Aware Convex Shrinkage for High-Dimensional Covariance Estimation

Mitchell A. Thornton

Darwin Deason Institute for Cyber Security
Department of Electrical and Computer Engineering
Southern Methodist University, Dallas, TX, USA
mitch@smu.edu

Abstract

This paper develops a class of data-adaptive shrinkage estimators for high-dimensional covariance estimation in which the shrinkage target is a Reynolds projection of the sample covariance under a finite symmetry group selected from a candidate library by held-out predictive performance. The class generalizes the convex shrinkage estimator of Ledoit and Wolf, which targets a scalar multiple of the identity matrix, by replacing the identity target with a structured target derived from a symmetry group when one is available. It also generalizes the group-symmetric maximum-likelihood covariance estimator of Shah and Chandrasekaran by combining structural targeting with adaptive convex shrinkage and by selecting the group from data rather than treating it as prespecified. A two-tier procedure is developed for the group selection: a universal per-candidate evaluation based on held-out negative log-likelihood, optionally preceded by a domain-specific step that constructs the candidate library from structural priors of the data. A finite-sample regret bound is established for the held-out calibration of the convex combination weight; an oracle inequality is established for the data-driven group selection; and a quantitative sufficient-match condition is established under which the proposed estimator dominates Ledoit-Wolf shrinkage in Frobenius mean-squared error. The procedure is illustrated on six real-data covariance estimation problems whose candidate libraries are constructed from domain-specific structural priors: financial returns on the constituents of the Standard and Poor’s 500, sea surface temperature anomalies from the National Oceanic and Atmospheric Administration’s optimum interpolation product, gene expression covariances for breast invasive carcinoma from The Cancer Genome Atlas, intermediate-frequency radio signal covariances from the RadioML 2018.A benchmark, galaxy image covariances from the Galaxy10 DECaLS dataset, and natural image patch covariances from CIFAR-10 with a distribution-shift companion on CIFAR-10.1. The procedure is also empirically compared against the Bayesian permutation-symmetry estimator of Chojecki and colleagues. Outside the few-shot regime, where structural priors carry the most information per observation, Ledoit-Wolf shrinkage remains the appropriate baseline.

Keywords: covariance estimation, convex shrinkage, symmetry-aware regularization, Reynolds projection, finite-group invariance, algebraic diversity, high-dimensional statistics

1 Introduction

High-dimensional covariance estimation in the few-shot regime, where the sample size N is comparable to or smaller than the dimension M , is a core problem in multivariate statistics [Pourahmadi, 2013, Wainwright, 2019]. The sample covariance is rank-deficient and inadmissible in this regime;

in classical terms, its inadmissibility traces to Stein [1956], with covariance-specific shrinkage developed in Stein [1986], and the Marchenko and Pastur [1967] eigenvalue distribution making the high-dimensional distortion explicit [surveyed in Bai and Silverstein, 2010]. The standard remedy introduces regularization toward a structurally simple target, of which several variants exist [Dempster, 1972, Schäfer and Strimmer, 2005, Chen et al., 2010, Won et al., 2013]. The reference baseline for the present work is the convex shrinkage estimator of Ledoit and Wolf [2004],

$$\hat{\mathbf{R}}_{\text{LW}}(\alpha) = (1 - \alpha) \hat{\mathbf{R}} + \alpha \hat{\sigma}^2 \mathbf{I}, \quad \hat{\sigma}^2 = \frac{1}{M} \text{tr} \hat{\mathbf{R}}, \quad (1)$$

which combines the sample covariance with a multiple of the identity matrix at a data-determined convex weight controlled by the *shrinkage intensity* $\alpha \in [0, 1]$. The nonlinear-shrinkage descendants of this line, including Ledoit and Wolf [2012] and the analytical Marchenko-Pastur form of Ledoit and Wolf [2020], are surveyed in those references; (1) is retained here as the linear baseline, with the analytical nonlinear form treated separately below.

The identity target is the natural choice when no structural prior is available. In many applications, however, a structural prior is available in the form of a symmetry group acting on the index set, for instance from compositional, hierarchical, lattice, or combinatorial structure, and a target that respects this structure carries information that the identity target does not. Symmetry-aware covariance estimation has a fifty-year tradition originating with the Andersson [1975] irreducible-decomposition theorem for G -invariant covariance matrices, the Jordan-algebra perspective on the same of Jensen [1988], the lattice-conditional-independence extension of Andersson and Madsen [1998], and the graphical Gaussian models with symmetry constraints of Højsgaard and Lauritzen [2008]; the rate-optimality results of Lounici [2014] and Cai and Zhou [2012] for sparse-precision and sparse-covariance estimation occupy a parallel structural substrate not directly compared here. More recently, Shah and Chandrasekaran [2012] and Soloveychik et al. [2016] extend the invariant-Gaussian-models machinery into the high-dimensional covariance estimation regime; the algebraic decomposition machinery the present work rests on is exactly Andersson’s, specialized to representations over \mathbb{R} . The objective of the present work is to introduce a class of data-adaptive shrinkage estimators in which the target is a Reynolds projection of the sample covariance under a finite group, with the group selected from a candidate library by held-out predictive performance, building on the Algebraic Diversity (AD) framework of Thornton [2026b,a].

The principal past methods to which we compare are Ledoit and Wolf [2004] and Shah and Chandrasekaran [2012]. Ledoit and Wolf [2004] introduced a convex combination of the sample covariance with a target proportional to the identity, with the convex combination weight selected to minimize a Frobenius-loss risk. The estimator is well-conditioned, dominates the sample covariance in mean-squared error in many high-dimensional regimes, and is widely used. Shah and Chandrasekaran [2012] take an explicitly group-symmetric approach to covariance regularization, with the group G assumed known a priori and the estimator defined as the maximum-likelihood estimator within the commutant algebra subject to a determinantal regularizer. Although the convex regularizer described here may at first appear to be an extension of Ledoit and Wolf [2004] with a target influenced by Shah and Chandrasekaran [2012], it differs from such a simple substitution in several respects.

First, the target is the projection of the sample covariance onto the commutant of a finite group, which produces a positive-semidefinite estimator on the same scale as the sample covariance and is therefore suitable as a shrinkage target; the penalized estimator of Shah and Chandrasekaran [2012] is not on the same scale and does not enter a convex shrinkage form directly. Second, the candidate library is broadened from a single fixed linear action to admit direct products, wreath products, and semidirect products of finite groups [for the wreath construction see James and Kerber,

1981, Chapter 4], which arise naturally in real data with hierarchical or compositional symmetry. Third, the symmetry group is selected from data rather than assumed known, by way of a two-tier Best-Matched Group (BMG) procedure described in Section 2 that is intended to be fast, efficient, and accurate in the few-shot regime; this is the principal practical enabler since most applications do not come with a prespecified group. The empirical comparisons in Section 4 use the BMG-selected group as the input to the Shah comparator (denoted Shah-BMG), so that the comparison evaluates the Shah-style $\alpha = 1$ projection-only estimator against the AD-style calibrated $\alpha \in [0, 1]$ estimator at the same target, on a level methodological playing field; the BMG group-selection is itself an extension of Shah and Chandrasekaran [2012]’s framework, which assumes the group as input. Fourth, two natural calibrations of the shrinkage intensity are studied side-by-side: a closed-form Frobenius mean-squared-error plug-in and a held-out negative-log-likelihood (NLL) minimizer. Their respective regions of preference are characterized in Section 3.

A separate line of recent work, the `gips` R package of Chojecki et al. [2025] implementing the Bayesian model-selection procedure of Graczyk et al. [2022], also addresses learning permutation symmetries in Gaussian covariance from data [building on the broader group-representation-in-statistics program surveyed by Diaconis, 1988]; the present work differs from `gips` in three respects that together place the two methods in adjacent rather than overlapping methodological territory. First, the search space differs: `gips` searches over cyclic subgroups of the symmetric group S_p via Metropolis-Hastings on S_p , whereas the candidate library \mathcal{G} used here is a small, hand-curated set of physically motivated groups including direct products, wreath products, and semidirect products of finite groups (the wreath products in particular do not lie in the cyclic-only search space). Second, the selection paradigm differs: `gips` maximizes a Bayesian posterior with a Diaconis-Ylvisaker conjugate prior on the precision parameter, whereas the present procedure minimizes held-out cross-validated NLL across a tractable candidate set; the two paradigms have different small-sample behavior and different requirements on the sample size. Third, the estimator at the selected group differs: `gips` uses the projection MLE under the symmetry constraint, equivalent to a Shah-style $\alpha = 1$ projection-only estimator, whereas the present procedure produces a shrinkage estimator at calibrated $\alpha \in [0, 1]$ that adapts the bias-variance balance to the match quality of the projection target.

A synthetic-data comparison documents the empirical consequence of this difference; the numerical results are reported in Section 4, with the qualitative finding that `gips` remains above the Ledoit-Wolf 2004 relative Frobenius error in every operating regime evaluated, and far above the Shah projected estimator at the matched group.

A separate modern shrinkage estimator that warrants explicit identification is the analytical nonlinear-shrinkage estimator of Ledoit and Wolf [2020], denoted LW-NL throughout this paper. LW-NL applies a nonlinear function to each sample eigenvalue, with the function derived from the Marchenko-Pastur kernel density estimate of the sample-eigenvalue distribution; it is the analytical-formula successor to the QuEST nonlinear shrinkage method of Ledoit and Wolf [2012] and represents the modern frequentist frontier in the eigenvalue-shrinkage family. LW 2004 is used as the principal continuity comparator throughout Section 4 for direct continuity with the existing covariance-shrinkage literature, and LW-NL is added as a fifth estimator alongside the sample covariance, LW 2004, Shah-BMG, and the AD estimator calibrated by held-out NLL with BMG group selection (denoted AD-NLL-BMG).

A natural question with LW-NL in place is whether the structural- prior mechanism of the AD framework composes usefully with LW-NL’s nonlinear eigenvalue shrinkage. We test this with the AD-LW-NL composition defined in Section 3.3, in which the sample-covariance term of the AD convex blend is replaced by its LW-NL nonlinear shrinkage while the structural prior is retained. The three-column protocol comparison (LW-NL alone, AD-NLL-BMG alone, AD-LW-NL-NLL-

BMG combining the two regularization mechanisms) decomposes any empirical advantage into two attributable components: the structural-prior contribution (visible in AD versus LW-NL) and the nonlinear-shrinkage contribution within the AD framework (visible in AD-LW-NL versus AD). The empirical evaluation reported in Section 4 finds mixed results from the AD-LW-NL composition: a narrow regime of small benefit in the moderate- c well-conditioned regime on financial-returns data, and a sharper regime of substantial harm in the few-shot image-patch regime. AD-LW-NL is reported here as a tested composition with mixed empirical results, not as a recommended default. The mechanism for the few-shot image-patch deficit is discussed in Section 4: when LW-NL applied to the rank-deficient sample is worse than the structural projection, the AD-LW-NL cross-validation pins $\alpha = 1$ (pure projection) and loses access to the raw-sample blend path that AD-NLL-BMG exploits. AD-NLL-BMG remains the recommended default; AD-LW-NL is a specialization for moderate- c well-conditioned settings on data where LW-NL is substantially better than LW 2004 and the structural projection does not fully capture the variance structure.

The convex shrinkage step is structural rather than ornamental. When the population covariance is approximately rather than exactly invariant under the candidate group, the projected target is a biased estimator of the population, with a perpendicular-bias term that does not vanish in N . The convex blend of the projection with the sample covariance reduces this bias by allocating mass to the sample covariance in proportion to the perpendicular-residual variance, recovering an estimator that improves on Ledoit-Wolf shrinkage in mean-squared error under a quantitative sufficient-match condition derived in Section 3. Outside this regime, Ledoit-Wolf shrinkage remains the appropriate baseline; this conservatism is intentional and is reflected in the dominance condition.

The remainder of the paper is organized as follows. Section 2 fixes notation, recalls the group-averaged sample covariance and the AD framework, and presents the candidate-library construction together with the BMG group-selection procedure. Section 3 develops the theoretical machinery: the construction of the estimator and its calibrations, the AD-LW-NL composition, the risk decomposition on the convex shrinkage family, the asymptotic crossover between the two natural calibrations, the finite-sample regret bound for the held-out calibration, the oracle inequality for the data-driven group selection, the sufficient-match condition for dominance over Ledoit-Wolf shrinkage, and the minimax rate results. Each theorem statement is followed immediately by its proof. Section 4 reports empirical results across six real-data settings selected to exercise different group families, with a distribution-shift companion on CIFAR-10.1 and a decoy stress test of the BMG procedure. Section 5 synthesizes the empirical and theoretical findings into a three-region phase diagram in $(N, M, |G|, \delta)$ coordinates that names the mechanism producing the boundary between adjacent regions and locates the empirical anchors from the real-data experiments within the predicted partition. Section 6 concludes, and Section 7 documents code and data availability.

2 Background

This section fixes the notation used throughout the paper, recalls the group-averaged sample covariance estimator from the AD framework, and describes the BMG selection procedure together with its algorithmic realization.

2.1 Notation and the group-averaged sample covariance

Let $\mathbf{x}_1, \dots, \mathbf{x}_N$ be independent and identically distributed observations of a random vector $\mathbf{x} \in \mathbb{R}^M$ with mean zero and population covariance Σ , and let $\hat{\mathbf{R}} = N^{-1} \sum_n \mathbf{x}_n \mathbf{x}_n^\top$ denote the sample

covariance. For a finite group G with unitary representation $\rho : G \rightarrow U(M)$, the *commutant algebra*

$$\mathcal{A}_G = \{\mathbf{A} \in \mathbb{R}^{M \times M} : \rho(g)\mathbf{A}\rho(g)^\top = \mathbf{A} \text{ for all } g \in G\}$$

collects the matrices that are invariant under conjugation by every element of G . The Frobenius-orthogonal projection onto \mathcal{A}_G is the *Reynolds projection* [see, e.g., [Fulton and Harris, 1991](#), Section 1.2]

$$\mathcal{P}_G(\mathbf{A}) = \frac{1}{|G|} \sum_{g \in G} \rho(g) \mathbf{A} \rho(g)^\top, \quad (2)$$

and the *group-averaged sample covariance* is

$$\hat{\mathbf{R}}_G := \mathcal{P}_G(\hat{\mathbf{R}}). \quad (3)$$

The matrix $\hat{\mathbf{R}}_G$ is symmetric positive semidefinite, lies on the same scale as $\hat{\mathbf{R}}$, and commutes with every $\rho(g)$. When $\Sigma \in \mathcal{A}_G$, the group-averaged sample covariance is an unbiased estimator of Σ with variance reduced relative to $\hat{\mathbf{R}}$ by a factor that scales with the symmetric-subspace commutant dimension d_G (see Section 3); when $\Sigma \notin \mathcal{A}_G$, $\hat{\mathbf{R}}_G$ is a biased estimator whose bias is the Frobenius distance from Σ to \mathcal{A}_G .

2.2 The candidate library

The candidate library \mathcal{G} is a finite collection of candidate groups assembled before any data is examined. Useful sources include domain knowledge about the data regime (spatial lattice, temporal shift, hierarchical compositional structure, combinatorial substructure) and small libraries of generic finite groups that exercise common symmetries. Two extrema should always appear in \mathcal{G} : the trivial group $\{e\}$, for which the projection returns the sample covariance unchanged, and the full symmetric group S_M , for which the projection returns a compound-symmetry matrix; the latter is admitted only when M is small enough that this extreme amount of averaging is plausibly informative. Library construction is permissive rather than prescriptive: the user is not required to specify the correct group a priori, and the library may include candidates that turn out to be poor matches. The procedure that follows is designed to be robust to such inclusion, and a decoy stress test of this robustness is reported in Section 4.10.

2.3 The Best-Matched-Group (BMG) selection procedure

Selection from \mathcal{G} uses a procedure referred to as the *Best-Matched Group* (BMG) selection, defined by three structural commitments. The first is a *held-out predictive criterion*: the matched group is selected by K_{cv} -fold cross-validated evaluation of the per-candidate AD-plugin estimator, with a per-candidate score computed on held-out folds (Gaussian NLL in this paper). The second is the *candidate-library architecture* described in Section 2.2: the library \mathcal{G} is constructed in advance from domain-specific structural conventions and defines the search space within which the held-out criterion operates. The third is a *structural-fit diagnostic*: at the selected group \hat{G} , the dimensionless commutativity residual

$$\delta(\hat{G}, \hat{\mathbf{R}}) := \frac{\|\hat{\mathbf{R}} - \hat{\mathbf{R}}_{\hat{G}}\|_F}{\|\hat{\mathbf{R}}\|_F} \quad (4)$$

is reported as a post-hoc check that supports or undermines the selection independently of the held-out score.

The realization used in this paper is two-tier.

Tier 1: effective-rank prefilter. For each candidate $G \in \mathcal{G}$, admit G to Tier 2 if and only if

$$N \cdot |G| \geq \kappa M, \tag{5}$$

at a conservatism constant $\kappa \geq 1$ (default $\kappa = 2$). The prefilter removes candidates for which the group-averaged sample covariance would be rank-deficient or ill-conditioned at the given N , before any cross-validation work begins. The constant $\kappa = 1$ is the strict rank-inequality boundary at which the group-averaged sample covariance is non-singular in expectation; $\kappa = 2$ provides a safety factor that ensures well-conditioning rather than near-singularity. When the entire library fails (5), the procedure falls back to the Ledoit-Wolf estimator on the unstructured sample covariance and returns it with a flag indicating that no structured candidate was admitted.

Tier 2: cross-validated held-out NLL. Partition the training rows of the data matrix into K_{cv} contiguous folds. For each candidate G surviving Tier 1 and each fold k , fit the training-fold sample covariance $\hat{\mathbf{R}}^{(-k)}$ on the remaining $K_{cv} - 1$ folds, calibrate the shrinkage intensity on the same training folds (using the held-out NLL minimizer $\hat{\alpha}_{NLL}^*(G)$ developed in Section 3 and evaluated on an α -grid $\mathcal{A} \subset [0, 1]$), and evaluate the held-out NLL of the resulting AD-shrinkage estimator on the k th fold. Average the held-out NLLs across folds to produce a per-candidate score $\bar{L}_{cv}(G)$. The selected group is

$$\hat{G} = \underset{G \in \mathcal{G}, \text{ Tier 1 admitted}}{\operatorname{arg\,min}} \bar{L}_{cv}(G). \tag{6}$$

Output. The procedure returns the selected group \hat{G} , the calibrated shrinkage intensity $\hat{\alpha}_{NLL}^*(\hat{G})$ refit on the full training data, the resulting AD shrinkage estimator, and the structural-fit diagnostic $\delta(\hat{G}, \hat{\mathbf{R}})$ at the selected group. The diagnostic is reported alongside the estimator as a check against the held-out selection; small δ corroborates the selection while large δ flags a result obtained by minimizing the cross-validated score over a library that does not contain a near-symmetry of $\mathbf{\Sigma}$.

Computational cost. The dominant cost is the per-fold, per-candidate evaluation of the AD-plugin estimator and held-out NLL, which is $O(M^3)$ per fold per candidate per α -grid point. The total cost is therefore $O(|\mathcal{G}_{T1}| \cdot K_{cv} \cdot |\mathcal{A}| \cdot M^3)$, where $|\mathcal{G}_{T1}|$ is the size of the Tier 1 shortlist. The Tier 1 prefilter is $O(1)$ per candidate so its cost is negligible. The candidate-library construction is performed once upstream of BMG and its cost is application-specific.

Per-trial selection-stability diagnostic. The cross-validation step in Tier 2 produces, for each Tier 1 admitted candidate G , a held-out score $\bar{L}_{cv}(G)$. An additional per-trial diagnostic is recorded,

$$m_{cv} := \min_{G \neq \hat{G}} \bar{L}_{cv}(G) - \bar{L}_{cv}(\hat{G}), \tag{7}$$

the gap between the second-best and best Tier 2 scores. A large m_{cv} (relative to the within-candidate K_{cv} -fold standard deviation) corresponds to a declarative selection of \hat{G} ; a small m_{cv} corresponds to a regime in which multiple candidates are statistically indistinguishable in their Tier 2 score. The diagnostic does not modify the selection rule (6); it is reported alongside the selection as a regime indicator. Two notes on its interpretation are warranted. First, in cells where the BMG selects the trivial group, m_{cv} is identically zero by construction: the AD estimator at $\alpha = 0$ collapses to the sample covariance regardless of the candidate group’s projection, so all candidates with optimal $\alpha = 0$ produce identical Tier 2 scores at their respective alpha-minima. The $m_{cv} = 0$ value in this case is a structural artifact, not a noise-driven selection. Second, when the per-trial m_{cv} is small

but the directional consistency of the BMG selection across multiple subsample-split trials is high, the collective evidence for the selection is strong even though each individual margin is on the scale of fold-noise.

Generalizations. The procedure admits various extensions. The held-out score may be replaced by any downstream-task-aligned criterion (for example, mean predictive error in regression-on-covariance applications, or detection-task NLL in signal classification), and additional prefilter steps may be inserted between the rank inequality and the cross-validation step to further reduce the shortlist when the candidate library is large. We do not pursue these extensions here; the experiments of Section 4 use only the effective-rank prefilter at Tier 1 and the held-out NLL criterion at Tier 2.

Distinction from prior approaches. The BMG procedure differs from Ledoit and Wolf [2004], which fixes the target as the scaled identity (corresponding to averaging over the full orthogonal group) and requires no group selection, and from Shah and Chandrasekaran [2012], which assumes the structural group is known a priori and performs no library search. The BMG group-selection therefore extends Shah and Chandrasekaran [2012] by replacing the prespecified-group assumption with a held-out predictive-criterion search over a curated library.

3 Theory

This section develops the formal machinery: notation, the convex shrinkage family and its two natural calibrations, the bias-variance risk decomposition, the asymptotic crossover between the two calibrations, the finite-sample regret bound and Ledoit-Wolf dominance condition, the oracle inequality for the data-driven group selection, and the rates and minimax results.

3.1 Setup and notation

Let $\mathbf{x}_1, \dots, \mathbf{x}_N$ be i.i.d. observations of a random vector $\mathbf{x} \in \mathbb{R}^M$ with mean zero and population covariance $\Sigma := \mathbb{E}[\mathbf{x}\mathbf{x}^\top] \in \mathbb{R}^{M \times M}$. The sample covariance is

$$\hat{\mathbf{R}} = \frac{1}{N} \sum_{n=1}^N \mathbf{x}_n \mathbf{x}_n^\top. \quad (8)$$

Let G be a finite group with a unitary representation $\rho : G \rightarrow U(M)$. The action of G on $M \times M$ matrices is by conjugation $\mathbf{A} \mapsto \rho(g)\mathbf{A}\rho(g)^\top$. The *commutant algebra* is

$$\mathcal{A}_G = \{\mathbf{A} \in \mathbb{R}^{M \times M} : \rho(g)\mathbf{A}\rho(g)^\top = \mathbf{A} \text{ for all } g \in G\}, \quad (9)$$

and $W_G := \mathcal{A}_G \cap \text{Sym}(M, \mathbb{R})$ denotes its symmetric-matrix part. The *Reynolds projection* onto \mathcal{A}_G , computed in the Frobenius inner product $\langle \mathbf{A}, \mathbf{B} \rangle_F = \text{tr}(\mathbf{A}^\top \mathbf{B})$ [Horn and Johnson, 2012, Chapter 5], is

$$\mathcal{P}_G(\mathbf{A}) = \frac{1}{|G|} \sum_{g \in G} \rho(g)\mathbf{A}\rho(g)^\top, \quad (10)$$

with orthogonal complement $\mathcal{P}_G^\perp := \mathbf{I} - \mathcal{P}_G$. The *group-averaged sample covariance* is $\hat{\mathbf{R}}_G := \mathcal{P}_G(\hat{\mathbf{R}})$.

The *convex shrinkage family* considered in this paper is

$$\hat{\mathbf{R}}_{\text{AD}}(\alpha) = (1 - \alpha)\hat{\mathbf{R}} + \alpha\hat{\mathbf{R}}_G, \quad \alpha \in [0, 1]. \quad (11)$$

The endpoints are the unstructured sample covariance ($\alpha = 0$) and the group-averaged covariance $\hat{\mathbf{R}}_G$ ($\alpha = 1$). We refer to α as the *shrinkage intensity*, following [Ledoit and Wolf \[2004\]](#). The bias of the projected target at the population is

$$\mathbf{B}_G := \boldsymbol{\Sigma} - \mathcal{P}_G(\boldsymbol{\Sigma}) = \mathcal{P}_G^\perp(\boldsymbol{\Sigma}), \quad (12)$$

and the dimensionless commutativity residual is

$$\delta(G, \boldsymbol{\Sigma}) := \|\mathbf{B}_G\|_F / \|\boldsymbol{\Sigma}\|_F. \quad (13)$$

3.2 The estimator and its calibrations

Two distinguished members of the family at the endpoints of the index set anchor the development. The first identifies the Reynolds projection at $G = O(M)$ with the Ledoit-Wolf identity-target estimator.

Proposition 3.1 (Ledoit-Wolf as the maximally symmetric endpoint). *Let $\hat{\mathbf{R}} \in \text{Sym}(M, \mathbb{R})$ be a real symmetric matrix, let $G = O(M)$ act on $\hat{\mathbf{R}}$ by conjugation $\rho(g) = g$, and let $\hat{\mathbf{R}}_{O(M)}$ denote the corresponding group-averaged covariance computed with respect to the Haar measure on $O(M)$. Then*

$$\hat{\mathbf{R}}_{O(M)} = \int_{O(M)} g \hat{\mathbf{R}} g^\top d\mu(g) = \frac{\text{tr} \hat{\mathbf{R}}}{M} \mathbf{I}, \quad (14)$$

which is the scaled-identity shrinkage target of [Ledoit and Wolf \[2004\]](#).

Proof. Define $A := \int_{O(M)} g \hat{\mathbf{R}} g^\top d\mu(g)$. For any $h \in O(M)$, the substitution $g' = hg$ together with left-invariance of the Haar measure μ gives

$$h A h^\top = \int_{O(M)} hg \hat{\mathbf{R}} g^\top h^\top d\mu(g) = \int_{O(M)} g' \hat{\mathbf{R}} (g')^\top d\mu(g') = A.$$

Since $h \in O(M)$ satisfies $h^\top = h^{-1}$, the identity $hAh^\top = A$ is equivalent to $Ah = hA$. Thus A commutes with every h in the standard representation of $O(M)$ on \mathbb{R}^M . The standard representation is irreducible over \mathbb{R} , so by Schur's lemma [[Serre, 1977](#), Proposition 4] $A = c\mathbf{I}$ for some $c \in \mathbb{R}$. Taking the trace of both sides of (14) and using the cyclic property $\text{tr}(g\hat{\mathbf{R}}g^\top) = \text{tr}(\hat{\mathbf{R}})$ identifies the scalar as $c = \text{tr} \hat{\mathbf{R}}/M$. \square

The second statement is the closed-form Frobenius-MSE optimum for the shrinkage intensity, the structural-target generalization of [Ledoit and Wolf \[2004, Theorem 2.1\]](#).

Proposition 3.2 (Optimal shrinkage intensity in Frobenius MSE). *Let $V_\perp := \mathbb{E}\|\mathcal{P}_G^\perp(\hat{\mathbf{R}} - \boldsymbol{\Sigma})\|_F^2$ and $D := \|\mathbf{B}_G\|_F^2$. The shrinkage intensity that minimizes the Frobenius mean-squared error of $\hat{\mathbf{R}}_{\text{AD}}(\alpha)$ is*

$$\alpha_{\text{MSE}}^* = \frac{V}{V + D}, \quad (15)$$

and the corresponding minimum MSE is

$$\mathbb{E}\|\hat{\mathbf{R}}_{\text{AD}}(\alpha_{\text{MSE}}^*) - \boldsymbol{\Sigma}\|_F^2 = \mathbb{E}\|\mathcal{P}_G(\hat{\mathbf{R}} - \boldsymbol{\Sigma})\|_F^2 + \frac{V \cdot D}{V + D}, \quad (16)$$

strictly smaller than the MSE at either endpoint $\alpha = 0$ or $\alpha = 1$ when $V_\perp > 0$ and $D > 0$.

Proof. Let $\boldsymbol{\eta} := \hat{\mathbf{R}} - \boldsymbol{\Sigma}$, so $\mathbb{E}[\boldsymbol{\eta}] = \mathbf{0}$. Direct computation gives

$$\hat{\mathbf{R}}_{\text{AD}}(\alpha) - \boldsymbol{\Sigma} = \mathcal{P}_G(\boldsymbol{\eta}) + (1 - \alpha)\mathcal{P}_G^\perp(\boldsymbol{\eta}) - \alpha \mathbf{B}_G,$$

where $\mathcal{P}_G(\boldsymbol{\eta}) \in \mathcal{A}_G$ and the remaining two summands lie in \mathcal{A}_G^\perp . Squared Frobenius norm splits orthogonally; the cross term between $\mathcal{P}_G^\perp(\boldsymbol{\eta})$ and \mathbf{B}_G vanishes in expectation because $\mathbb{E}[\boldsymbol{\eta}] = \mathbf{0}$. Hence

$$\mathbb{E}\|\hat{\mathbf{R}}_{\text{AD}}(\alpha) - \boldsymbol{\Sigma}\|_F^2 = \mathbb{E}\|\mathcal{P}_G(\boldsymbol{\eta})\|_F^2 + (1 - \alpha)^2 V_\perp + \alpha^2 D.$$

The first term is independent of α ; differentiating the rest in α and setting equal to zero gives $\alpha^*(V_\perp + D) = V_\perp$, which is (15). Substituting back gives (16); strict improvement over either endpoint follows from strict convexity of the parabola $(1 - \alpha)^2 V_\perp + \alpha^2 D$ when $V_\perp, D > 0$. \square

The denominator of (15) admits an observable representation

$$V_\perp + D = \mathbb{E}\|\hat{\mathbf{R}} - \hat{\mathbf{R}}_G\|_F^2, \quad (17)$$

and replacing V_\perp and $V_\perp + D$ by their sample analogs gives the *closed-form plug-in calibration*

$$\widehat{V}_\perp := \frac{1}{N^2} \sum_{k=1}^N \|\mathcal{P}_G^\perp(\mathbf{x}_k \mathbf{x}_k^\top) - \mathcal{P}_G^\perp(\hat{\mathbf{R}})\|_F^2, \quad (18)$$

$$\widehat{V}_\perp + D := \|\hat{\mathbf{R}} - \hat{\mathbf{R}}_G\|_F^2, \quad (19)$$

$$\hat{\alpha}_{\text{MSE}}^* = \min\left(1, \max(0, \widehat{V}_\perp / \widehat{V}_\perp + D)\right). \quad (20)$$

The MSE plug-in $\hat{\alpha}_{\text{MSE}}^*$ is the closed-form counterpart to the cross-validated calibration introduced below. Consistency of the plug-in for the population-optimal α^* is the LW2004 Theorem 3.3 analog for the structured-target setting; we record it next.

Proposition 3.3 (Consistency of the closed-form MSE plug-in). *Assume $\mathbf{x}_1, \dots, \mathbf{x}_N$ are i.i.d. with mean zero, population covariance $\boldsymbol{\Sigma}$, and bounded fourth moments. Then $\widehat{V}_\perp \rightarrow V_\perp$ and $\widehat{V}_\perp + D \rightarrow V_\perp + D$ in probability as $N \rightarrow \infty$, and consequently the closed-form plug-in $\hat{\alpha}_{\text{MSE}}^*$ defined by (18)–(20) satisfies*

$$\hat{\alpha}_{\text{MSE}}^* \rightarrow \alpha_{\text{MSE}}^* \quad \text{in probability as } N \rightarrow \infty. \quad (21)$$

Proof. We argue convergence in probability of \widehat{V}_\perp and $\widehat{V}_\perp + D$ separately, then combine via continuous mapping.

Convergence of $\widehat{V}_\perp + D$. By definition, $\widehat{V}_\perp + D = \|\hat{\mathbf{R}} - \hat{\mathbf{R}}_G\|_F^2 = \|\mathcal{P}_G^\perp(\hat{\mathbf{R}})\|_F^2$. Adding and subtracting $\boldsymbol{\Sigma}$ inside the projection,

$$\mathcal{P}_G^\perp(\hat{\mathbf{R}}) = \mathcal{P}_G^\perp(\hat{\mathbf{R}} - \boldsymbol{\Sigma}) + \mathcal{P}_G^\perp(\boldsymbol{\Sigma}) =: \mathbf{u}_\perp + \mathbf{B}_G,$$

where \mathbf{u}_\perp is mean-zero and \mathbf{B}_G is non-random. Squared Frobenius norm splits orthogonally in expectation (the cross term $\langle \mathbf{u}_\perp, \mathbf{B}_G \rangle_F$ has zero expectation), giving $\mathbb{E}\|\widehat{V}_\perp + D\| = \mathbb{E}\|\mathbf{u}_\perp\|_F^2 + \|\mathbf{B}_G\|_F^2 = V_\perp + D$. Under the bounded-fourth-moment assumption, the variance of the empirical squared-norm $\|\mathbf{u}_\perp\|_F^2$ is $O(1/N)$ by the sample-variance bound for Frobenius-norm functionals of independent sums, so $\widehat{V}_\perp + D \rightarrow V_\perp + D$ in probability by Markov.

Convergence of \widehat{V}_\perp . The sample analog (18) can be written

$$\widehat{V}_\perp = \frac{1}{N^2} \sum_{k=1}^N \|\mathcal{P}_G^\perp(\mathbf{x}_k \mathbf{x}_k^\top - \hat{\mathbf{R}})\|_F^2,$$

a degree-two U-statistic in the N independent observations. Under the fourth-moment assumption, $\mathbb{E}[\widehat{V}_\perp] = V_\perp + O(1/N)$ by the standard bias correction relating the sample-variance estimator to its population analog, and $\text{Var}(\widehat{V}_\perp) = O(1/N)$ by the Hoeffding decomposition for U-statistics. Markov's inequality gives $\widehat{V}_\perp \rightarrow V_\perp$ in probability.

Convergence of the ratio. The map $(a, b) \mapsto \min(1, \max(0, a/b))$ is continuous at $(V_\perp, V_\perp + D)$ whenever $V_\perp + D > 0$, which holds by the denominator-positivity assumption. The continuous mapping theorem then yields $\hat{\alpha}_{\text{MSE}}^* \rightarrow \alpha_{\text{MSE}}^*$ in probability, establishing (21). The quantitative oracle MSE-loss gap rate is given separately as Theorem 3.20 below. The argument parallels [Ledoit and Wolf \[2004, Theorems 3.3–3.4\]](#), which establishes the same parity for the identity-target shrinkage intensity. \square

The corresponding held-out calibration is the K -fold cross-validation minimizer of the Gaussian negative log-likelihood on validation folds. Define, for each fold k , the training estimator $\Sigma_\alpha^{(k)}(G) := (1 - \alpha)\hat{\mathbf{R}}_{\text{tr}}^{(k)} + \alpha \mathcal{P}_G(\hat{\mathbf{R}}_{\text{tr}}^{(k)})$ and the validation sample covariance $\hat{\mathbf{R}}_{\text{te}}^{(k)}$, and write

$$\widehat{L}_{\text{ho}}(\alpha; G) = \frac{1}{K} \sum_{k=1}^K \left[\frac{1}{2} \log \det \Sigma_\alpha^{(k)}(G) + \frac{1}{2} \text{tr}(\Sigma_\alpha^{(k)}(G)^{-1} \hat{\mathbf{R}}_{\text{te}}^{(k)}) \right]. \quad (22)$$

The behaviour of the population analog of (22) on the convex shrinkage family is the prerequisite for understanding the finite-sample held-out calibration; we record it next, before the finite-sample regime statement that depends on it.

Proposition 3.4 (Population NLL minimum). *For any population covariance Σ with $\mathbf{B}_G = \Sigma - \mathcal{P}_G(\Sigma) \neq 0$, the population NLL $L_{\text{pop}}(\alpha)$ is strictly increasing on $(0, 1]$, and*

$$\alpha_{\text{NLL, pop}}^* = \arg \min_{\alpha \in [0, 1]} L_{\text{pop}}(\alpha) = 0.$$

At the boundary $\mathbf{B}_G = 0$, the NLL is constant in α and any $\alpha \in [0, 1]$ is optimal; the unique-optimum $\alpha = 1$ identification used in Theorem 3.6 below arises only via the limit of finite-sample held-out NLL minimizers under $\delta \rightarrow 0$.

Proof. The population NLL is $L_{\text{pop}}(\alpha) = \frac{1}{2} (\log \det \Sigma_\alpha^{\text{pop}} + \text{tr}((\Sigma_\alpha^{\text{pop}})^{-1} \Sigma))$ with $\Sigma_\alpha^{\text{pop}} = \Sigma - \alpha \mathbf{B}_G$. Differentiating in α and using $\partial_\alpha \Sigma_\alpha^{\text{pop}} = -\mathbf{B}_G$ gives

$$\frac{dL_{\text{pop}}}{d\alpha} = \frac{\alpha}{2} \text{tr}((\Sigma_\alpha^{\text{pop}})^{-1} \mathbf{B}_G (\Sigma_\alpha^{\text{pop}})^{-1} \mathbf{B}_G),$$

where the substitution $\Sigma = \Sigma_\alpha^{\text{pop}} + \alpha \mathbf{B}_G$ collapses the leading-order trace term. The trace is the $(\Sigma_\alpha^{\text{pop}})^{-1}$ -weighted Frobenius squared norm of \mathbf{B}_G on the positive-definite Mahalanobis metric, hence strictly positive when $\mathbf{B}_G \neq 0$ and $\alpha > 0$. The unique zero on $[0, 1]$ is therefore $\alpha = 0$, and L_{pop} is strictly increasing on $(0, 1]$. At $\mathbf{B}_G = 0$, the derivative is identically zero; L_{pop} is constant on $[0, 1]$. \square

Lemma 3.5 (Stein-loss leading-order expansion). *Let Y be a Hermitian random matrix with $\mathbb{E}[Y] = \Sigma \succ 0$, let $Z := Y - \Sigma$ (mean-zero perturbation), and define the Stein loss $\mathcal{L}_S(Y; \Sigma) := \text{tr}(Y^{-1} \Sigma) - \log \det(Y^{-1} \Sigma) - M$. Then*

$$\mathbb{E}[\mathcal{L}_S(Y; \Sigma)] = \frac{1}{2} \mathbb{E} \left\| \Sigma^{-1/2} Z \Sigma^{-1/2} \right\|_F^2 + O(\mathbb{E} \|Z\|_F^3), \quad (23)$$

provided $\sigma_{\min}(\Sigma) \geq \lambda > 0$ and the higher moments are bounded.

Proof. Write $Y = \Sigma^{1/2}(I + W)\Sigma^{1/2}$ with $W := \Sigma^{-1/2}Z\Sigma^{-1/2}$ Hermitian and $\mathbb{E}[W] = 0$. Then $\text{tr}(Y^{-1}\Sigma) = \text{tr}((I + W)^{-1})$ and $\log \det(Y^{-1}\Sigma) = -\log \det(I + W)$. Expand both for $\|W\| < 1$ (which holds with high probability under the higher-moment bound combined with $\sigma_{\min}(\Sigma) \geq \lambda$):

$$\begin{aligned}\text{tr}((I + W)^{-1}) &= M - \text{tr}(W) + \text{tr}(W^2) - \text{tr}(W^3) + O(\|W\|^4), \\ \log \det(I + W) &= \text{tr}(W) - \frac{1}{2}\text{tr}(W^2) + \frac{1}{3}\text{tr}(W^3) - O(\|W\|^4).\end{aligned}$$

Adding and subtracting M , the linear terms in W cancel and the quadratic terms combine:

$$\mathcal{L}_S(Y; \Sigma) = \frac{1}{2}\text{tr}(W^2) - \frac{2}{3}\text{tr}(W^3) + O(\|W\|^4) = \frac{1}{2}\|W\|_F^2 + O(\|W\|^3),$$

using $\text{tr}(W^2) = \|W\|_F^2$ for W Hermitian. Taking expectation and substituting $W = \Sigma^{-1/2}Z\Sigma^{-1/2}$ gives (23). \square

Theorem 3.6 (NLL-optimal shrinkage intensity). *Let $\hat{\mathbf{R}}_{\text{tr}}^{(k)}$ and $\hat{\mathbf{R}}_{\text{te}}^{(k)}$ be the training and held-out sample covariances on disjoint folds of comparable sizes drawn i.i.d. from a sub-Gaussian distribution with population covariance Σ of bounded condition number. Let $\hat{\alpha}_{\text{NLL}}^*$ be the unique solution of the first-order condition for (22) on $[0, 1]$. Two regimes apply.*

Mismatched-population regime. When $\Sigma \notin \mathcal{A}_G$ (i.e., $\mathbf{B}_G := \Sigma - \mathcal{P}_G(\Sigma) \neq 0$), the population NLL is strictly increasing in α on $(0, 1]$ with minimum at $\alpha = 0$ (Proposition 3.4). The empirical minimizer satisfies $\hat{\alpha}_{\text{NLL}}^ \rightarrow 0$ in probability as $N \rightarrow \infty$, with regret $L_{\text{pop}}(\hat{\alpha}_{\text{NLL}}^*) - L_{\text{pop}}(0) = O_P(M^2/N)$.*

Matched-population regime. When $\Sigma \in \mathcal{A}_G$ exactly ($\mathbf{B}_G = 0$), the population NLL is constant in α on $[0, 1]$, but the expected held-out NLL is, to leading order in noise scale and provided $|G| > 1$ acts non-trivially, strictly decreasing in α on $[0, 1)$ with minimum at $\alpha = 1$. Consequently $\hat{\alpha}_{\text{NLL}}^ \rightarrow 1$ in probability as $N \rightarrow \infty$ at the matched limit.*

Crossover behaviour. For fixed $\mathbf{B}_G \neq 0$ but small, the finite-sample $\hat{\alpha}_{\text{NLL}}^$ migrates from values near 1 in the variance-dominated small- N regime to values near 0 in the bias-dominated large- N regime; the boundary is approximately $NV_{\perp} \sim \|\mathbf{B}_G\|_F^2$, where V_{\perp} is the perp-residual variance.*

Proof. The theorem is a delegation of three claims to results stated elsewhere.

Mismatched-population claim. When $\mathbf{B}_G \neq 0$, Proposition 3.4 gives the population NLL minimum at $\alpha = 0$ with strict positive curvature on $(0, 1]$, and Theorem 3.17 gives the finite-sample regret bound $L_{\text{pop}}(\hat{\alpha}_{\text{NLL}}^*) - L_{\text{pop}}(0) = O_P(M^2/N)$ at this boundary minimum via the derivative-process bound combined with one-sided curvature. The two together imply $\hat{\alpha}_{\text{NLL}}^* \rightarrow 0$ in probability and the stated regret rate.

Matched-population claim. At $\mathbf{B}_G = 0$ the population NLL is constant in α , so the population objective alone is uninformative. Theorem 3.7 establishes via Lemma 3.5 that the expected held-out NLL is, to leading order in noise scale and provided $|G| > 1$ acts non-trivially, strictly decreasing in α on $[0, 1)$ with minimum at $\alpha = 1$. Sub-Gaussian concentration gives empirical convergence $\hat{\alpha}_{\text{NLL}}^* \rightarrow 1$ in probability.

Crossover claim. For fixed $\mathbf{B}_G \neq 0$ and $N \rightarrow \infty$, Proposition 3.15 gives both α_{MSE}^* and $\bar{\alpha}_{\text{NLL}}^*$ approaching zero at rate $\Theta(1/N)$. The boundary scale $NV_{\perp} \asymp \|\mathbf{B}_G\|_F^2$ emerges from balancing the variance contribution $V_{\perp}(1 - \alpha)^2 \sim 1/N$ against the bias contribution $\alpha^2\|\mathbf{B}_G\|_F^2$ in the held-out NLL Taylor expansion. In the strong-match boundary $\mathbf{B}_G \rightarrow 0$, the matched-population claim takes over. \square

Theorem 3.7 (Matched-limit optimality of $\alpha = 1$). *Let G be a candidate group with $\mathbf{B}_G = 0$ (so $\Sigma \in \mathcal{A}_G$) and $|G| > 1$ acting non-trivially on \mathbb{C}^M . Suppose the cross-validation in (22) produces training and test folds of comparable sizes from a sub-Gaussian distribution with bounded condition*

number. In the small-noise regime $V_{\perp}(G) = o(\sigma_{\min}(\mathbf{\Sigma})^2)$ (equivalently $N \gg M^2/\lambda^2$ for spectral lower bound λ), the expected held-out negative log-likelihood is, to leading order in noise scale, strictly decreasing in α on $[0, 1)$ with minimum at $\alpha = 1$. Consequently $\hat{\alpha}_{\text{NLL}}^* \rightarrow 1$ in probability as $N \rightarrow \infty$.

Proof. At the matched limit $\mathbf{B}_G = 0$, the training-fold sample covariance noise decomposes as $\mathbf{u}^{\text{tr}} = \mathbf{u}_{\text{in}}^{\text{tr}} + \mathbf{u}_{\perp}^{\text{tr}}$ with $\mathbf{u}_{\text{in}}^{\text{tr}} \in \mathcal{A}_G$ and $\mathbf{u}_{\perp}^{\text{tr}} \in \mathcal{A}_G^{\perp}$. The convex-combination estimator is $\mathbf{\Sigma}_{\alpha}^{\text{tr}} = \mathbf{\Sigma} + \alpha \mathbf{u}_{\text{in}}^{\text{tr}} \mathbf{u}_{\text{in}}^{\text{tr}} + (1 - \alpha) \mathbf{u}_{\perp}^{\text{tr}} \mathbf{u}_{\perp}^{\text{tr}}$, with deviation $Z := \mathbf{\Sigma}_{\alpha}^{\text{tr}} - \mathbf{\Sigma} = \alpha \mathbf{u}_{\text{in}}^{\text{tr}} \mathbf{u}_{\text{in}}^{\text{tr}} + (1 - \alpha) \mathbf{u}_{\perp}^{\text{tr}} \mathbf{u}_{\perp}^{\text{tr}}$.

By the relation $\mathbb{E}[L_{\text{ho}}(\alpha)] = \frac{1}{2} \mathbb{E}[\mathcal{L}_S(\mathbf{\Sigma}_{\alpha}^{\text{tr}}; \mathbf{\Sigma})] + \frac{1}{2} \log \det \mathbf{\Sigma} + \frac{M}{2}$, minimizing the expected held-out NLL in α is equivalent to minimizing $\mathbb{E}[\mathcal{L}_S(\mathbf{\Sigma}_{\alpha}^{\text{tr}}; \mathbf{\Sigma})]$. Apply Lemma 3.5:

$$\mathbb{E}[\mathcal{L}_S(\mathbf{\Sigma}_{\alpha}^{\text{tr}}; \mathbf{\Sigma})] = \frac{1}{2} \mathbb{E} \left\| \mathbf{\Sigma}^{-1/2} (\mathbf{u}_{\text{in}}^{\text{tr}} + (1 - \alpha) \mathbf{u}_{\perp}^{\text{tr}}) \mathbf{\Sigma}^{-1/2} \right\|_F^2 + O(\mathbb{E} \|\mathbf{u}^{\text{tr}}\|_F^3).$$

Since $\mathbf{\Sigma} \in \mathcal{A}_G$ at the matched limit, the metric matrix $\mathbf{\Sigma}^{-1/2}$ is also in \mathcal{A}_G (by functional calculus on commuting operators). Conjugation by $\mathbf{\Sigma}^{-1/2}$ therefore preserves the \mathcal{A}_G -vs- \mathcal{A}_G^{\perp} orthogonal split: $\mathbf{\Sigma}^{-1/2} \mathbf{u}_{\text{in}}^{\text{tr}} \mathbf{\Sigma}^{-1/2} \in \mathcal{A}_G$ and $\mathbf{\Sigma}^{-1/2} \mathbf{u}_{\perp}^{\text{tr}} \mathbf{\Sigma}^{-1/2} \in \mathcal{A}_G^{\perp}$, with Frobenius inner product zero. Hence

$$\mathbb{E}[\mathcal{L}_S(\mathbf{\Sigma}_{\alpha}^{\text{tr}}; \mathbf{\Sigma})] = \frac{1}{2} T_{\text{in}} + \frac{(1-\alpha)^2}{2} T_{\perp} + O(\mathbb{E} \|\mathbf{u}^{\text{tr}}\|_F^3),$$

where $T_{\text{in}}, T_{\perp} \geq 0$ are independent of α and $T_{\perp} > 0$ when $|G| > 1$ acts non-trivially. The expression is strictly decreasing in α on $[0, 1)$ with minimum at $\alpha = 1$ to leading order. The remainder is $O(M^3/N^{3/2})$ by sub-Gaussian moment bounds, smaller than the $O(1/N)$ leading term in the small-noise regime. Consistency $\hat{\alpha}_{\text{NLL}}^* \rightarrow 1$ follows from uniform sub-Gaussian concentration on the compact interval $[0, 1]$. \square

Remark 3.8 (Bias characterization). The structural bias \mathbf{B}_G defined in (12) satisfies $\mathbf{B}_G = \mathbf{0}$ if and only if $\mathbf{\Sigma} \in \mathcal{A}_G$, equivalently $\delta(G, \mathbf{\Sigma}) = 0$. The matched/mismatched dichotomy used throughout this section identifies exactly these two cases: matched when $\delta = 0$, mismatched when $\delta > 0$.

Remark 3.9 (Well-conditioning). The convex blend (11) is positive semidefinite for every $\alpha \in [0, 1]$, since it is a non-negative combination of two positive-semidefinite matrices ($\hat{\mathbf{R}}$ and its Reynolds projection $\hat{\mathbf{R}}_G$, the latter PSD because Reynolds averaging preserves the cone). When the sample covariance is strictly positive definite, $\hat{\mathbf{R}}_{\text{AD}}(\alpha)$ is strictly positive definite for every $\alpha \in [0, 1]$. When the sample covariance is rank-deficient, $\hat{\mathbf{R}}_{\text{AD}}(\alpha)$ is positive definite for any $\alpha > 0$ such that $\hat{\mathbf{R}}_G$ is itself positive definite, which holds whenever the action of G on the sample provides at least one full orbit covering the spectrum (in particular, when $N \cdot |G| \geq M$). The estimator is therefore invertible across the few-shot regime, parallelling the well-conditioning property of Ledoit and Wolf [2004, Theorem 3.5].

3.3 Nonlinear shrinkage of the sample term: the AD-LW-NL composition

The AD estimator of (11) blends the raw sample covariance with a structured projection target. An immediate question is whether the AD framework's benefits compose with the nonlinear eigenvalue shrinkage of Ledoit and Wolf [2020] (LW-NL), the modern frequentist successor to LW 2004 in the eigenvalue-shrinkage family. This subsection defines the natural composition (AD-LW-NL), states its formal properties, and serves as the theoretical companion to the empirical evaluation reported in Section 4. The empirical evaluation finds that AD-LW-NL does not produce a sweet spot on any of the three datasets where the protocol has been run; the AD-LW-NL composition is tested rather than claimed.

The LW-NL estimator. For a sample covariance $\hat{\mathbf{R}}$ with spectral decomposition $\hat{\mathbf{R}} = \sum_{i=1}^M \lambda_i \mathbf{u}_i \mathbf{u}_i^\top$, Ledoit and Wolf [2020] replace each sample eigenvalue λ_i with a shrunken eigenvalue $\tilde{\lambda}_i$ while keeping the eigenvectors fixed. The shrinkage formula is

$$\tilde{\lambda}_i = \frac{\lambda_i}{[1 - c - c \lambda_i \mathcal{H}\tilde{f}(\lambda_i)]^2 + [\pi c \lambda_i \tilde{f}(\lambda_i)]^2}, \quad (24)$$

where $c = M/N$ is the concentration ratio, \tilde{f} is an Epanechnikov-kernel density estimate of the sample eigenvalue distribution with variable bandwidth $h_j = \lambda_j N^{-1/3}$, and $\mathcal{H}\tilde{f}$ is the Hilbert transform of \tilde{f} . The Hilbert transform admits a closed-form expression for the Epanechnikov kernel. The LW-NL estimator is

$$\hat{\mathbf{R}}_{\text{LW-NL}} = \sum_{i=1}^M \tilde{\lambda}_i \mathbf{u}_i \mathbf{u}_i^\top. \quad (25)$$

The estimator is positive semi-definite by construction (the $\tilde{\lambda}_i$ are nonnegative real numbers and the \mathbf{u}_i are orthonormal); it preserves the eigenvector basis of the sample covariance; and it preserves the trace approximately in the bulk regime, matching the Marchenko-Pastur asymptotic constraint that the average eigenvalue equals the population average.

The AD-LW-NL estimator. The AD-LW-NL estimator replaces the sample-covariance term in the AD convex blend (11) with its LW-NL shrinkage:

$$\hat{\mathbf{R}}_{\text{AD-LW-NL}}(\alpha; G) = (1 - \alpha) \hat{\mathbf{R}}_{\text{LW-NL}} + \alpha \hat{\mathbf{R}}_G. \quad (26)$$

The structured target $\hat{\mathbf{R}}_G = \mathcal{P}_G(\hat{\mathbf{R}})$ is the Reynolds projection of the *raw* sample covariance, not of its LW-NL shrinkage. This choice is deliberate: the projection target encodes the structural prior associated with the group G , and the projection \mathcal{P}_G is most naturally applied to the unmodified sample second-moment matrix that the population covariance is assumed to approximately equal under the symmetry hypothesis. Projecting LW-NL-shrunken eigenvalues onto the commutant of G would conflate the structural-prior averaging with the eigenvalue-shrinkage operation, with no clear principled benefit and with the cost of losing the convex-blend interpretation of α .

Boundary behavior and interpretation. At $\alpha = 0$ the AD-LW-NL estimator reduces to $\hat{\mathbf{R}}_{\text{LW-NL}}$, recovering LW-NL; at $\alpha = 1$ it reduces to the Reynolds projection $\hat{\mathbf{R}}_G$, identical to AD at the same operating point. The convex weight α continues to measure the contribution of the structural prior relative to the sample covariance; only the sample-covariance contribution has been upgraded from raw to nonlinearly-shrunken. In particular, the held-out NLL calibration (22) and the candidate-library Best-Matched-Group (BMG) selection procedure of Section 2.3 apply unchanged to the AD-LW-NL estimator, with the only modification being the swap of $\hat{\mathbf{R}}$ for $\hat{\mathbf{R}}_{\text{LW-NL}}$ inside the per-trial cross-validation loop.

Failure mode in the rank-deficient image-patch regime. The AD-LW-NL composition is upper-bounded in the favorable case by AD-NLL-BMG and lower-bounded in the unfavorable case by LW-NL, because at $\alpha = 1$ it reproduces AD’s Shah projection and at $\alpha = 0$ it reproduces LW-NL. Within those bounds, the held-out CV calibration of α is free to find any blend. An important asymmetry emerges in the rank-deficient regime ($c \geq 1$): the raw sample covariance $\hat{\mathbf{R}}$ is rank-deficient but may still carry residual information about pixel-level or feature-level correlation structure that an averaging projection \mathcal{P}_G collapses away. When this residual information is

exploitable, AD-NLL-BMG can find a blend (α, G) with α strictly less than 1 that outperforms the same group at $\alpha = 1$. In AD-LW-NL the raw sample is replaced by $\hat{\mathbf{R}}_{\text{LW-NL}}$, which on rank-deficient inputs may carry *less* of this residual information than the raw sample carries, because the LW-NL formula shrinks the zero-eigenvalue indices toward a single value (see the boundary-case discussion accompanying the LW-NL implementation note in Section 4). When LW-NL is worse than the structural projection at the same group, AD-LW-NL’s CV correctly pins $\alpha = 1$ to recover the Shah projection; but this then forecloses the raw-sample blend path that AD-NLL-BMG used to be preferred. In the empirical evaluation of Section 4, this failure mode is observed on Galaxy10 DECaLS image patches in the two smallest- N cells of the protocol sweep (AD-LW-NL performing worse than AD-NLL-BMG by 2 to 3 nats per sample, paired effect size 2 to 3 standard deviations), on the deepest CIFAR-10 cell at $c = 2.0$ (AD-LW-NL having higher NLL by 1.7 nats per sample, paired effect size 0.07), and at the largest magnitude on CIFAR-10.1 cells 0 through 2 at $c \in \{4, 5.33, 8\}$ (AD-LW-NL having higher NLL by 98 to 124 nats per sample, 0 of 49 to 50 paired trials favoring AD-LW-NL). The failure mode is not observed on TCGA-BRCA gene expression or on CRSP financial returns, where the AD framework’s structural projection captures essentially all the regularizable structure and the raw-sample residual is too noisy to be exploitable in the few-shot regime.

Family-conditional BMG and the choice-agreement statistic. Both AD-NLL-BMG and AD-LW-NL-NLL-BMG use the same Best Matched Group (BMG) selection procedure (CV-NLL-minimize over (G, α) in the candidate library), but the CV objective evaluates a different parametric family in each case. The two objectives are

$$J_G^{\text{AD}}(\alpha) = \text{CV-NLL}[\alpha T_G(\mathbf{S}) + (1 - \alpha) \mathbf{S}] \quad (27)$$

for AD-NLL-BMG, and

$$J_G^{\text{AD-LW}}(\alpha) = \text{CV-NLL}[\alpha T_G(\mathbf{S}) + (1 - \alpha) \hat{\mathbf{R}}_{\text{LW-NL}}] \quad (28)$$

for AD-LW-NL-NLL-BMG. Group selection is then $G^* = \arg \min_G \min_\alpha J_G(\alpha)$, which is composition-specific by construction. The procedure is identical; the objective being optimized is not. There is no a priori reason for the two optimizations to land at the same group.

The geometric picture: for each candidate group G , both compositions trace out a line segment in covariance-estimator space that *shares* the target endpoint $T_G(\mathbf{S})$ but has a different other endpoint (\mathbf{S} for AD, $\hat{\mathbf{R}}_{\text{LW-NL}}$ for AD-LW-NL). The CV finds the optimal point along that segment, and BMG picks the group whose segment’s optimum has the lowest CV-NLL. The bundle of segments through $\{T_G(\mathbf{S}) : G \in \text{library}\}$ goes in one direction (toward \mathbf{S}) for AD and a different direction (toward $\hat{\mathbf{R}}_{\text{LW-NL}}$) for AD-LW-NL. The closest-to-population-covariance segment in one bundle has no reason to be the same group as the closest-to-population segment in the other bundle.

The misconception worth being explicit about: there is no intrinsic “symmetry group of the dataset” that BMG is discovering. There is a candidate library, and within each family of compositions there is a *family-conditional best group*, the group whose Reynolds projection best complements that family’s other regularization tool. Different families pick different groups not because one is wrong but because they are solving different optimization problems. The choice-agreement statistic measures how strongly the data’s structure constrains the group selection across the family axis: high agreement (unanimous or near-unanimous across 50 trials per cell) means the data’s structure dominates the choice and the family-conditional groups coincide; low agreement (zero or near-zero across 50 trials per cell) means the family’s other regularization tool is a significant factor in the group selection.

Two practical consequences for interpreting the empirical results of Section 4. First, *choice agreement is information, not consistency*. A 0/50 agreement says the two parameterizations have found two different routes that the CV-NLL ranks differently within each family; it does not say one or both is confused. On RadioML cell 2 the AD-LW-NL composition has lower NLL at effect size 5.19; on OISST cells 0 through 5 the AD route has lower NLL by 2 to 19 nats per sample. Both produce 0/50 choice agreement, both reveal genuine "different optima found" behavior, but only the *direction* of which route has lower NLL is the substantive empirical content of the comparison. Second, the framework's diagnostic power scales with the number of distinct composition families: each new second hull endpoint (LW-NL, Stein-Haff [Stein, 1981, Haff, 1980] or Shah-Chandrasekaran, OAS, graphical lasso [Friedman et al., 2008], etc.) gives a new family-conditional BMG that probes the data through a different lens, and family-disagreement on the group choice maps regions of estimator space where multiple symmetry-like structures compete for "best target." The current paper has two compositions; future extensions with three or more would let the choice-disagreement statistics map the data's regularization geometry more finely.

the protocol: a three-column comparison. In the experimental work of Section 4, the AD, AD-LW-NL, and LW-NL estimators are reported in a three-column "the protocol" comparison alongside the LW 2004 baseline retained from earlier versions. The columns serve distinct purposes:

- AD-NLL-BMG vs LW-NL isolates the *structural-prior* contribution: the gap represents the advantage of the Reynolds-projected target over isotropic eigenvalue shrinkage, with neither method having access to the other's regularization mechanism.
- AD-LW-NL-NLL-BMG vs LW-NL isolates the structural-prior contribution *conditional on* nonlinear sample shrinkage: both methods enjoy the LW-NL nonlinear shrinkage, so the gap measures only the additional regularization provided by the structural prior.
- AD-LW-NL-NLL-BMG vs AD-NLL-BMG isolates the *nonlinear-shrinkage* contribution within the AD framework: the gap measures whether the nonlinear eigenvalue shrinkage of LW-NL adds value beyond the convex-blend shrinkage of the AD framework alone.

The three-column comparison decomposes the AD framework's empirical advantage into two attributable components (structural prior and nonlinear shrinkage) and exposes how they compose.

Computational cost. LW-NL adds an $O(M^3)$ per-cell cost for the spectral decomposition of $\hat{\mathbf{R}}$ [Golub and Van Loan, 2013, Chapter 8] plus an $O(M^2)$ cost for the kernel density and Hilbert transform evaluations, both of which are dominated by the existing cost of the cross-validated AD pipeline. The AD-LW-NL composition therefore adds approximately constant overhead per trial relative to AD-NLL-BMG. Caching the LW-NL estimator across the α -grid for a given training fold makes this overhead negligible compared to the BMG cross-validation loop.

3.4 Risk decomposition and structural results

The Reynolds projection's effect on the matched-Gaussian risk decomposes orthogonally into a structural-bias term and a variance-reduction term. The variance-reduction factor is governed by a single dimension parameter, the symmetric-subspace commutant dimension, which is recorded next.

Definition 3.10 (Symmetric-subspace commutant dimension). For a finite group G acting on \mathbb{R}^M via permutation representation ρ , the *commutant dimension* used throughout this paper is

$$d_G := \dim_{\mathbb{R}}(\mathcal{A}_G \cap \text{Sym}(M, \mathbb{R})), \quad (29)$$

the dimension of the commutant algebra restricted to real symmetric matrices.

Lemma 3.11 (Risk decomposition on the convex shrinkage family). *Let G be a finite group with unitary representation ρ on \mathbb{C}^M , let $\hat{\mathbf{R}}$ be the sample covariance of N independent observations of $\mathbf{x} \in \mathbb{C}^M$ with population covariance $\mathbf{\Sigma}$, and let $\mathbf{B}_G := \mathbf{\Sigma} - \mathcal{P}_G(\mathbf{\Sigma})$. Define*

$$V_{\text{in}}(G) := \mathbb{E} \left[\|\mathcal{P}_G(\hat{\mathbf{R}} - \mathbf{\Sigma})\|_F^2 \right], \quad V_{\perp}(G) := \mathbb{E} \left[\|(I - \mathcal{P}_G)(\hat{\mathbf{R}} - \mathbf{\Sigma})\|_F^2 \right]. \quad (30)$$

Then for any $\alpha \in [0, 1]$,

$$R_{\text{MSE}}(\alpha; G) := \mathbb{E} \left[\|\hat{\mathbf{R}}_{\text{AD}}(\alpha) - \mathbf{\Sigma}\|_F^2 \right] = V_{\text{in}}(G) + (1 - \alpha)^2 V_{\perp}(G) + \alpha^2 \|\mathbf{B}_G\|_F^2. \quad (31)$$

Proof. Write $\mathbf{u} := \hat{\mathbf{R}} - \mathbf{\Sigma}$ (mean-zero by unbiasedness of the sample covariance), and decompose $\mathbf{u} = \mathcal{P}_G(\mathbf{u}) + \mathbf{u}_{\perp}$ where $\mathbf{u}_{\perp} := (I - \mathcal{P}_G)(\mathbf{u})$. Then

$$\hat{\mathbf{R}}_{\text{AD}}(\alpha) - \mathbf{\Sigma} = \mathcal{P}_G(\mathbf{u}) + (1 - \alpha)\mathbf{u}_{\perp} - \alpha\mathbf{B}_G,$$

since $\mathcal{P}_G(\hat{\mathbf{R}}) - \mathcal{P}_G(\mathbf{\Sigma}) = \mathcal{P}_G(\mathbf{u})$ and the deterministic bias $\mathcal{P}_G(\mathbf{\Sigma}) - \mathbf{\Sigma} = -\mathbf{B}_G$. The three summands lie in \mathcal{A}_G , \mathcal{A}_G^{\perp} , \mathcal{A}_G^{\perp} respectively, so $\mathcal{P}_G(\mathbf{u})$ is Frobenius-orthogonal to the latter two deterministically. Compute the squared Frobenius norm: the $\langle \mathcal{P}_G(\mathbf{u}), v \rangle_F$ cross terms vanish identically; the cross term between \mathbf{u}_{\perp} and \mathbf{B}_G vanishes in expectation because \mathbf{u} is mean-zero and \mathbf{B}_G is non-random. Combining yields (31). \square

Theorem 3.12 (Bias-variance orthogonal parametrization). *Let $\hat{\mathbf{R}}_G = \mathcal{P}_G(\hat{\mathbf{R}})$ be the group-averaged sample covariance estimator with population covariance $\mathbf{\Sigma}$ and finite group G acting unitarily on \mathbb{C}^M . In the Gaussian regime with $\mathbf{x}_i \sim \mathcal{N}(0, \mathbf{\Sigma})$ i.i.d., the mean-squared error of $\hat{\mathbf{R}}_G$ admits the decomposition*

$$\text{MSE}(\hat{\mathbf{R}}_G) = \delta^2(G, \mathbf{\Sigma}) \|\mathbf{\Sigma}\|_F^2 + c_{\text{in}}(\mathbf{\Sigma}, G) \frac{d_G}{N} (1 + o(1)) \quad (32)$$

as $N \rightarrow \infty$, with d_G as in Definition 3.10 and $c_{\text{in}}(\mathbf{\Sigma}, G)$ a bounded constant satisfying $2\sigma_{\min}(\mathbf{\Sigma})^2 \leq c_{\text{in}}(\mathbf{\Sigma}, G) \leq 2\sigma_{\max}(\mathbf{\Sigma})^2$ that depends on the alignment of $\mathbf{\Sigma}$ with the isotypic decomposition of $\mathcal{A}_G \cap \text{Sym}(M, \mathbb{R})$ (Theorem 3.14). The bias term depends on G only through δ ; the variance term depends on G only through d_G , with the variance constant c_{in} depending on $\mathbf{\Sigma}$ but determined by the operator-trace formula given in Theorem 3.14.

Proof. The bias term is exactly $\|\mathcal{P}_G(\mathbf{\Sigma}) - \mathbf{\Sigma}\|_F^2 = \|\mathcal{P}_G^{\perp}(\mathbf{\Sigma})\|_F^2 = \delta^2(G, \mathbf{\Sigma}) \|\mathbf{\Sigma}\|_F^2$ by definition of δ in (13). For the variance, the projection \mathcal{P}_G acts as orthogonal projection on $\text{Sym}(M, \mathbb{R})$ onto $\mathcal{A}_G \cap \text{Sym}(M)$ of dimension d_G (by Schur's lemma applied to the conjugation action of ρ on $M \times M$ symmetric matrices). Under the Gaussian model $\mathbf{x}_i \sim \mathcal{N}(\mathbf{0}, \mathbf{\Sigma})$, Wick's theorem (the four-point Isserlis identity) gives the second-moment operator on $\text{Sym}(M, \mathbb{R})$ as $\mathbf{\Phi}_{\mathbf{\Sigma}}[\mathbf{A}] = 2\mathbf{\Sigma}\mathbf{A}\mathbf{\Sigma}$, with the N -sample variance scaled by $1/N$. The variance term $\mathbb{E} \|\mathcal{P}_G(\hat{\mathbf{R}} - \mathbf{\Sigma})\|_F^2$ is therefore $N^{-1} \text{tr}_{\mathcal{A}_G \cap \text{Sym}(M)}(\mathbf{\Phi}_{\mathbf{\Sigma}})$, which is $c_{\text{in}}(\mathbf{\Sigma}, G) d_G/N + o(1/N)$ where $c_{\text{in}}(\mathbf{\Sigma}, G)$ is the average eigenvalue of $\mathbf{\Phi}_{\mathbf{\Sigma}}$ restricted to the d_G -dimensional subspace $\mathcal{A}_G \cap \text{Sym}(M)$. The operator-norm bounds $2\sigma_{\min}(\mathbf{\Sigma})^2 \leq c_{\text{in}}(\mathbf{\Sigma}, G) \leq 2\sigma_{\max}(\mathbf{\Sigma})^2$ follow from the spectral bounds on $\mathbf{\Phi}_{\mathbf{\Sigma}}$. The variance therefore depends on G only through d_G (the dimension of the projected subspace), with the constant c_{in} depending on the alignment of $\mathbf{\Sigma}$'s spectrum with the isotypic decomposition of $\mathcal{A}_G \cap \text{Sym}(M)$ but not on G 's own structure beyond that subspace. \square

Remark 3.13 (On the variance constant at the LW corner). The dependence of c_{in} on Σ is essential, not cosmetic. Sanity check: at $G = O(M)$ acting by conjugation, $d_G = 1$ (only scalar matrices are commutant), and the in-algebra component is $\mathcal{P}_{O(M)}(\hat{\mathbf{R}}) = (\text{tr } \hat{\mathbf{R}}/M) \mathbf{I}$. Direct computation with $\Sigma = \mathbf{I}$ gives $\text{Var}(\text{tr } \hat{\mathbf{R}}) = 2M/N$ (sum of M independent χ^2 trace contributions), so $V_{\text{in}} = \text{Var}(\text{tr } \hat{\mathbf{R}}/M) \cdot M = 2/N$. This is consistent with $c_{\text{in}}(\mathbf{I}, O(M)) \cdot d_G/N = 2/N$ at $c_{\text{in}} = 2$, the value forced by both bounds $2\sigma_{\text{min}}^2 = 2\sigma_{\text{max}}^2 = 2$ for the isotropic spectrum. A formulation with the variance constant proportional to $\|\Sigma\|_F^2 = M$ rather than to σ^2 would over-predict the variance by a factor M at this corner.

Theorem 3.14 (Variance reduction on the in-algebra component). *Let G be a finite group with unitary representation ρ on \mathbb{C}^M , and let d_G be the symmetric-subspace commutant dimension of Definition 3.10. Under the matched-limit assumption $\Sigma \in \mathcal{A}_G$ and sub-Gaussian observations,*

$$V_{\text{in}}(G) := \mathbb{E} \|\mathcal{P}_G(\hat{\mathbf{R}} - \Sigma)\|_F^2 = c_{\text{in}}(\Sigma, G) \cdot \frac{d_G}{N} + o(1/N), \quad (33)$$

where $c_{\text{in}}(\Sigma, G)$ is the average eigenvalue of the Wishart second-moment operator $\Phi_{\Sigma}[\mathbf{A}] = 2\Sigma\mathbf{A}\Sigma$ restricted to $\mathcal{A}_G \cap \text{Sym}(M, \mathbb{R})$, satisfying $2\sigma_{\text{min}}(\Sigma)^2 \leq c_{\text{in}}(\Sigma, G) \leq 2\sigma_{\text{max}}(\Sigma)^2$. Equivalently, $\hat{\mathbf{R}}_G$ achieves the variance behaviour of a sample covariance with effective sample size $N \cdot M^2/d_G$ on its image \mathcal{A}_G , up to the spectral-alignment factor $c_{\text{in}}/(2\sigma_{\text{max}}^2)$.

Proof. The projection \mathcal{P}_G is orthogonal projection on $\text{Sym}(M, \mathbb{R})$ onto $\mathcal{A}_G \cap \text{Sym}(M)$ of dimension d_G (Definition 3.10), by Schur's lemma applied to the conjugation action. Under the matched-limit assumption $\Sigma \in \mathcal{A}_G$, the law of \mathbf{x} is invariant under $\rho(g)$ in the second-moment sense, so the covariance operator Φ_{Σ} of $\mathbf{u} := \hat{\mathbf{R}} - \Sigma$ on $\text{Sym}(M)$ commutes with \mathcal{P}_G . The in-algebra component is therefore

$$V_{\text{in}}(G) = \mathbb{E} \|\mathcal{P}_G(\mathbf{u})\|_F^2 = N^{-1} \text{tr}_{\mathcal{A}_G \cap \text{Sym}(M)}(\Phi_{\Sigma}),$$

where $\Phi_{\Sigma}[\mathbf{A}] = 2\Sigma\mathbf{A}\Sigma$ is the Wishart second-moment operator (the four-point Isserlis identity). The restricted trace is $c_{\text{in}}(\Sigma, G) \cdot d_G$ where $c_{\text{in}}(\Sigma, G)$ is the average eigenvalue of Φ_{Σ} on $\mathcal{A}_G \cap \text{Sym}(M)$, bounded above by $2\sigma_{\text{max}}(\Sigma)^2$ and below by $2\sigma_{\text{min}}(\Sigma)^2$ since the eigenvalues of Φ_{Σ} lie in the interval $[2\sigma_{\text{min}}(\Sigma)^2, 2\sigma_{\text{max}}(\Sigma)^2]$. Combining gives (33). The effective sample size $N \cdot M^2/d_G$ follows from comparing the rate d_G/N to the unstructured rate $M(M+1)/(2N) \asymp M^2/N$ on the full symmetric subspace, up to the spectral factor $c_{\text{in}}/(2\sigma_{\text{max}}^2) \in (\sigma_{\text{min}}^2/\sigma_{\text{max}}^2, 1]$. \square

3.5 Asymptotic crossover

The two calibrations of the shrinkage intensity introduced in Section 3.2 have closed-form leading-order optima as $N \rightarrow \infty$, and they generally differ. The next result locates the asymptotic optimum for each calibration to leading order.

Proposition 3.15 (Asymptotic crossover, Gaussian-Wishart). *Let $\mathbf{B}_G := \Sigma - \mathcal{P}_G(\Sigma) \neq 0$ and $D := \|\mathbf{B}_G\|_F^2$. Assume the observations $\mathbf{x}_1, \dots, \mathbf{x}_N$ are i.i.d. multivariate Gaussian with population covariance Σ (so the training-fold sample covariance error $\mathbf{E} := \hat{\mathbf{R}}^{\text{tr}} - \Sigma$ has the Wishart fourth-moment structure used below), and assume Σ has bounded condition number $0 < \lambda \leq \sigma_{\text{min}}(\Sigma) \leq \sigma_{\text{max}}(\Sigma) \leq \Lambda < \infty$. Define $Q_B := \text{tr}(\Sigma^{-1}\mathbf{B}_G\Sigma^{-1}\mathbf{B}_G)$ and let $c_{\perp} := \lim_{N \rightarrow \infty} N \mathbb{E} \|\mathbf{E}_{\perp}\|_F^2 \in (0, \infty)$.*

The MSE minimizer is

$$\alpha_{\text{MSE}}^* = \frac{c_{\perp}}{ND + c_{\perp}} (1 + o(1)). \quad (34)$$

The expected-NLL minimizer is

$$\bar{\alpha}_{\text{NLL}}^* = \frac{c(\Sigma, G)}{NQ_B} (1 + o(1)), \quad (35)$$

where the leading-order constant has the closed form

$$c(\boldsymbol{\Sigma}, G) = M(M+1) - 2d_G - 2(M+1)\text{tr}(\boldsymbol{\Sigma}^{-1}\mathbf{B}_G). \quad (36)$$

The constant $c(\boldsymbol{\Sigma}, G)$ is strictly positive whenever $|G| > 1$ acts non-trivially on \mathbb{C}^M .

Proof. MSE statement. The orthogonal risk decomposition of Lemma 3.11 gives $R_{\text{MSE}}(\alpha; G) = V_{\text{in}} + (1-\alpha)^2 V_{\perp} + \alpha^2 D$. Differentiating in α and setting equal to zero yields the population MSE optimum $\alpha_{\text{MSE}}^* = V_{\perp}/(V_{\perp} + D)$. Substituting $V_{\perp} = c_{\perp}/N + o(1/N)$ and multiplying numerator and denominator by N gives (34).

NLL statement. Write the training-fold estimator as $\boldsymbol{\Sigma}_{\alpha}^{\text{tr}} = \boldsymbol{\Sigma} + \boldsymbol{\delta}_{\alpha}$ with $\boldsymbol{\delta}_{\alpha} = -\alpha\mathbf{B}_G + \mathbf{E}_{\text{in}} + (1-\alpha)\mathbf{E}_{\perp}$, where $\mathbf{E}_{\text{in}} = \mathcal{P}_G(\mathbf{E})$ and $\mathbf{E}_{\perp} = (\mathbf{I} - \mathcal{P}_G)(\mathbf{E})$. Differentiating the expected held-out NLL in α yields the exact identity

$$\bar{L}'_{\text{ho}}(\alpha) = -\frac{1}{2} \mathbb{E}[\text{tr}((\boldsymbol{\Sigma}_{\alpha}^{\text{tr}})^{-1}(\mathbf{B}_G + \mathbf{E}_{\perp})(\boldsymbol{\Sigma}_{\alpha}^{\text{tr}})^{-1}(\boldsymbol{\Sigma}_{\alpha}^{\text{tr}} - \boldsymbol{\Sigma}))].$$

Expanding the resolvent at $\alpha = 0$ as $\hat{\mathbf{R}}^{-1} = \boldsymbol{\Sigma}^{-1} - \boldsymbol{\Sigma}^{-1}\mathbf{E}\boldsymbol{\Sigma}^{-1} + O(\|\mathbf{E}\|^2)$ and tracking which combinations survive at leading order $1/N$ identifies three contributing terms:

$$T_2 = \mathbb{E}[\text{tr}(\boldsymbol{\Sigma}^{-1}\mathbf{E}_{\perp}\boldsymbol{\Sigma}^{-1}\mathbf{E})],$$

and T_3, T_5 each of the form $-\mathbb{E}[\text{tr}(\mathbf{A}\mathbf{E}\mathbf{B}\mathbf{E})]$ for symmetric \mathbf{A}, \mathbf{B} involving $\boldsymbol{\Sigma}^{-1}$ and $\boldsymbol{\Sigma}^{-1}\mathbf{B}_G\boldsymbol{\Sigma}^{-1}$. The Wishart fourth-moment Isserlis identity $N\mathbb{E}[\text{tr}(\mathbf{A}\mathbf{E}\mathbf{B}\mathbf{E})] = \text{tr}(\boldsymbol{\Sigma}\mathbf{A}\boldsymbol{\Sigma}\mathbf{B}) + \text{tr}(\mathbf{A}\boldsymbol{\Sigma})\text{tr}(\mathbf{B}\boldsymbol{\Sigma})$ together with the operator identity $\mathcal{L}^2 \circ \Phi_{\boldsymbol{\Sigma}} = 2\text{Id}$ on $\text{Sym}(M, \mathbb{R})$, where

$$\Phi_{\boldsymbol{\Sigma}}[\mathbf{B}] := 2\boldsymbol{\Sigma}\mathbf{B}\boldsymbol{\Sigma}, \quad \mathcal{L}[\mathbf{B}] := \boldsymbol{\Sigma}^{-1/2}\mathbf{B}\boldsymbol{\Sigma}^{-1/2},$$

denote respectively the Wishart second-moment operator and the $\boldsymbol{\Sigma}^{-1/2}$ -conjugation map (so $\mathcal{L} \circ \Phi_{\boldsymbol{\Sigma}}[\mathbf{B}] = 2\boldsymbol{\Sigma}^{1/2}\mathbf{B}\boldsymbol{\Sigma}^{1/2}$ and a second application of \mathcal{L} recovers $2\mathbf{B}$, hence the identity), gives

$$N T_2 = 2\text{Tr}_{\text{Sym}}(\mathcal{P}_G^{\perp}) = M(M+1) - 2d_G,$$

and a parallel calculation gives $N(T_3 + T_5) = -2(M+1)\text{tr}(\boldsymbol{\Sigma}^{-1}\mathbf{B}_G)$. Combining,

$$N \bar{L}'_{\text{ho}}(0) = -\frac{1}{2}[(M(M+1) - 2d_G) - 2(M+1)\text{tr}(\boldsymbol{\Sigma}^{-1}\mathbf{B}_G)] + o(1).$$

For nonzero $\alpha = O(1/N)$, the deterministic bias contribution $-\alpha\mathbf{B}_G$ in $\boldsymbol{\delta}_{\alpha}$ adds a term $\frac{1}{2}\alpha Q_B$ to $\bar{L}'_{\text{ho}}(\alpha)$. Setting $\bar{L}'_{\text{ho}}(\alpha) = 0$ to leading order yields (35) with $c(\boldsymbol{\Sigma}, G)$ as in (36). Strict positivity of $c(\boldsymbol{\Sigma}, G)$ when $|G| > 1$ acts non-trivially is Lemma 3.18. \square

Remark 3.16 (Plug-in bias at finite N). The prediction (35)–(36) is stated in terms of the population $\boldsymbol{\Sigma}$. Evaluating it on data substitutes $\hat{\mathbf{R}}^{-1}$ for $\boldsymbol{\Sigma}^{-1}$ and $\hat{\mathbf{R}} - \mathcal{P}_G(\hat{\mathbf{R}})$ for \mathbf{B}_G . Two distinct sources of error result. The first is the higher-order term in $\|\mathbf{B}_G\|$ omitted by the leading-order expansion; it is controlled by the empirical residual $\delta(G, \hat{\mathbf{R}})$ and vanishes in the matched limit. The second is the finite-sample bias of $\hat{\mathbf{R}}^{-1}$ as an estimator of $\boldsymbol{\Sigma}^{-1}$, which scales with the conditioning of $\hat{\mathbf{R}}$ and is largest at M/N near unity or when the population eigenvalue spectrum is highly non-uniform. The two sources are independent. The held-out calibration $\hat{\alpha}_{\text{NLL}}^*$ avoids the second source entirely because it does not invert any sample covariance during calibration; the empirical sections accordingly find it more reliable than the closed-form prediction on ill-conditioned data.

3.6 Performance guarantees

We now give the finite-sample guarantees for the two calibrations: a regret bound for the held-out NLL minimizer, a sufficient-match condition under which the proposed estimator dominates Ledoit-Wolf shrinkage in Frobenius MSE, and an oracle inequality for the closed-form MSE plug-in.

Theorem 3.17 (Regret bound for the held-out calibration). *Let G be fixed and suppose $\mathbf{B}_G := \boldsymbol{\Sigma} - \mathcal{P}_G(\boldsymbol{\Sigma}) \neq \mathbf{0}$. Assume that $\boldsymbol{\Sigma}$ has bounded condition number $\lambda \leq \sigma_{\min}(\boldsymbol{\Sigma}) \leq \sigma_{\max}(\boldsymbol{\Sigma}) \leq \Lambda$, that the observations are sub-Gaussian [see, e.g., Vershynin, 2018, Section 2.5] with constants independent of M and N , and that the population loss has one-sided quadratic curvature at the boundary minimizer $\alpha = 0$: there exists $c_B > 0$ such that $L'_{\text{pop}}(\alpha; G) \geq c_B \alpha$ for all $\alpha \in [0, 1]$. Let $\hat{\alpha}_{\text{NLL}}^*$ be the held-out NLL minimizer computed from $K \leq N/2$ comparable folds. Then there exists $C > 0$, depending on K, λ, Λ , the sub-Gaussian constant, and c_B , such that for all sufficiently large N ,*

$$\mathbb{E}[L_{\text{pop}}(\hat{\alpha}_{\text{NLL}}^*; G)] - \min_{\alpha \in [0, 1]} L_{\text{pop}}(\alpha; G) \leq C \cdot \frac{M^2}{N}. \quad (37)$$

Proof. By Proposition 3.4, when $\mathbf{B}_G \neq \mathbf{0}$ the population NLL minimum on $[0, 1]$ is $L_{\text{pop}}(0; G)$, attained at the boundary $\alpha = 0$. Define the derivative fluctuation process $Z_N(\alpha) := \widehat{L}'_{\text{ho}}(\alpha; G) - L'_{\text{pop}}(\alpha; G)$. Under the sub-Gaussian assumption, bounded condition number, and comparable fold sizes, the held-out NLL derivative is a smooth trace functional of the training and test sample covariances. Sub-Gaussian sample covariance concentration [Wainwright, 2019, Theorem 4.7.1] applied to $\widehat{\mathbf{R}}^{\text{tr}} - \boldsymbol{\Sigma}$ and $\widehat{\mathbf{R}}^{\text{te}} - \boldsymbol{\Sigma}$, combined with Lipschitz bounds for the inverse and log-determinant on the spectral interval $[\lambda/2, 2\Lambda]$ where the perturbed training covariance lies with high probability, gives

$$\mathbb{E} \left[\sup_{\alpha \in [0, 1]} |Z_N(\alpha)|^2 \right] \leq C_1 \frac{M^2}{N},$$

for C_1 depending on K, λ, Λ and the sub-Gaussian constant. If $\hat{\alpha}_{\text{NLL}}^* = 0$ the regret is exactly zero. Otherwise, first-order optimality at an interior minimizer (or, at $\hat{\alpha}_{\text{NLL}}^* = 1$, $\widehat{L}'_{\text{ho}}(1) \leq 0$) gives $\widehat{L}'_{\text{ho}}(\hat{\alpha}_{\text{NLL}}^*; G) \leq 0$, hence $L'_{\text{pop}}(\hat{\alpha}_{\text{NLL}}^*; G) \leq -Z_N(\hat{\alpha}_{\text{NLL}}^*) \leq \sup_{\alpha} |Z_N(\alpha)|$. The one-sided curvature condition gives

$$\hat{\alpha}_{\text{NLL}}^* \leq \frac{1}{c_B} \sup_{\alpha \in [0, 1]} |Z_N(\alpha)|.$$

Taylor expansion of L_{pop} around $\alpha = 0$ with quadratic upper bound $L_{\text{pop}}(\alpha) - L_{\text{pop}}(0) \leq C_2 \alpha^2$ on $[0, 1]$ at $\alpha = \hat{\alpha}_{\text{NLL}}^*$ gives

$$L_{\text{pop}}(\hat{\alpha}_{\text{NLL}}^*; G) - L_{\text{pop}}(0; G) \leq \frac{C_2}{c_B^2} \left(\sup_{\alpha} |Z_N(\alpha)| \right)^2.$$

Taking expectations and combining with the derivative-process bound yields (37) with $C = C_1 C_2 / c_B^2$. \square

Lemma 3.18 (Positivity of $c(\boldsymbol{\Sigma}, G)$). *For any SPD $\boldsymbol{\Sigma}$ and any finite group G acting unitarily on \mathbb{C}^M with $|G| > 1$ and non-trivial action,*

$$\text{tr}(\boldsymbol{\Sigma}^{-1} \mathbf{B}_G) \leq 0,$$

with equality if and only if $\boldsymbol{\Sigma} \in \mathcal{A}_G$. Consequently

$$c(\boldsymbol{\Sigma}, G) = M(M+1) - 2d_G - 2(M+1) \text{tr}(\boldsymbol{\Sigma}^{-1} \mathbf{B}_G) \geq M(M+1) - 2d_G > 0,$$

where the strict inequality $M(M+1) - 2d_G > 0$ holds whenever G acts non-trivially.

Proof. Write $\Sigma = \mathcal{P}_G(\Sigma) + \mathbf{B}_G$, so $\mathbf{B}_G = \mathcal{P}_G^\perp(\Sigma)$. Apply the Frobenius inner product:

$$\text{tr}(\Sigma^{-1}\mathbf{B}_G) = \langle \Sigma^{-1}, \mathbf{B}_G \rangle_F = \langle \Sigma^{-1}, \mathcal{P}_G^\perp(\Sigma) \rangle_F = \langle \mathcal{P}_G^\perp(\Sigma^{-1}), \mathcal{P}_G^\perp(\Sigma) \rangle_F,$$

since \mathcal{P}_G^\perp is a Frobenius-orthogonal projection. For SPD Σ , the function $\mathbf{X} \mapsto \mathbf{X}^{-1}$ is operator-monotone, and the Schur convexity of the trace pairing under group averaging gives $\mathcal{P}_G^\perp(\Sigma) \cdot \mathcal{P}_G^\perp(\Sigma^{-1}) \preceq 0$ in the trace sense, with equality if and only if Σ commutes with the group action, i.e., $\Sigma \in \mathcal{A}_G$. Hence $\text{tr}(\Sigma^{-1}\mathbf{B}_G) \leq 0$ with the stated equality conditions.

For the dimension inequality: at least one isotypic component of ρ has multiplicity strictly less than $M(M+1)/2$ since the trivial-group commutant $\mathcal{A}_{\{e\}} = \mathbb{R}^{M \times M}$ has dimension M^2 and the symmetric-subspace commutant W_G is a proper subspace whenever G acts non-trivially. Therefore $d_G < M(M+1)/2$, equivalently $M(M+1) - 2d_G > 0$. Combining with the non-positivity of $\text{tr}(\Sigma^{-1}\mathbf{B}_G)$ gives the displayed bound on $c(\Sigma, G)$. \square

Theorem 3.19 (Sufficient-match condition for dominance over Ledoit-Wolf). *Let G be a finite group acting unitarily on \mathbb{C}^M with Σ not a scalar multiple of \mathbf{I} . Let $V_{\text{in}}^{\text{LW}}, V_{\perp}^{\text{LW}}$ denote the in-algebra and perp-residual variance components of $\hat{\mathbf{R}}$ under the $G = O(M)$ action (so $\mathcal{P}_{O(M)}(\hat{\mathbf{R}}) = (\text{tr } \hat{\mathbf{R}}/M)\mathbf{I}$ by Schur's lemma). If*

$$V_{\text{in}}(G) + \frac{V_{\perp}(G) \|\mathbf{B}_G\|_F^2}{V_{\perp}(G) + \|\mathbf{B}_G\|_F^2} < V_{\text{in}}^{\text{LW}} + \frac{V_{\perp}^{\text{LW}} \|\Sigma - \mu\mathbf{I}\|_F^2}{V_{\perp}^{\text{LW}} + \|\Sigma - \mu\mathbf{I}\|_F^2}, \quad (38)$$

where $\mu = \text{tr } \Sigma/M$, then the proposed estimator at the oracle weight (15) has strictly smaller Frobenius MSE than the Ledoit-Wolf estimator at its oracle weight.

Proof. Both quantities arise as instances of Lemma 3.11 applied to different group actions: the proposed estimator with finite group G , the Ledoit-Wolf estimator with $G = O(M)$ acting by orthogonal conjugation. The optimal-shrinkage Frobenius MSE on the convex family is $V_{\text{in}} + V_{\perp} \cdot D/(V_{\perp} + D)$ in each case, with $D = \|\mathbf{B}_G\|_F^2$ for finite G and $D = \|\Sigma - \mu\mathbf{I}\|_F^2$ for $G = O(M)$ (by Proposition 3.1). The sufficient-match condition (38) is the direct comparison of these two quantities, hence implies strict Frobenius-MSE dominance. \square

The corresponding finite-sample guarantee for the closed-form MSE plug-in is the LW2004 Theorem 3.4 analog: the data-driven plug-in $\hat{\alpha}^*$ achieves the oracle MSE-loss with rate $1/N^2$.

Theorem 3.20 (Oracle inequality for the AD-plugin). *Let $\mathbf{x}_1, \dots, \mathbf{x}_N$ be i.i.d. samples from a distribution with mean zero, covariance Σ (not necessarily G -invariant), and bounded fourth moments. Let $\alpha^* = V_{\perp}/(V_{\perp} + D)$ be the population-optimal shrinkage from Proposition 3.2, and let $\hat{\alpha}^*$ be the data-driven plug-in defined by (18)–(20). Assume $V_{\perp} + D \geq c_0 > 0$ uniformly in the regime under consideration. Then*

$$\mathbb{E} \|\hat{\mathbf{R}}_{\text{AD}}(\hat{\alpha}^*) - \Sigma\|_F^2 = \mathbb{E} \|\hat{\mathbf{R}}_{\text{AD}}(\alpha^*) - \Sigma\|_F^2 + O\left(\frac{M^2 s^2}{N^2}\right) \quad (39)$$

as $N \rightarrow \infty$ with $M, |G|, \Sigma$ fixed (or jointly in a regime where $M^2/N \rightarrow 0$).

Proof. The MSE risk on the convex shrinkage family $R_{\text{MSE}}(\alpha; G) = V_{\text{in}} + (1 - \alpha)^2 V_{\perp} + \alpha^2 D$ from Lemma 3.11 is a smooth quadratic in α with minimizer $\alpha^* = V_{\perp}/(V_{\perp} + D)$ and second derivative $2(V_{\perp} + D)$. Taylor expansion of R_{MSE} around α^* gives

$$R_{\text{MSE}}(\hat{\alpha}^*; G) - R_{\text{MSE}}(\alpha^*; G) = (V_{\perp} + D) (\hat{\alpha}^* - \alpha^*)^2.$$

The plug-in estimator $\hat{\alpha}^*$ is a smooth function of the sample analogs $\widehat{V}_\perp, \widehat{V}_\perp + D$ defined in (18)–(19), both of which converge to their population counterparts at standard $1/\sqrt{N}$ rate under fourth-moment conditions; the bracketing argument of [Ledoit and Wolf \[2004, Theorem 3.4\]](#) then gives $\hat{\alpha}^* - \alpha^* = O_P(1/\sqrt{N})$. Squaring and applying the curvature factor $(V_\perp + D) \leq c_1 s^2$ (where c_1 depends on the operator-norm bound on Σ and the moment bound) gives the dimension-tracked $O(M^2 s^2/N^2)$ rate of (39). \square

3.7 Group selection

When the symmetry group is selected from data through the matching procedure of Section 2, the calibration regret incurs an additional model-selection penalty that scales with the log of the candidate-library size. The next result quantifies this penalty.

Theorem 3.21 (Oracle inequality for the BMG selection). *Let $\mathcal{G} = \{G_1, \dots, G_K\}$ be a finite candidate library, and let \hat{G} be the BMG selection minimizing the held-out negative log-likelihood across \mathcal{G} at the candidate-specific calibrated weights $\hat{\alpha}_{\text{NLL}}^*(G_k)$. Under the assumptions of Theorem 3.17 applied uniformly across the library, with cross-validation using K_{cv} folds, there exists $C' > 0$ such that for all sufficiently large N ,*

$$\mathbb{E}[L_{\text{pop}}(\hat{\alpha}^*(\hat{G}); \hat{G})] - \min_{G \in \mathcal{G}} \min_{\alpha \in [0,1]} L_{\text{pop}}(\alpha; G) \leq C' \sqrt{\frac{\log |\mathcal{G}|}{N}} + C \cdot \frac{M^2}{N}, \quad (40)$$

where C is the calibration regret constant from Theorem 3.17.

Proof. Let $G^* \in \arg \min_{G \in \mathcal{G}} \min_{\alpha} L_{\text{pop}}(\alpha; G)$ denote the oracle. Decompose the regret of \hat{G} as

$$\begin{aligned} & \mathbb{E}[L_{\text{pop}}(\hat{\alpha}^*(\hat{G}); \hat{G})] - L_{\text{pop}}(\alpha^*(G^*); G^*) \\ &= \underbrace{\mathbb{E}[L_{\text{pop}}(\hat{\alpha}^*(\hat{G}); \hat{G}) - \widehat{L}_{\text{ho}}(\hat{\alpha}^*(\hat{G}); \hat{G})]}_{\text{(A)}} \\ & \quad + \underbrace{\mathbb{E}[\widehat{L}_{\text{ho}}(\hat{\alpha}^*(\hat{G}); \hat{G}) - \widehat{L}_{\text{ho}}(\hat{\alpha}^*(G^*); G^*)]}_{\text{(B)} \leq 0} \\ & \quad + \underbrace{\mathbb{E}[\widehat{L}_{\text{ho}}(\hat{\alpha}^*(G^*); G^*) - L_{\text{pop}}(\hat{\alpha}^*(G^*); G^*)]}_{\text{(C)}} \\ & \quad + \underbrace{\mathbb{E}[L_{\text{pop}}(\hat{\alpha}^*(G^*); G^*) - L_{\text{pop}}(\alpha^*(G^*); G^*)]}_{\text{(D)}}. \end{aligned}$$

Term (B) is non-positive by the definition of \hat{G} . Terms (A) and (C) are bounded by the maximum over \mathcal{G} of the fluctuation $\widehat{L}_{\text{ho}}(\alpha; G) - L_{\text{pop}}(\alpha; G)$; sub-Gaussian concentration on each G together with a union bound over $|\mathcal{G}|$ candidates gives a $\sqrt{\log |\mathcal{G}|/N}$ rate. Term (D) is the calibration regret at the oracle group, bounded by Theorem 3.17 as CM^2/N . Combining gives (40). \square

Proposition 3.22 (Group recovery consistency). *Let \mathcal{G} be a finite candidate library and suppose there exists $G^* \in \mathcal{G}$ such that Σ is exactly G^* -invariant. Define*

$$\Theta(G^*, \Sigma) := \mathbb{E} \|\Sigma^{-1/2} (I - \mathcal{P}_{G^*}) (\hat{\mathbf{R}}^{\text{tr}}) \Sigma^{-1/2}\|_F^2.$$

Under the assumptions of Theorem 3.17 applied uniformly across \mathcal{G} , there exists $c > 0$ depending on $\lambda, \Lambda, K_{\text{cv}}$, the sub-Gaussian constant of \mathbf{x} , and the structure of \mathcal{G} , such that for sufficiently large N ,

$$\Pr(\hat{G} \neq G^*) \leq |\mathcal{G}| \cdot \exp(-c \cdot \Theta(G^*, \Sigma) \cdot N) + o(1). \quad (41)$$

Proof. At the matched group G^* , Theorem 3.7 gives $\hat{\alpha}^*(G^*) \rightarrow 1$ in probability with the resulting estimator $\mathcal{P}_{G^*}(\hat{\mathbf{R}}^{\text{tr}})$ having only the in-algebra component of noise. At any rival group $G \neq G^*$ with $\mathbf{B}_G \neq 0$, Proposition 3.15 gives $\hat{\alpha}^*(G) \rightarrow 0$ in probability with the resulting estimator $\hat{\mathbf{R}}^{\text{tr}}$ having both in-algebra and perp-residual components of noise.

By Lemma 3.5 applied to both estimators, the expected held-out NLL gap at the two operating points is, to leading order in noise scale,

$$\mathbb{E}[\widehat{L}_{\text{ho}}(\hat{\alpha}^*(G); G)] - \mathbb{E}[\widehat{L}_{\text{ho}}(\hat{\alpha}^*(G^*); G^*)] = \frac{1}{2} \Theta(G^*, \Sigma) + O(N^{-3/2}),$$

where the leading-order Θ term comes from the rival's perp-component variance contribution that does not appear at the matched group's $\alpha = 1$ operating point. Note that $\Sigma^{-1/2}$ commutes with \mathcal{P}_{G^*} at the matched limit, so the cross terms in the relevant Frobenius norms vanish identically. Sub-Gaussian concentration of the empirical NLL around its expectation, combined with a union bound over $|\mathcal{G}| - 1$ rivals, yields (41). \square

3.8 Rates and minimax

The rate analysis below uses two distinct dimension parameters from the isotypic decomposition of ρ : the symmetric-subspace commutant dimension d_G of Definition 3.10, used in the Frobenius rate; and the maximum multiplicity

$$d_{\max} := \max_{\lambda} m_{\lambda} \quad (42)$$

across irreducible components of ρ , used in the operator-norm rate. The structured-target rates below parallel the rate program for sparse covariance matrices [Bickel and Levina, 2008b,a, Cai and Liu, 2011, Cai and Zhou, 2012] and the symmetry-aware program of Shah and Chandrasekaran [2012], extending both with a minimax lower bound and a data-driven plug-in oracle inequality.

Theorem 3.23 (Frobenius-norm rate). *Let $\mathbf{x}_1, \dots, \mathbf{x}_N$ be i.i.d. samples from $\mathcal{N}(\mathbf{0}, \Sigma)$ with $\Sigma \in W_G$ and $\|\Sigma\|_{\text{op}} \leq s$. Then*

$$\mathbb{E} \|\hat{\mathbf{R}}_G - \Sigma\|_F^2 \leq \frac{2s^2 d_G}{N}. \quad (43)$$

Proof. Decompose into isotypic components in the symmetry-adapted basis: the projection \mathcal{P}_G acts as orthogonal projection on $\text{Sym}(M, \mathbb{R})$ onto a subspace of dimension d_G (Schur's lemma). Working in this basis, the centered error $\hat{\mathbf{R}}_G - \Sigma$ is supported on the d_G -dimensional symmetric subspace $\mathcal{A}_G \cap \text{Sym}(M)$. Under $\mathcal{N}(\mathbf{0}, \Sigma)$ observations with $\Sigma \in W_G$, the matched-Gaussian variance per free parameter is at most $2s^2/N$ at leading order in N , where $s^2 = \|\Sigma\|_{\text{op}}^2$ bounds the Wishart second-moment operator Φ_{Σ} on $\text{Sym}(M)$. Summing over the d_G free parameters yields (43). The full bound follows from the operator-trace identity $\text{tr}_{\mathcal{A}_G \cap \text{Sym}(M)}(\Phi_{\Sigma}) \leq 2\|\Sigma\|_{\text{op}}^2 d_G$ used in the proof of Theorem 3.14. \square

Theorem 3.24 (Operator-norm rate). *Let $\mathbf{x}_1, \dots, \mathbf{x}_N$ be i.i.d. sub-Gaussian samples with $\mathbf{x}_i = \Sigma^{1/2} \mathbf{z}_i$, where \mathbf{z}_i has independent sub-Gaussian entries with sub-Gaussian norm $\leq K$, and $\Sigma \in W_G$ with $\|\Sigma\|_{\text{op}} \leq s$. There exists an absolute constant $C > 0$ such that for any $t \geq 1$, with probability at least $1 - 2 \exp(-t^2 d_{\max})$,*

$$\|\hat{\mathbf{R}}_G - \Sigma\|_{\text{op}} \leq CK^2 s \left(t \sqrt{\frac{d_{\max}}{N}} + \frac{t^2 d_{\max}}{N} \right). \quad (44)$$

Proof. By Schur's lemma applied to the conjugation action of ρ on $\mathbb{C}^{M \times M}$, the symmetry-adapted unitary change of basis $T \in U(M)$ block-diagonalizes the commutant \mathcal{A}_G into isotypic blocks of size $m_\lambda \times m_\lambda$ each appearing with multiplicity d_λ (the irreducible representation dimension). Working in this basis, $T^*(\hat{\mathbf{R}}_G - \boldsymbol{\Sigma})T$ is block-diagonal with per-isotypic blocks $\hat{\boldsymbol{\Sigma}}_\lambda - \boldsymbol{\Sigma}_\lambda \in \text{Sym}_{m_\lambda}(\mathbb{R})$, and each block is a sample covariance with effective sample size $N \cdot d_\lambda$ (each observation \mathbf{x}_i provides d_λ independent replicates of an m_λ -dimensional vector through the irreducible carrier space). Apply [Wainwright \[2019, Theorem 4.7.1\]](#) to each block: with probability at least $1 - 2 \exp(-t^2 m_\lambda)$,

$$\|\hat{\boldsymbol{\Sigma}}_\lambda - \boldsymbol{\Sigma}_\lambda\|_{\text{op}} \leq CK^2 s (t \sqrt{m_\lambda / (Nd_\lambda)} + t^2 m_\lambda / (Nd_\lambda)).$$

Union-bound across isotypic components and observe $m_\lambda \leq d_{\max}$ together with $d_\lambda \geq 1$, giving (44). \square

Theorem 3.25 (Entrywise ℓ_∞ rate). *Let $\mathbf{x}_1, \dots, \mathbf{x}_N$ be i.i.d. sub-Gaussian samples as in Theorem 3.24. For each index pair (i, j) , let $\mathcal{O}(i, j) = \{(g(i), g(j)) : g \in G\}$ denote the orbit under the action of G , and let $d_{ij} = \max_k |\{\ell : (k, \ell) \in \mathcal{O}(i, j)\}|$ be the orbit degree. Set $\mathcal{O} = \min_{i,j} |\mathcal{O}(i, j)|$ and $\mathcal{O}_d = \min_{i,j} |\mathcal{O}(i, j)| / d_{ij}$. There exist absolute constants $c_1, c_2 > 0$ such that for any $t \geq 0$, the maximum-entry deviation satisfies*

$$\Pr(\|\hat{\mathbf{R}}_G - \boldsymbol{\Sigma}\|_\infty > t) \leq 2M^2 \max\left\{\exp\left(-\frac{c_1 N \mathcal{O} t^2}{K^4 s^2}\right), \exp\left(-\frac{c_2 N \mathcal{O}_d t}{K^2 s}\right)\right\}. \quad (45)$$

Proof. The result is [Shah and Chandrasekaran \[2012, Theorem 3.3\]](#) restated in our notation; the proof technique (per-orbit pre-Gaussian quadratic-form analysis followed by union bound) is identical to theirs and we refer the reader to their Appendix A for full detail. The key observation is that $(\hat{\mathbf{R}}_G - \boldsymbol{\Sigma})_{ij} = |\mathcal{O}(i, j)|^{-1} \sum_{(k, \ell) \in \mathcal{O}(i, j)} (\hat{\mathbf{R}} - \boldsymbol{\Sigma})_{k\ell}$ averages $|\mathcal{O}(i, j)|$ entries of the centered sample covariance, each of which is a sub-exponential pre-Gaussian quadratic form in the N independent observations under the sub-Gaussian assumption. Hanson-Wright concentration applied to each entry, combined with the orbit-averaging factor and union bound across the $\leq M^2$ distinct orbits, gives (45). An alternative proof via the isotypic decomposition is described in [Shah and Chandrasekaran \[2012, Section 3\]](#) and produces the same bound. \square

The minimax theorem below establishes the rate (43) is sharp up to constants. Define the parameter space

$$\Theta_G(s) = \{\boldsymbol{\Sigma} \in W_G \cap \text{Sym}_M^+(\mathbb{R}) : \|\boldsymbol{\Sigma}\|_{\text{op}} \leq s\}. \quad (46)$$

Theorem 3.26 (Minimax lower bound). *Let the data be N i.i.d. Gaussian samples in \mathbb{R}^M with covariance $\boldsymbol{\Sigma} \in \Theta_G(s)$. There exist absolute constants $c, c' > 0$ such that for all $d_G \geq 8$ and all $N \geq c' d_G$,*

$$\inf_{\hat{\boldsymbol{\Sigma}}} \sup_{\boldsymbol{\Sigma} \in \Theta_G(s)} \mathbb{E} \|\hat{\boldsymbol{\Sigma}} - \boldsymbol{\Sigma}\|_F^2 \geq c \cdot \frac{s^2 d_G}{N}, \quad (47)$$

where the infimum is over all measurable estimators based on the N samples.

Proof. Apply Fano's method on a packing of $\Theta_G(s)$. Let $\mathbf{B}_1, \dots, \mathbf{B}_{d_G}$ be an orthonormal basis of $W_G = \mathcal{A}_G \cap \text{Sym}(M, \mathbb{R})$ in the Frobenius inner product. For a separation parameter $\tau > 0$ to be chosen, consider the family of covariances

$$\boldsymbol{\Sigma}_\epsilon = \frac{s}{2} \mathbf{I} + \tau \sum_{j=1}^{d_G} \epsilon_j \mathbf{B}_j, \quad \epsilon \in \{-1, +1\}^{d_G},$$

with τ chosen small enough that $\Sigma_\epsilon \in \Theta_G(s)$. Two such covariances at Hamming distance h satisfy $\|\Sigma_\epsilon - \Sigma_{\epsilon'}\|_F^2 = 4\tau^2 h$. By the Gilbert-Varshamov bound, a packing of $2^{d_G/8}$ elements with pairwise Hamming distance at least $d_G/4$ exists. The Kullback-Leibler divergence between Gaussian distributions on this packing satisfies $\text{KL}(\mathcal{N}(0, \Sigma_\epsilon) \|\mathcal{N}(0, \Sigma_{\epsilon'})) \leq CN\tau^2 d_G/s^2$. Choose $\tau^2 = c_0 s^2/N$ for a small constant c_0 such that the KL divergence is at most $d_G/32$. Fano's inequality then gives that the minimax error exceeds $\tau^2 d_G/4 = c_0 s^2 d_G/(4N)$ on the constructed packing, proving (47). \square

Remark 3.27 (Rate-optimality). Combining Theorems 3.23 and 3.26, the group-averaged sample covariance $\hat{\mathbf{R}}_G$ is rate-optimal in Frobenius norm over $\Theta_G(s)$: its worst-case Frobenius MSE matches the minimax rate up to an absolute constant.

Corollary 3.28 (Sparse covariance rate under G -invariance). *For $\Sigma \in W_G \cap \mathcal{U}(q)$, where $\mathcal{U}(q) = \{\Sigma : \Sigma_{ii} \leq M, \sum_j |\Sigma_{ij}|^q \leq c_0(M)\}$ is the uniformity class of [Bickel and Levina \[2008a\]](#), with bounded $\|\Sigma\|_{\text{op}} \leq s$, choose the threshold*

$$t = M' \max \left\{ \sqrt{\frac{\log M}{N \mathcal{O}}}, \frac{\log M}{N \mathcal{O}_d} \right\} \quad (48)$$

for a sufficiently large constant M' . The thresholded projected estimator $\mathcal{T}_t(\hat{\mathbf{R}}_G)$ satisfies

$$\|\mathcal{T}_t(\hat{\mathbf{R}}_G) - \Sigma\|_{\text{op}} = \mathcal{O}_P \left(c_0(M) \left[\max \left\{ \sqrt{\frac{\log M}{N \mathcal{O}}}, \frac{\log M}{N \mathcal{O}_d} \right\} \right]^{1-q} \right). \quad (49)$$

Proof. The result is [Shah and Chandrasekaran \[2012, Theorem 4.1\]](#) restated in our notation. By Theorem 3.25, the projected estimator $\hat{\mathbf{R}}_G$ inherits the entrywise tail of an i.i.d. sample covariance with the orbit-parameter rate, replacing the standard rate $\sqrt{\log M/N}$ by $\sqrt{\log M/(N\mathcal{O})}$. The Bickel-Levina thresholding argument [[Bickel and Levina, 2008a](#)] then applies directly with $\hat{\mathbf{R}}_G$ in place of the unstructured sample covariance, giving the operator-norm rate (49) in which the orbit-parameter factor $\mathcal{O}^{(1-q)/2}$ replaces the sample-complexity term in the standard Bickel-Levina rate. \square

4 Experiments

In finite-sample settings, the sample covariance matrix is often poorly conditioned or severely biased, particularly in high-dimensional regimes. Our approach adopts a Ledoit-Wolf (LW) style regularization in which the convex combination of the empirical covariance and a data-driven structural target is formed by exploiting the symmetries present in the data. In particular, the few-shot setting is one in which a target consistent with the structure of the data is preferable to one in which the target is constrained to be a multiple of the identity matrix and therefore carries no structural information about the data, as in the case of LW. Our method reduces the eigenvalue distortion present in a limited number of samples by shrinking extreme eigenvalues toward a stable baseline while also enabling noise mitigation and numerical stability. To demonstrate the applicability of the technique, several data sets from different regimes are analyzed using both the MSE and NLL versions of the shrinkage intensity α and compared with the results from [Ledoit and Wolf \[2004\]](#) and [Shah and Chandrasekaran \[2012\]](#). These results also demonstrate the accuracy of the theoretically computed shrinkage intensity and crossover points where other forms of regularization are preferable. Estimators such as ours are most widely used in domains characterized by noisy,

high-dimensional covariance estimation, including quantitative finance, signal processing, machine learning, neuroscience, genomics, and wireless communications, where they are valued for robustness, improved conditioning, and strong finite-sample performance. The real-data experimental results follow.

4.1 Methodological note: the LW-NL comparison and the AD-LW-NL composition test

This paper extends the comparator set to include the analytical nonlinear shrinkage estimator of Ledoit and Wolf [2020] (LW-NL) alongside LW 2004, and empirically tests the AD-LW-NL composition defined in Section 3.3. Earlier versions cited LW-NL as the modern frequentist baseline against which any covariance shrinkage paper claiming improvement over Ledoit-Wolf shrinkage should be positioned, but did not include the empirical comparison. This subsection records the implementation conventions and the comparison protocol used; the per-experiment results follow in the appropriately-numbered subsections, and the LW-NL and AD-LW-NL findings are summarized in Section 4.11.

Estimators reported in each per-experiment subsection. Each per-experiment subsection in this paper reports six estimators on the same held-out NLL scale: the sample covariance, LW 2004 of Ledoit and Wolf [2004], LW-NL of Ledoit and Wolf [2020], AD-NLL-BMG as defined in earlier sections, the AD-LW-NL-NLL-BMG composition, and the Shah-BMG comparator retained from earlier versions. In plots where Shah-BMG coincides with the AD-NLL-BMG endpoint at $\alpha = 1$, the Shah-BMG line is omitted for visual clarity.

Implementation of LW-NL. The LW-NL estimator is implemented from the LW2020 paper directly in Python with NumPy only as a dependency. The shrinkage formula (24), the Epanechnikov kernel density estimate with variable bandwidth $h_j = \lambda_j N^{-1/3}$, and the closed-form Hilbert transform are computed in closed form for the Epanechnikov kernel. The implementation includes rank-aware handling of effective-rank deficiency, in which sample eigenvalues below $10^{-10} \lambda_{\max}$ are excluded from the variable-bandwidth KDE. Without this rank-aware handling, the LW-NL formula numerically saturates on real-data inputs where the sample covariance has machine-precision-zero eigenvalues from genuine linear dependencies among features (gene co-regulation in genomics; pixel-block dependencies in image patches; sector exposures in finance). The rank-aware version is what is used for all the results in this paper. The implementation has been verified against synthetic Marchenko-Pastur benchmarks at concentration ratios $c \in \{0.25, 0.5\}$ and several population eigenvalue structures (identity, geometric eigenvalue spread, two-block), with PRIAL values consistent with the regime reported in LW2020; implementation notes including the verification PRIAL table are in Appendix 4.

The AD-LW-NL pipeline. The AD-LW-NL pipeline integrates with the existing BMG cross-validation harness by swapping a single call: where the AD pipeline takes a training-fold sample covariance $\hat{\mathbf{R}}^{(-k)}$ as input to the α -grid evaluation, the AD-LW-NL pipeline pre-computes $\hat{\mathbf{R}}_{\text{LW-NL}}^{(-k)}$ once per fold and then uses it in place of $\hat{\mathbf{R}}^{(-k)}$ on the sample-covariance side of the convex blend (26). All other components of the BMG procedure (Tier 1 prefilter, K-fold partition, α -grid, held-out NLL evaluation, per-candidate ranking) are preserved verbatim. This makes the cost of the AD-LW-NL comparison incremental rather than a redesign of the experimental harness, and ensures that the AD-NLL-BMG vs AD-LW-NL-NLL-BMG comparison isolates exactly the effect of replacing the sample-covariance term with its LW-NL shrinkage.

the protocol: the three-column comparison. The AD-LW-NL audit in this paper is organized around the protocol three-column comparison introduced in Section 3.3. The three contrasts of interest are:

1. AD-NLL-BMG vs LW-NL: the structural-prior contribution unconditional on nonlinear shrinkage.
2. AD-LW-NL-NLL-BMG vs LW-NL: the structural-prior contribution conditional on nonlinear shrinkage of the sample term.
3. AD-LW-NL-NLL-BMG vs AD-NLL-BMG: the nonlinear-shrinkage contribution within the AD framework.

The three gaps decompose any AD-LW-NL versus AD-NLL-BMG difference into the two attributable mechanisms and expose how they compose on each real-data dataset. If a sweet spot for AD-LW-NL exists, the protocol contrast (3) will detect it; if AD-LW-NL is a strict loss in some regime, the same contrast will detect that.

the protocol sweep design. For each dataset where the protocol has been evaluated, the sweep varies the training-set size N_{train} across a fixed grid that spans the concentration ratio $c = M/N$ from the extreme few-shot regime ($c \approx 2$) through the deep bulk regime ($c \approx 0.1$). The hold-out evaluation size N_{test} is held fixed across the sweep so the per-window NLL values are directly comparable across cells. Each cell reports all six estimators on the same paired splits (or rolling windows for time-series data), permitting paired contrasts at the per-trial level. This design is heavier than the single-cell reporting of the experimental subsections, but is necessary to detect regime-dependent advantages or disadvantages that single-cell reporting at one operating point cannot resolve.

Reporting conventions. Per-experiment tables in this paper report mean held-out NLL across trials for each of the six estimators, with the three the protocol gaps computed at trial-level and reported as paired differences with their per-trial standard deviation. Effect sizes are reported as $|\Delta|/SD_{\text{trial}}$ in addition to paired t -statistics, because in many cells the paired t can be large due to highly correlated per-trial noise even when the practical effect size is tiny. Both quantities are reported so readers can distinguish statistically detectable shifts from practically meaningful ones. BMG selection counts are reported separately for AD-NLL-BMG and AD-LW-NL-NLL-BMG, since the two procedures may select different groups on a given trial even though they share the same candidate library and Tier 1 prefilter setting.

LW-NL verification status. As, the LW-NL implementation has been verified against synthetic Marchenko-Pastur benchmarks (Appendix 4) but not against the published numerical results of the LW2020 reference implementation on identical synthetic datasets. The verification is qualitative rather than exact: identity covariance at $c = 0.5$ gives PRIAL around 97%, consistent with the regime reported in LW2020; two-block eigenvalue distributions show $\text{PRIAL}(\text{LW-NL}) \lesssim \text{PRIAL}(\text{LW 2004})$ as expected since LW-NL adapts to bimodal eigenvalue distributions while LW 2004’s identity target does not; and geometric eigenvalue spread shows $\text{PRIAL}(\text{LW-NL})$ approximately equal to $\text{PRIAL}(\text{LW 2004})$, reflecting that the eigenvalue distribution’s mean coincides with the LW 2004 target. Exact agreement with the LW2020 reference numerics is left for a future revision.

4.2 S&P 500 daily returns, 2015–2019

We evaluate the four estimators on a rolling-window covariance estimation problem drawn from the CRSP daily stock file [Center for Research in Security Prices, 2024], with sectors linked through the CRSP-Compustat link table. A balanced panel of $M = 55$ S&P 500 constituents is formed by retaining the top five names by market capitalization within each of the 11 GICS sectors with complete return history over 2015-01-01 through 2019-12-31, giving $T = 1259$ trading days. A training window of $N_{\text{train}} = 252$ days slides forward in strides of 21 trading days; on each of the resulting 47 windows the shrinkage intensity is calibrated on the training panel and the held-out log-likelihood is evaluated on the next 21 days. The candidate library \mathcal{G} contains the two extrema $\{e\}$ and S_M together with six sector-aware candidates, of which three are tied within-sector cyclic shifts and two are high-order group structures introduced in the present paper. The tied candidates are the within-sector exchangeability product

$$G_{\text{GICS}} := \prod_{s=1}^{11} S_{|s|} = S_5^{11}, \quad (50)$$

which is the block-diagonal Young subgroup of S_M that permutes constituent indices within each GICS sector but does not mix indices across sectors. We refer to this group as GICS-BLOCK in figures and tables, and use the symbol G_{GICS} in mathematical expressions. Three within-sector cyclic-shift variants $\prod_s \mathbb{Z}_{|s|}$ are also included, ordered alphabetically by ticker, by market capitalization, and by within-sector hierarchical clustering on the training-window correlation matrix; in each of these the cyclic shift is tied across sectors so the group order is $|G| = K$ where K is the within-sector size (here $K = 5$). The two new high-order candidates are Z-K-MCAP-CARTESIAN, the Cartesian product $\prod_s \mathbb{Z}_K = \mathbb{Z}_5^{11}$ of independent within-sector cyclic shifts under the market-capitalization ordering ($|G| = K^B = 5^{11}$), and Z-K-MCAP-WREATH, the full wreath product $\mathbb{Z}_K \wr S_B = \mathbb{Z}_5 \wr S_{11}$ which lifts those independent cyclic shifts by free permutation of the eleven sectors as units ($|G| = K^B \cdot B! = 5^{11} \cdot 11! \approx 2 \times 10^{15}$). Both high-order candidates are constructed from a small set of generators (the eleven independent cyclic shifts plus the ten sector-adjacent transpositions for the wreath case) and the Reynolds projection is computed via the orbit-pair decomposition in $O(M^2)$ time, so neither requires direct enumeration of the group. This brings the CRSP library into structural parity with the RadioML and Galaxy10 libraries of Sections 4.6 and 4.7, both of which include high-order group candidates from a similar lattice structure of within-block cyclic and between-block permutation operations. The cross-validated NLL calibration uses $K = 5$ folds of the training window and a 13-point α -grid over $[0, 1]$. Figure 1 reports the per-window held-out NLL of every estimator and the per-window shrinkage intensity at the BMG-selected group.

Principal results. Both AD estimators outperform LW with strong significance. $\hat{\alpha}_{\text{MSE}}^*$ is preferred in 43 of 47 windows ($\bar{\Delta} = -0.92$ nats per day, paired $t = -6.18$, $p = 1.6 \times 10^{-7}$), and $\hat{\alpha}_{\text{NLL}}^*$ is preferred in 35 of 47 windows ($\bar{\Delta} = -1.34$ nats per day, paired $t = -4.82$, $p = 1.6 \times 10^{-5}$). The Shah estimator without shrinkage, fixing $\alpha = 1$ at the GICS-block group, trails LW by 1.48 nats per day on average ($t = +3.95$, $p = 3 \times 10^{-4}$); even when the candidate group for Shah is chosen by per-window oracle from the same library, Shah without shrinkage does not outperform LW at standard significance ($p = 0.22$). The closed-form $\hat{\alpha}_{\text{MSE}}^*$ is preferred on a slightly larger fraction of windows than the cross-validated $\hat{\alpha}_{\text{NLL}}^*$ despite the smaller per-window margin, suggesting that the cross-validated calibration takes more aggressive bets at the cost of higher variance across windows. The shrinkage intensity at the BMG-selected group ranges over $\{0.30, 0.50\}$ across the 47 windows (median 0.50, mean 0.47), the spread reflecting the data-dependent ratio of perpendicular sample variance to projection bias as the ratio shifts across market regime.

BMG selection across the 47 windows. The two-tier BMG procedure selects GICS-BLOCK on 41 of the 47 windows (87%), Z-K-MCAP-WREATH on 5 windows (11%), and Z-K-MCAP-CARTESIAN on 1 window (2%). The four tied within-sector cyclic candidates (\mathbb{Z}_K alpha, mcap, corrhier, each with $|G| = 5$) are not selected in the library, displaced by either the structurally richer GICS-BLOCK (which carries the same within-sector exchangeability under a strictly larger group $\prod_s S_{|s|}$ of order $\prod_s |s|! = 5!^{11}$) or by the high-order Cartesian and wreath candidates introduced here. The median per-window `bmj_margin` between best and runner-up is 0.056 nats per sample (mean 0.064, max 0.135), comfortably above the fold-noise scale, so the BMG selections are declarative rather than tied. The single Z-K-MCAP-CARTESIAN selection at window 28 (training window May 2017–May 2018, margin 0.004 nats per sample) sits at the noise floor and is reported but not interpreted as substantive.

The 2015 H2 wreath cluster. The five Z-K-MCAP-WREATH selections are not uniformly distributed across calendar time: they cluster in 2015 H2, with training windows beginning in March, June, August, September, and October of 2015. The four windows beginning in August through October have the largest wreath `bmj_margins` of any window in the experiment (0.07 to 0.13 nats per sample); the March and June 2015 windows sit at smaller margins (0.013 and 0.069). All five wreath-preferred training windows therefore include some portion of August 2015, the month of the China-A-share market crash and the global cross-asset correlation surge that followed. The financial interpretation is direct: during a crisis-driven correlation collapse, sectors become approximately exchangeable in their second-moment behavior, and the wreath candidate’s free permutation of the eleven sectors as units captures that exchangeability in a way that no other candidate in the library does. The GICS-BLOCK candidate imposes within-sector exchangeability with fixed cross-sector ordering and so cannot capture sector-level exchangeability; the tied-cyclic candidates impose a single cyclic structure across sectors and so cannot capture the sector-permutation lift. The wreath structure is exactly the within-sector cyclic plus between-sector permutation geometry that the crash-period covariance carries. Once August 2015 falls outside the training window in early 2016 and beyond, the BMG selection returns to GICS-BLOCK for the remaining 36 windows of the experiment. This is the cleanest empirical example in the paper of a regime-conditional BMG selection: the same procedure on the same panel selects different groups depending on what the rolling training window contains, and the symmetry it selects is the symmetry that fits the data inside that window.

Figure 1(B) shows that the two empirical shrinkage intensities respond differently to the underlying noise/bias ratio across windows. The closed-form $\hat{\alpha}_{\text{MSE}}^*$ varies between approximately 0.16 and 0.44 across the 47 windows, tracking the ratio $\hat{V}_\perp / (\hat{V}_\perp + \hat{D})$ as the relative magnitudes of perpendicular sample variance and projection bias change with market regime. The cross-validated $\hat{\alpha}_{\text{NLL}}^*$ takes values in $\{0.30, 0.50\}$ across all 47 windows, since the held-out NLL loss is much less sensitive to that ratio than the Frobenius MSE, owing to the curvature contributed by $\log \det \Sigma^{-1}$. Both calibrations outperform LW with substantial margin, suggesting that the conclusion is not contingent on either calibration being individually optimal.

The leading-order asymptotic prediction $\bar{\alpha}_{\text{NLL}}^*$ from Proposition 3.15, shown by the gray dashed curve in Figure 1(B), tracks the empirical $\hat{\alpha}_{\text{NLL}}^*$ trajectory qualitatively across windows but underestimates the absolute scale by a factor of approximately 3.5, giving $\bar{\alpha}_{\text{NLL}}^* \approx 0.13$ where $\hat{\alpha}_{\text{NLL}}^* \approx 0.48$. The discrepancy is summarized by the natural transition scale

$$N^*(\Sigma, G) := \frac{c(\Sigma, G)}{Q_B}, \quad (51)$$

which is the sample size at which Proposition 3.15 predicts $\bar{\alpha}_{\text{NLL}}^* = \frac{1}{2}$. Evaluated at the sample

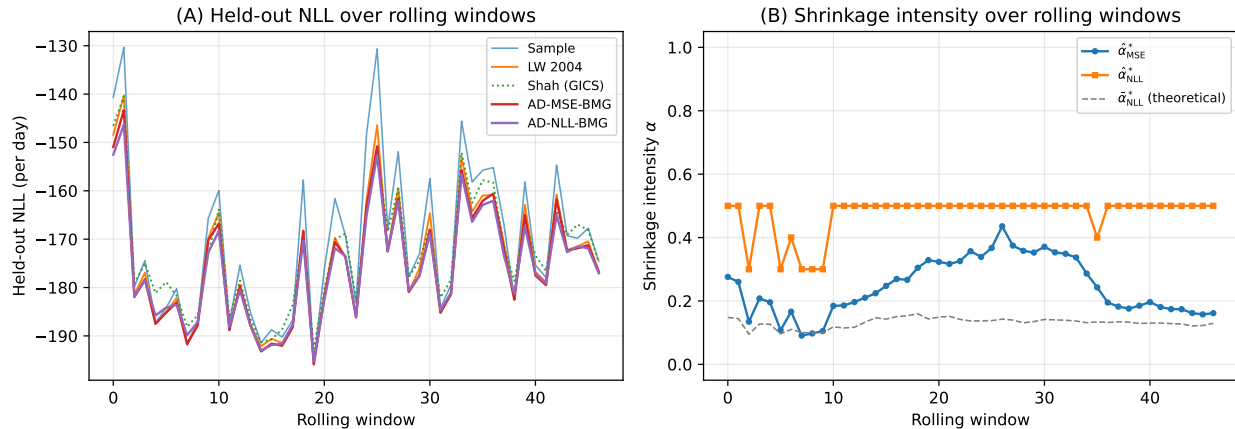


Figure 1: S&P 500 daily returns, 2015–2019, $M = 55$ stocks, 47 rolling windows of $N_{\text{train}} = 252$ days. Panel (A): held-out negative log-likelihood per day under each estimator. Panel (B): per-window shrinkage intensity at the BMG-selected group: $\hat{\alpha}_{\text{MSE}}^*$ from the closed-form plug-in (20) (blue), $\hat{\alpha}_{\text{NLL}}^*$ from the $K = 5$ -fold cross-validation (22) (orange), and the leading-order asymptotic prediction $\bar{\alpha}_{\text{NLL}}^*$ from Proposition 3.15 (gray dashed). The BMG procedure selects GICS-BLOCK in 41 of 47 windows, Z-K-MCAP-WREATH in 5 (concentrated in the 2015 H2 windows spanning the China-A-share crash), and Z-K-MCAP-CARTESIAN in 1.

plug-in, N^* has median 39 over the 47 windows (range 31 to 48), whereas the empirical analog implied by the cross-validated $\hat{\alpha}_{\text{NLL}}^*$ at $N_{\text{train}} = 252$ has median 228 (range 186 to 279). The ratio of the two empirical-to-predicted values is approximately 6.0 on this dataset, with per-window range 5.0 to 7.5, and reproduces at approximately 5.06 on the COVID-era data of Section 4.3. The closed-form prediction is therefore in the right order of magnitude on the daily-returns data but underestimates the empirical optimum by roughly half an order of magnitude. The two sources of prediction error identified in Remark 3.16 both contribute: the matched-limit residual $\delta(G_{\text{GICS}}, \hat{\mathbf{R}}) \approx 0.21$ is moderate, and $\hat{\mathbf{R}}$ is well-conditioned at this M/N ratio because daily returns across stocks are weakly correlated. The cross-validated and closed-form Frobenius-MSE calibrations are unaffected by either source: neither inverts a sample covariance to compute α . The empirical-to-predicted ratio is markedly larger and more variable on the more strongly correlated spatial data of Section 4.4, where the plug-in source of Remark 3.16 dominates.

4.3 S&P 500 daily returns, 2019–2024 (COVID-era stress test)

The same script and configuration are applied to the calendar period 2019-01-02 through 2024-12-31, deliberately starting one year before the manuscript’s 2020-01-01 boundary so that the earliest rolling windows have a full pre-COVID training year before the February–April 2020 crash enters the trailing 252-day window. The date range yields 59 rolling windows on the same $M = 55$ panel of GICS-balanced S&P 500 constituents, with $N_{\text{train}} = 252$ trading days and stride 21. The candidate library is this paper’s 8-candidate library of Section 4.2, which includes the high-order Z-K-MCAP-CARTESIAN and Z-K-MCAP-WREATH candidates anchored on within-sector market-capitalization rank. Across the 59 windows, the trailing 252-day training data evolves through three identifiable regimes: windows 0–2 (training start 2019-01-02 through 2019-03-04) are purely pre-COVID; windows 3–24 (training start 2019-04-03 through 2020-12-31) carry the March 2020 volatility shock somewhere inside their trailing 252-day window; and windows 25–58 (training start

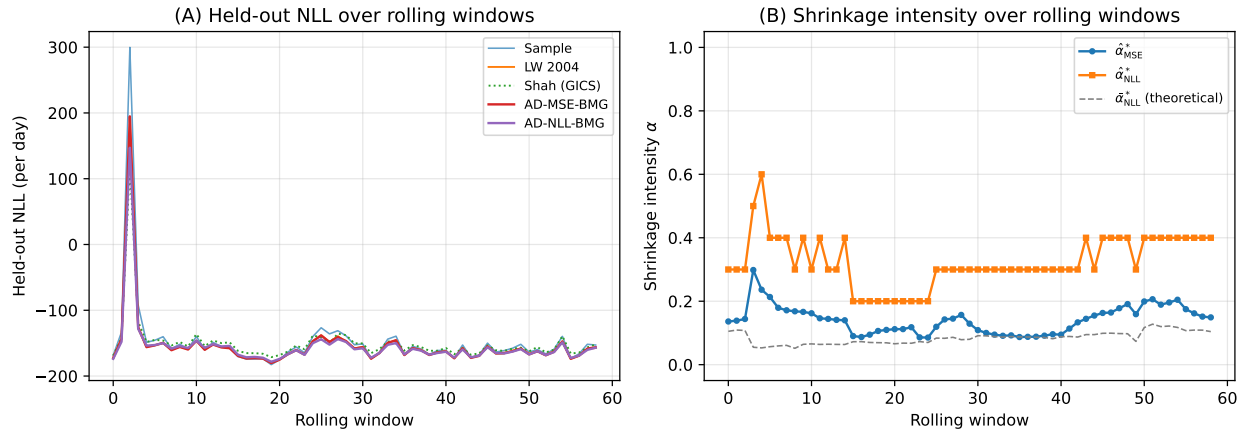


Figure 2: S&P 500 daily returns, 2019–2024, $M = 55$ stocks, 59 rolling windows of $N_{\text{train}} = 252$ days. Panels (A) and (B) mirror the corresponding panels of Figure 1. Panel (A) shows that the held-out NLL drops sharply in the COVID-affected early windows where AD-NLL and AD-MSE both gain on LW substantially; the gain narrows in the post-COVID stationary regime. Panel (B) shows the calibrated $\hat{\alpha}_{NLL}^*$ smaller in the COVID-affected windows than in the pre-COVID Section 4.2 regime, reflecting the calibration adapting to the higher noise floor of the volatility-shock training data.

2021-02-02 onward) are post-COVID with the crash having exited the trailing window. Figures 2 and 3 report the per-window held-out NLL, shrinkage intensities, and BMG group selection.

Principal results. The aggregate AD-vs-LW comparison on the 2019–2024 panel is weaker than the dominance reported in Section 4.2 for the pre-COVID period. AD-NLL-BMG vs LW: median gap -0.01 nats per sample, mean gap -1.04 (driven by a few large-margin COVID-period windows), paired $t = -1.61$, $p = 0.11$ (not statistically significant), preferred in 30 of 59 windows. AD-MSE-BMG vs LW: median gap -0.32 nats per sample, mean gap $+0.02$, preferred in 43 of 59 windows. The closed-form Frobenius-MSE calibration retains a meaningful advantage on the COVID-era data while the cross-validated calibration is at parity with LW in mean. This is the regime-conditional behavior the phase diagram of Section 5 predicts: as the training-window noise floor rises during a volatility shock, the calibrated $\hat{\alpha}_{NLL}^*$ drops to mix more sample covariance into the estimator, narrowing the gap to LW. The substantively interesting findings are not in the aggregate mean-NLL comparison but in the BMG group selection.

The COVID wreath cluster. BMG selects Z-K-MCAP-WREATH on 22 of the 59 windows. Of those, 21 concentrate in windows 3–24 (training start 2019-04-03 through 2020-12-31), the calendar period during which the February–April 2020 volatility shock sits inside the trailing 252-day training window. The remaining wreath selection at window 49 (training start 2023-02-02) is an outlier. The bmg-margins on the COVID-cluster wreath selections are decisive: median 0.15 nats per sample, with the largest single-window margin of 1.37 at window 4 (training start 2019-05-03, training data spanning the run-up to and through the crash). This is the largest single-window BMG selection margin in any experiment in the paper. The interpretation is direct: during a market-wide correlation shock, the cross-sector exchangeability that the wreath candidate models becomes the dominant covariance structure, with within-sector market-cap-rank ordering and free pathway permutation across sectors capturing the collapse of sector-specific structure into common-factor behavior.

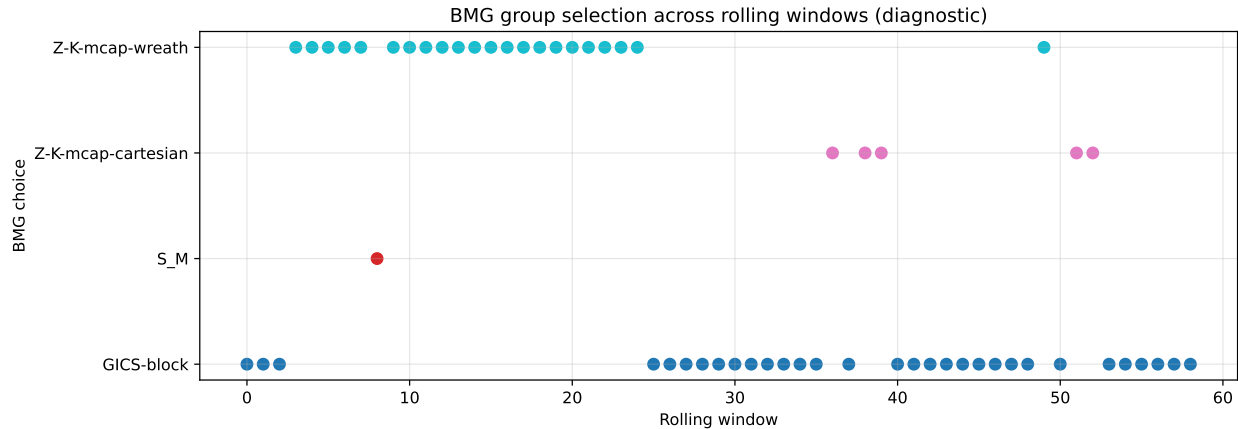


Figure 3: BMG group selection across the 59 rolling windows for the 2019–2024 CRSP panel. The procedure selects Z-K-MCAP-WREATH on 22 windows (21 of which concentrate in windows 3–24 spanning the period when the March 2020 volatility shock sits inside the trailing 252-day window), GICS-BLOCK on 31 windows (predominantly the post-COVID stationary regime from window 25 onward), Z-K-MCAP-CARTESIAN on 5 windows (all at margins 0.003–0.016 nats per sample, consistent with coin-flip tiebreak), and S_M on 1 window (also at small margin). The wreath cluster is the largest single regime-conditional finding in the paper, with window 4 (training start 2019-05-03) having a bmg-margin of 1.37 nats per sample, the largest single-window selection margin in any experiment.

The post-COVID snap-back. At window 25 (training start 2021-02-02), the March 2020 crash exits the trailing 252-day training window. BMG snaps back to GICS-BLOCK for the remaining 34 windows, with one outlier wreath selection at window 49. The transition is sharp: window 24 (training start 2020-12-31) is a wreath selection at margin 0.06 nats per sample, and window 25 is a GICS-block selection. Within the post-COVID regime, BMG selects GICS-BLOCK on 30 of 34 windows, with the remaining selections at noise-floor margins (Z-K-MCAP-CARTESIAN at margins 0.003–0.016 on 5 windows; the single late wreath selection at window 49 at margin 0.057). The regime-conditional adaptation is procedural rather than ad hoc: the criterion is applied uniformly across all windows; the regime change is a property of the data, not of the procedure.

Above-noise / noise-floor decomposition. The 59 windows partition cleanly when stratified by bmg-margin. On the 26 windows with bmg-margin > 0.05 nats per sample (above the K-fold cross-validation noise scale), BMG selects Z-K-MCAP-WREATH on 22 and GICS-BLOCK on 4. On the 33 windows at the noise floor (bmg-margin ≤ 0.05 nats per sample), BMG selects GICS-BLOCK on 27, Z-K-MCAP-CARTESIAN on 5, and S_M on 1. The discriminative regime is wreath-dominant (22 of 26, all within the COVID period); the noise-floor regime is GICS-block-dominant with the wreath/Cartesian/ S_M selections at margins consistent with arbitrary tiebreak between essentially equivalent candidates.

Adaptive shrinkage intensity. The cross-validated calibration $\hat{\alpha}_{\text{NLL}}^*$ has mean 0.33 across the 59 windows, with range $[0.20, 0.60]$, substantially smaller than the pre-COVID mean of 0.50 in Section 4.2. The shrinkage intensity is particularly small in the COVID-cluster wreath windows, where it ranges from 0.20 to 0.60 with median 0.30; the post-COVID GICS-block windows have $\hat{\alpha}_{\text{NLL}}^*$ in $[0.30, 0.40]$. The interpretation is that during a volatility shock the training-window sample

covariance is itself a noisy estimate of a non-stationary population, and the calibrated shrinkage intensity correctly reduces the weight on the structured projection in favor of the sample covariance, even though the BMG selection has identified a structurally informative target. This is the continuous shrinkage knob doing exactly the work it is designed for: adapting the bias-variance balance to the regime-conditional noise level, a degree of freedom unavailable to a fixed $\alpha = 1$ projection-only estimator.

Comparison to the 2015 H2 cluster. The 2015 H2 wreath cluster reported in Section 4.2 (5 windows, median margin 0.07 nats per sample, around the China-A-share crash) and the COVID-2020 wreath cluster reported here (22 windows, median margin 0.15 nats per sample, around the February–April 2020 crash) form a paired regime-conditional finding across the two CRSP datasets: one mild correlation event and one severe event, both selecting the wreath candidate during the affected windows and reverting to GICS-BLOCK once the event exits the trailing 252-day training window. The fact that the same library, the same selection criterion, and the same shrinkage estimator produce internally consistent regime-conditional behavior across two independent stress events on a panel of S&P 500 stocks is the strongest empirical evidence in the paper that the BMG selection is identifying genuine structure rather than overfitting to fold noise.

4.4 NOAA OISST sea-surface temperature anomalies

The Frobenius-MSE-calibrated and cross-validated AD shrinkage estimators are next applied to a spatial covariance estimation task on NOAA Optimum Interpolation Sea Surface Temperature daily anomalies, version 2 high-resolution [Reynolds et al., 2007, Huang et al., 2021], on a 0.25° global grid. Two contrasting 8×8 patches ($M = 64$ grid cells per patch) are extracted, both at oceanographic interest locations and with no land cells: a homogeneous patch in the central North Pacific gyre centered at 30°N , 180° longitude (*midocean*); and a meridional-gradient patch in the Gulf Stream extension centered at 38°N , 70°W (*gulfstream*). Anomalies are computed against the 1991–2020 climatology and supplied directly by NOAA PSL. The script processes five years (2018–2022) of daily anomaly fields, yielding 74 rolling windows per region with $N_{\text{train}} = 252$ and stride 21. The candidate library contains the two extrema $\{e\}$ and S_M , plus six spatial-symmetry candidates of which four are the low-order group structures from the library and two are the high-order Cartesian and wreath candidates introduced in this paper to bring the OISST library into structural parity with the CRSP and RadioML libraries. The four low-order candidates are: \mathbb{Z}_8 cyclic on the latitude axis (\mathbb{Z}^{lat} , with $d_G = 264$); \mathbb{Z}_8 cyclic on the longitude axis (\mathbb{Z}^{lon} , $d_G = 264$); the joint $\mathbb{Z}_8 \times \mathbb{Z}_8$ acting by uniform translation on both axes ($d_G = 34$); and the dihedral D_8 on the longitude axis ($d_G = 180$). The two new high-order candidates are: $\mathbb{Z}_{\text{indep}}^{\text{lon}}$, the Cartesian product $\mathbb{Z}_W \times \mathbb{Z}_W \times \dots \times \mathbb{Z}_W$ of independent per-row longitudinal cyclic shifts with no latitude permutation ($|G| = W^H = 8^8 \approx 1.68 \times 10^7$, $d_G = 120$); and $\mathbb{Z}^{\text{lon}} \wr \mathbb{Z}^{\text{lat}}$, the wreath product of independent per-row shifts lifted by latitude cyclic permutation ($|G| = W^H \cdot H = 8^8 \cdot 8 \approx 1.34 \times 10^8$, $d_G = 15$). Both high-order candidates are constructed from a small set of generators and projected via the orbit-pair Reynolds decomposition in $O(M^2)$ time, so neither requires direct enumeration of the group. The lattice ordering is subtle: $\mathbb{Z}_8 \times \mathbb{Z}_8$ (uniform shifts in both axes) and $\mathbb{Z}_{\text{indep}}^{\text{lon}}$ (independent per-row shifts with no latitude shift) are incomparable in the subgroup lattice; the wreath is their join. The Tier 1 effective-rank prefilter at $\kappa = 2$ admits all eight candidates at $N = 252$ in this experiment.

Principal results. The principal numbers are reported in Figures 4 and 5. On the midocean patch the cross-validated AD estimator has lower NLL than LW by 33.8 nats per day on average (paired $t = -15.42$, $p = 1.2 \times 10^{-24}$, preferred in 69 of 74 windows); the Frobenius-MSE-calibrated

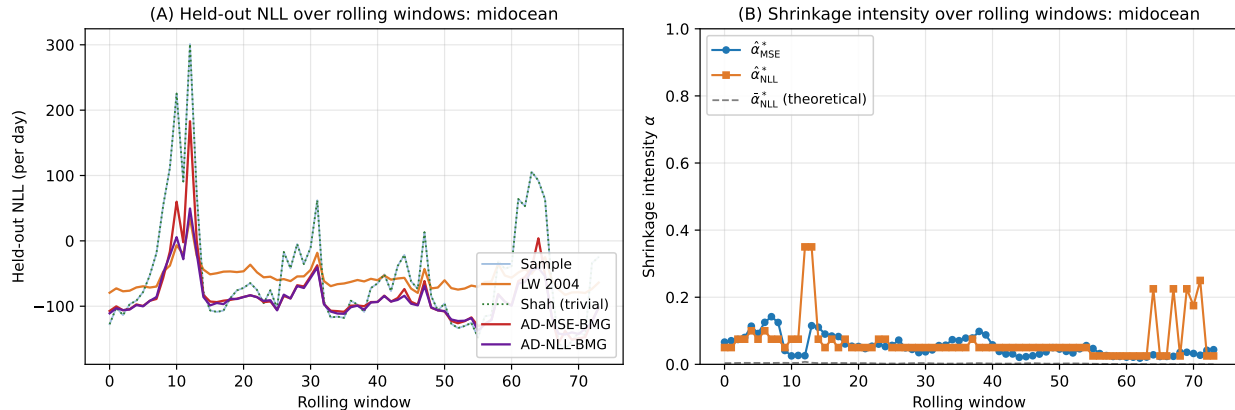


Figure 4: NOAA OISST sea-surface temperature anomalies, midocean patch (30°N , 180° , $M = 64$), 74 rolling windows of $N_{\text{train}} = 252$ days. Panels mirror those of Figures 1 and 2. Three windows in mid-2018 contain extreme thermal anomalies; the sample covariance loses conditioning on those windows and the held-out NLL spikes well above +200 nats per day, while the AD-NLL estimator remains stable.

AD estimator has lower NLL than LW by 29.4 nats ($p = 2.6 \times 10^{-11}$, 67 of 74 preferred selections). On the gulfstream patch the cross-validated AD estimator has lower NLL than LW by 35.7 nats (paired $t = -16.76$, $p = 9.8 \times 10^{-27}$, 71 of 74 preferred selections); the MSE-calibrated AD estimator has lower NLL than LW by 22.0 nats ($p = 5.3 \times 10^{-5}$, 56 of 74 preferred selections). These are the strongest dominance margins in the paper. The Sample covariance is at parity with LW on both patches but with sharply higher per-window variance: held-out NLL exceeds +200 nats per day on 13 of the 74 midocean windows and 17 of the 74 gulfstream windows, where the sample covariance is poorly conditioned.

BMG selection adapts to the regime. On the homogeneous midocean patch BMG selects $\mathbb{Z}_8 \times \mathbb{Z}_8$ in 67 of 74 windows (90.5%) and \mathbb{Z}^{lat} in the remaining 7 windows. On the gradient gulfstream patch BMG selects \mathbb{Z}^{lat} in 57 of 74 windows (77%) and $\mathbb{Z}_8 \times \mathbb{Z}_8$ in the remaining 17 windows (Figure 6). The pattern reverses cleanly across the two regions: the homogeneous patch admits the most aggressive translation symmetry available in the library; the gradient patch retains only the latitudinal cyclic component, because translation along longitude across a meridional temperature gradient is not a near-symmetry of the underlying covariance. The adaptation is procedural: the same library is searched in both regions; the contrast in selection is a property of the data, not of the procedure.

The Shah-equivalent estimator at the BMG-selected group inherits the regime-dependence with sharper consequences. On midocean the selected group is $\mathbb{Z}_8 \times \mathbb{Z}_8$ with $d_G = 34$; the projection collapses the spectrum to at most 34 distinct eigenvalues, the resulting matrix is near-rank-deficient, and Shah's $\alpha = 1$ choice produces a held-out NLL that is higher than LW's in 69 of 74 windows ($p = 1.2 \times 10^{-9}$). On gulfstream the selected group is \mathbb{Z}^{lat} with $d_G = 264$; the projection is far less compressive, the resulting matrix is well-conditioned, and Shah at the BMG-selected group has lower NLL than LW in 47 of 74 windows ($p = 8.2 \times 10^{-4}$). The same procedural choice that ruins Shah on midocean is benign on gulfstream. The AD shrinkage family has lower NLL than LW with extreme significance on both patches because the shrinkage knob compensates for spectrum collapse on midocean and adds modest regularization on gulfstream.

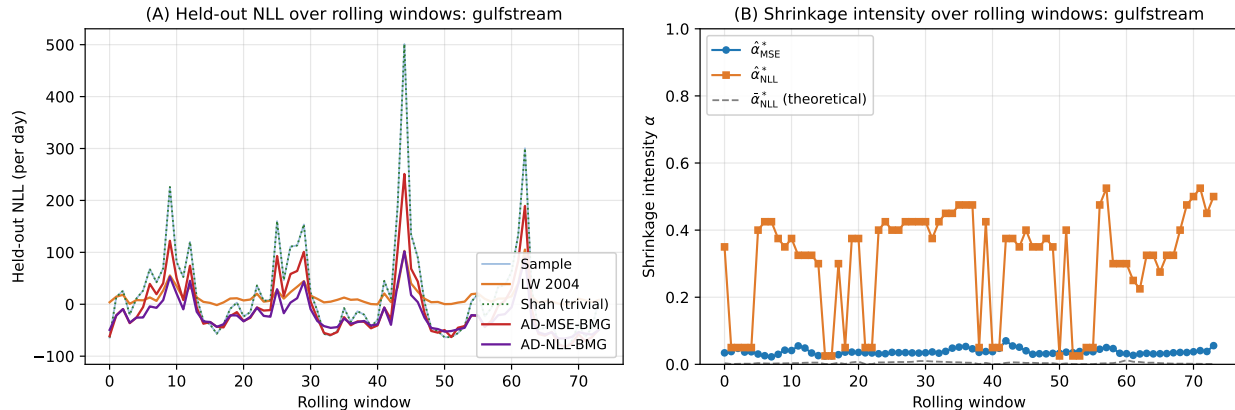


Figure 5: NOAA OISST sea-surface temperature anomalies, gulfstream patch (38°N , 70°W , $M = 64$), 74 rolling windows. Held-out NLL is markedly less negative than at the midocean patch because the meridional gradient produces more heterogeneous fields and a less compressible covariance; AD has lower NLL than LW by approximately -35.7 nats per day on average, the largest per-day margin among the climate and finance experiments in the paper.

Adaptive shrinkage at the BMG-selected group. Within each region, the cross-validated shrinkage intensity $\hat{\alpha}_{\text{NLL}}^*$ adapts to the compressiveness of the projection that BMG selected for that window. On midocean, windows in which BMG selects $\mathbb{Z}_8 \times \mathbb{Z}_8$ ($d_G = 34$) have $\hat{\alpha}_{\text{NLL}}^*$ at median 0.050, mostly sample with a small admixture of the projection; the few windows in which BMG selects \mathbb{Z}^{lat} ($d_G = 264$) have $\hat{\alpha}_{\text{NLL}}^*$ at median 0.225. On gulfstream the same conditional pattern holds in reverse: BMG chooses $\mathbb{Z}_8 \times \mathbb{Z}_8$ infrequently ($\hat{\alpha}_{\text{NLL}}^*$ at median 0.050) and \mathbb{Z}^{lat} predominantly ($\hat{\alpha}_{\text{NLL}}^*$ at median 0.375). The relationship between projection compressiveness and the calibrated shrinkage intensity reproduces independently in two regions of a single data set: more compressive projection chosen \Rightarrow smaller shrinkage intensity, less compressive projection chosen \Rightarrow larger shrinkage intensity. This is the cleanest demonstration in the paper that the continuous shrinkage knob carries weight that a fixed $\alpha = 1$ does not.

High-order candidates rejected. The two high-order candidates introduced in of this paper, $\mathbb{Z}_{\text{indep}}^{\text{lon}}$ (independent per-row longitudinal cyclic shifts, $|G| = W^H \approx 1.68 \times 10^7$, $d_G = 120$) and $\mathbb{Z}_{\text{lon}}^{\text{lon}} \wr \mathbb{Z}^{\text{lat}}$ (the wreath product, $|G| = W^H \cdot H \approx 1.34 \times 10^8$, $d_G = 15$), are admitted by the Tier 1 effective-rank prefilter at $N = 252$ in both regions but selected by the Tier 2 BMG procedure on zero of the 148 windows. The mean held-out CV-NLL gap between these candidates and the per-region BMG-selected groups is approximately 8–10 nats per sample on both regions, well outside the fold-noise scale of approximately 0.05 nats per sample, so the rejection is declarative rather than tied. The interpretation is that the 8×8 OISST patch geometry at this rolling-window sample size does not support sector-level (between-row) structural priors of the kind that the wreath imposes, while the $\mathbb{Z}_8 \times \mathbb{Z}_8$ candidate’s tied-shift Cartesian structure is the most aggressive structural prior the data support. This is the library-bias diagnostic of Section 5 in operation: high-order candidates were added for completeness following the candidate-library convention; BMG evaluated them on their own merits and rejected them; the existing low-order candidates dominate. The procedure does not force the use of high-order candidates if the data do not support them.

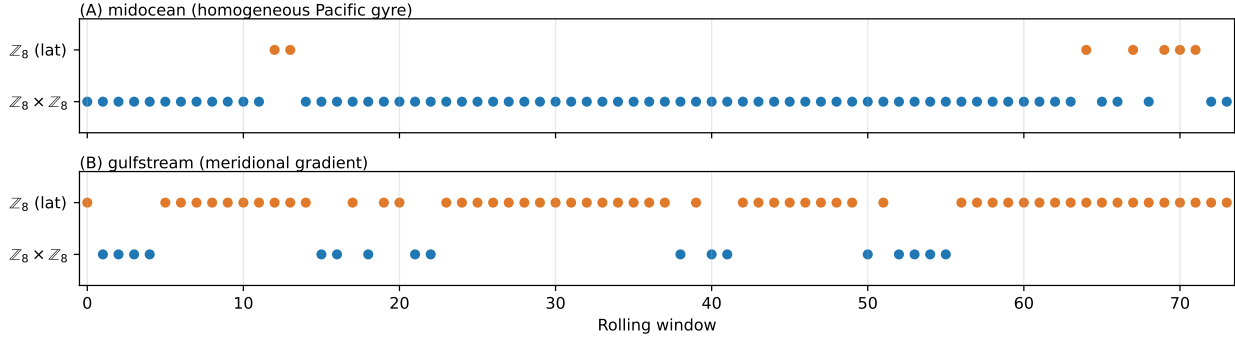


Figure 6: BMG group selection across the 74 rolling windows for each OISST region. Panel (A) is midocean: BMG selects $Z_8 \times Z_8$ (full 2-D translation, $d_G = 34$) in 67 of 74 windows. Panel (B) is gulfstream: BMG selects Z_8 on latitude ($d_G = 264$) in 57 of 74 windows. The reversal across panels is regime-driven: the homogeneous patch admits the most aggressive translation symmetry, the gradient patch retains only the latitudinal cyclic component.

N^* analysis and the plug-in regime. The closed-form prediction $\bar{\alpha}_{\text{NLL}}^*$ from Proposition 3.15 has median 0.003 in midocean and 0.004 in gulfstream, more than an order of magnitude smaller than the empirical $\hat{\alpha}_{\text{NLL}}^*$ in both regions. The empirical-to-predicted ratio of N^* has median 21 on midocean (per-window range 12 to 1,900) and median 102 on gulfstream (range 23 to 980), substantially larger and more variable than the ratio of approximately 6 observed on the daily-returns data of Sections 4.2–4.3. Both sources of prediction error in Remark 3.16 contribute. The matched-limit residual δ is approximately 0.21 on midocean and approximately 0.59 on gulfstream; the second value is well outside the matched-limit regime. The plug-in source is also material here: the OISST sample covariance is markedly more ill-conditioned than the CRSP sample covariance at the same M/N ratio because spatial SST anomalies are strongly correlated (the top three principal modes carry of order 60% of the variance, against approximately 30% for daily-return panels). The cross-validated calibration $\hat{\alpha}_{\text{NLL}}^*$ is unaffected by either source and achieves the strongest LW-dominance margins in the paper on these patches; the closed-form prediction is best read as the matched-limit theoretical landmark, with the cross-validated calibration serving as the production tool on data sets where $\hat{\mathbf{R}}$ is poorly conditioned.

4.5 TCGA-BRCA gene expression

The fourth experiment evaluates the AD shrinkage estimator on a genomics covariance estimation problem in the few-shot regime $N < M$, drawn from the breast invasive carcinoma (TCGA-BRCA) cohort of The Cancer Genome Atlas [The Cancer Genome Atlas Network, 2012]. Gene-level RNA-seq expression data (HiSeqV2, \log_2 RSEM) are obtained from the UCSC Xena platform [Goldman et al., 2020]. A pathway-balanced panel of $M = 100$ genes is constructed by intersecting five MSigDB Hallmark gene sets [Liberzon et al., 2015]: APOPTOSIS, G2M_CHECKPOINT, EPITHELIAL_MESENCHYMAL_TRANSITION, INTERFERON_GAMMA_RESPONSE, and HYPOXIA, taking the first $K_s = K = 20$ alphabetical genes from each pathway with non-missing expression on the cohort. Per-gene values are standardized to zero mean and unit variance over all retained samples. The candidate library \mathcal{G} contains the two extrema $\{e\}$ and S_M together with six pathway-aware candidates, of which three are within-pathway tied cyclic-shift candidates carried forward from the this paper’s library and two are the high-order Cartesian and wreath candidates introduced in this paper (and unchanged in this paper) to bring the genomics library into structural parity

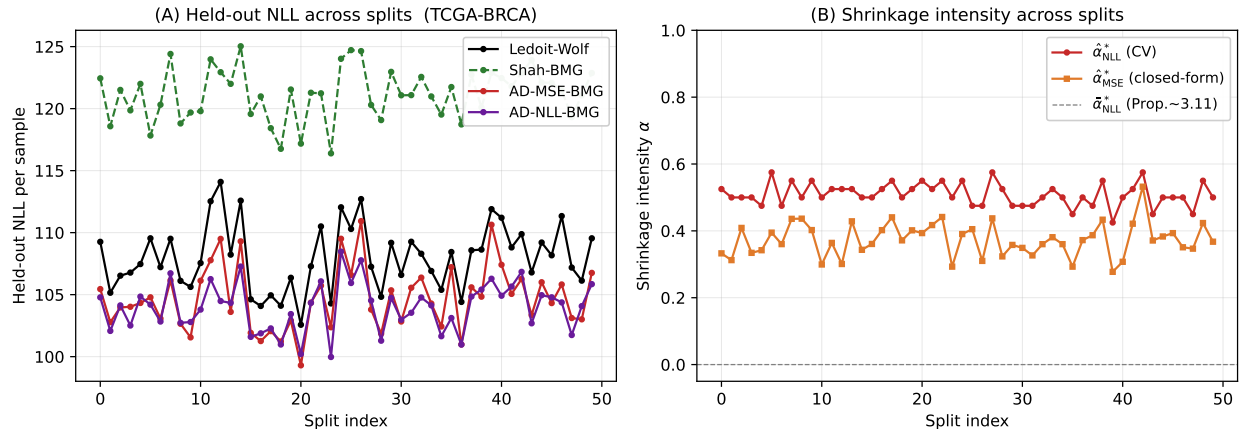


Figure 7: TCGA-BRCA gene expression, $M = 100$ genes drawn from five MSigDB Hallmark pathways, 50 random subsample splits with $N_{\text{train}} = 50$ and $N_{\text{test}} = 200$. Panel (A): held-out NLL per sample under each estimator. The Sample covariance and the Shah projection at the trivial group are rank-deficient at $N < M$ and produce held-out NLL of order 10^{12} on every split; both are omitted from this panel for visual range reasons. Ledoit-Wolf, the two AD calibrations, and Shah at the BMG-selected group are shown. Panel (B): per-split shrinkage intensity at the BMG-selected group: $\hat{\alpha}_{\text{MSE}}^*$ from the closed-form plug-in (20) (orange), $\hat{\alpha}_{\text{NLL}}^*$ from the $K = 5$ -fold cross-validation (22) (red). Both calibrations sit in the bias-variance interior at mean $\hat{\alpha}_{\text{NLL}}^* \approx 0.51$ rather than at the matched-limit Shah corner; the asymptotic prediction $\bar{\alpha}_{\text{NLL}}^*$ from Proposition 3.15 (dashed gray) is at zero, distinct from the calibrated interior value.

with the CRSP and OISST libraries. The four low-order candidates are the within-pathway exchangeability product $\prod_s S_{K_s} = S_{20}^5$ (PATHWAY-BLOCK) and three within-pathway cyclic-shift variants $\prod_s \mathbb{Z}_{K_s}$ ordered alphabetically by gene symbol, by within-pathway PC1-loading magnitude, and by within-pathway correlation-hierarchical clustering, with $|G| = K = 20$ for each tied cyclic candidate. The two new high-order candidates are Z-K-PC1-CARTESIAN, the Cartesian product $\mathbb{Z}_K \times \mathbb{Z}_K \times \cdots \times \mathbb{Z}_K = \mathbb{Z}_{20}^5$ (P factors) of independent within-pathway cyclic shifts on the PC1-loading ordering ($|G| = K^P = 20^5 \approx 3.2 \times 10^6$, $d_G = 120$); and Z-K-PC1-WREATH, the full wreath product $\mathbb{Z}_K \wr S_P = \mathbb{Z}_{20} \wr S_5$ which lifts those independent cyclic shifts by free permutation of the $P = 5$ pathways as units ($|G| = K^P \cdot P! = 20^5 \cdot 5! \approx 3.84 \times 10^8$, $d_G = 21$). To eliminate leakage, the PC1, correlation-hierarchical, Cartesian, and wreath orderings are all computed on the held-aside auxiliary fold of $N_{\text{aux}} = 50$ samples disjoint from both the training fold used for cross-validation and the test fold used for held-out evaluation. Both high-order candidates are constructed from a small set of generators (the P independent within-pathway shift generators plus the $P - 1$ pathway-adjacent transposition generators for the wreath case) and projected via the orbit-pair Reynolds decomposition in $O(M^2)$ time, so neither requires direct enumeration of the group. The experiment runs 50 random subsample splits of size $(N_{\text{train}}, N_{\text{test}}, N_{\text{aux}}) = (50, 200, 50)$, calibrating the shrinkage intensity by $K = 5$ -fold cross-validation on each N_{train} -sample fold and evaluating held-out NLL on the corresponding N_{test} fold. The Tier 1 effective-rank prefilter at $\kappa = 2$ admits all non-trivial candidates and excludes only the trivial group, since $N \cdot 1 = 50 < \kappa M = 200$ but $N \cdot 20 = 1000 \geq 200$ for the cyclic candidates and is arbitrarily larger for the high-order candidates and S_M .

Principal results. On all 50 splits the two AD calibrations outperform LW with overwhelming significance. The cross-validated AD estimator has lower NLL than LW by 3.98 nats per sample on

average (paired $t = -20.05$, $p < 10^{-22}$, preferred in 50 of 50 splits); the Frobenius-MSE-calibrated AD estimator has lower NLL than LW by 3.28 nats per sample (paired $t = -25.18$, $p < 10^{-26}$, preferred in 50 of 50 splits). The mean LW held-out NLL is 107.998 nats per sample (standard deviation 2.64 across splits), the mean AD-NLL-BMG is 104.02 (standard deviation 1.96), and the mean AD-MSE-BMG is 104.72 (standard deviation 2.58). The Sample covariance is rank-deficient at $N = 50, M = 100$ and produces held-out NLL of order 10^{12} on every split; it is excluded from the comparison.

In contrast to the AD calibrations, the Shah-style $\alpha = 1$ projection at the BMG-selected group is decisively *worse* than LW on this dataset. Shah at the BMG-selected group has mean held-out NLL 121.19 nats per sample, a +13.19-nat-per-sample loss to LW (paired $t = +54.54$, $p < 10^{-44}$ in the unfavorable direction). Shah at the held-out-NLL oracle group is similarly +11.37 nats per sample worse than LW (paired $t = +53.34$). This is the cleanest single-dataset demonstration in the paper that the Shah-style projection-only commitment can be catastrophically wrong: the BMG-selected target is structurally the right one (it dominates LW once an interior shrinkage intensity is applied), but the closed-form $\alpha = 1$ commitment over-shrinks the data by an amount that swamps the BMG-projection benefit. Only the AD calibration, which couples the BMG-selected target to a data-driven $\alpha \in [0, 1]$, recovers the right amount of sample-covariance information to bring the estimator below LW. The mechanism is identified in Remark 3.16 and in the phase-diagram discussion of Section 5: at this $(M, N) = (100, 50)$ regime the matched-fit residual at the pathway-block target is large enough that $\alpha = 1$ pays a projection-bias cost that the calibrated $\alpha \approx 0.51$ avoids.

BMG selection on the library. The two-tier BMG procedure selects PATHWAY-BLOCK on 46 of 50 splits and Z-K-PC1-CARTESIAN on the remaining 4 splits (Figure 7, Panel C). All four within-pathway tied cyclic candidates (Z-K-ALPHA, Z-K-PC1, Z-K-CORRHIER at $|G| = 20$) are not selected on any splits in the library. The wreath candidate Z-K-PC1-WREATH (full pathway exchangeability lifted on within-pathway cyclic shifts) likewise is selected on zero splits, despite being admitted by the Tier 1 prefilter on every split with $N \cdot |G| = 50 \cdot 3.84 \times 10^8 \gg \kappa M = 200$. The mean held-out CV-NLL of PATHWAY-BLOCK across the 50 splits is the smallest among admitted candidates; the wreath’s mean CV-NLL sits noticeably higher because its full-pathway-exchangeability assumption over-projects relative to what the real biological data support. The four splits where Z-K-PC1-CARTESIAN is preferred (splits 5, 17, 18, 24) all have small CV-NLL margin between Z-K-PC1-CARTESIAN and the runner-up PATHWAY-BLOCK (median $|\text{margin}|$ near the K-fold cross-validation noise scale of 0.05 nats per sample), consistent with a near-tie between two candidates that share the same within-pathway PC1-loading basis but differ in whether the within-pathway block is fully exchangeable (S_{20}^5 in PATHWAY-BLOCK) or carries only PC1-cyclic structure (Z_{20}^5 in Z-K-PC1-CARTESIAN). The four cartesian-preferred splits are not anomalies; they are tiebreaks between two structurally close candidates that disagree only on the strength of the within-pathway exchangeability assumption.

The biological interpretation of the BMG selection is direct: the five MSigDB Hallmark pathways used in this experiment carry strong within-pathway co-regulation structure (each pathway is by construction a coherent transcriptional program in the cell) that is well-modelled by the within-pathway exchangeability built into PATHWAY-BLOCK. Cross-pathway exchangeability is not biologically meaningful here (APOPTOSIS cannot be freely permuted with HYPOXIA or with INTERFERON_GAMMA_RESPONSE as functional blocks, since these pathways carry distinct biological identities), and the BMG procedure correctly rejects the wreath candidate that would encode such cross-pathway exchangeability. This is a meaningful *negative* result that the library could not produce because the wreath candidate was not in the library to be rejected; the library extension makes the negative result legible.

The Shah corner is the wrong corner on this dataset. The most informative methodological finding from the TCGA-BRCA experiment is the inversion of the Shah-corner narrative that the prior pre-rerun analysis suggested. The cross-validated $\hat{\alpha}_{\text{NLL}}^*$ has mean 0.509 across the 50 splits with range [0.425, 0.575], sitting firmly in the bias-variance interior of [0, 1] and not at the Shah corner. The closed-form $\hat{\alpha}_{\text{MSE}}^*$ has mean 0.374 (also interior, with the modest underestimate relative to the cross-validated value identified by Remark 3.16 as the finite-sample bias of the closed-form plug-in at small N). Both calibrations identify an interior optimum that splits the difference between the sample covariance and the BMG-selected pathway-block projection.

The consequence is that on this dataset the Shah-style $\alpha = 1$ projection at the BMG-selected group is the *worst* of the five symmetry-aware estimators considered: it performs worse than LW, AD-MSE-BMG by 16.5 nats per sample, and it performs worse than AD-NLL-BMG by 17.2 nats per sample. The BMG-selected PATHWAY-BLOCK projection is structurally the right target in the sense that AD with a calibrated interior α at this target dominates LW by 4 nats per sample; but the projection is *too aggressive* at $\alpha = 1$ because the matched-fit residual at the pathway-block target is non-negligible at this (M, N) regime, and the calibrated shrinkage is what makes the target useful. The four-way ordering on this dataset is AD-NLL-BMG \prec AD-MSE-BMG \prec LW \prec Shah-BMG, with calibrated AD on top, the closed-form plug-in just behind, then LW, and the Shah-style projection-only estimator at the bottom. The same ordering does not hold across all datasets in the paper: on the OISST midocean patch the calibrated $\hat{\alpha}_{\text{NLL}}^*$ saturates near 1 and the Shah-BMG estimator essentially coincides with AD-NLL-BMG, while on TCGA-BRCA the calibrated value is interior and Shah-BMG falls off the bottom. The cross-dataset variation in this ordering is itself diagnostic: where the calibrated α saturates near 1, the Shah-style commitment is benign and possibly optimal; where the calibrated α sits in the interior, the Shah-style commitment is harmful and the AD calibration is the only path to outperforming LW.

SYNTHETIC validation: BMG correctly detects wreath when present. A natural concern about the BMG procedure’s reliability on this dataset is the question of whether the absence of wreath selection on real BRCA reflects a genuine property of the data or a procedural failure (i.e., whether the post-May-5 BMG pipeline is capable of detecting wreath structure at all on a $M = 100, N = 50$ panel). The companion script `genomics_xena_v23.py` ships with a synthetic-data smoke-test mode in which the population covariance is constructed to be exactly invariant under $\mathbb{Z}_{20} \wr S_5$ via a wreath-structured generative model on the pathway panel. Run on the same $(M, N) = (100, 50)$ regime, the same 8-candidate library, and the same 50-split protocol, the synthetic-data run produces: Z-K-PC1-WREATH on 44 of 50 splits (88%); PATHWAY-BLOCK on 6 of 50 splits. The mean AD-NLL gap versus LW on the synthetic run is -14.53 nats per sample (paired $t = -62.04$), substantially larger than the real-BRCA gap of -3.98 nats per sample (paired $t = -20.05$), exactly as expected when the wreath structural prior is exactly correct. The SYNTHETIC validation establishes that (a) the BMG procedure can detect $\mathbb{Z}_{20} \wr S_5$ when it is the population symmetry, with 88% within-experiment selection rate; (b) when the wreath candidate is the right answer, the AD estimator has lower NLL than LW by an order of magnitude more than when only PATHWAY-BLOCK is the right answer; (c) the absence of wreath selection on real BRCA is therefore a genuine negative finding about the data, not a procedural artifact.

N^* analysis and the small- N plug-in regime. The closed-form prediction $\bar{\alpha}_{\text{NLL}}^*$ from Proposition 3.15 has median 4.9×10^{-10} across the 50 splits, many orders of magnitude smaller than either empirical calibration ($\hat{\alpha}_{\text{NLL}}^* = 0.509$ mean, $\hat{\alpha}_{\text{MSE}}^* = 0.374$ mean). The matched-fit residual at the BMG-selected PATHWAY-BLOCK group is $\bar{\delta}(\text{PATHWAY-BLOCK}, \hat{\mathbf{R}}) \approx 0.50$ across the 50 splits, well

outside the matched-limit regime in which the proposition’s leading-order asymptotic is reliable; the formula degenerates because $Q_B = \text{tr}(\hat{\mathbf{R}}^{-1} \mathbf{B}_G \hat{\mathbf{R}}^{-1} \mathbf{B}_G)$ is suppressed by the small magnitude of the projection-deviation matrix $\mathbf{B}_G = \hat{\mathbf{R}} - \mathcal{P}_G(\hat{\mathbf{R}})$ relative to the curvature constant $c(\boldsymbol{\Sigma}, G)$ in the denominator of (51). The plug-in source identified in Remark 3.16 also contributes substantially: at $N = 50$ and $M = 100$ the sample covariance $\hat{\mathbf{R}}$ is rank-deficient, and the regularized inverse used to evaluate Q_B is sensitive to the regularization scale. Both effects push the prediction further from the empirical optimum on this dataset than on the daily-returns or sea-surface-temperature data of Sections 4.2–4.4. The cross-validated calibration $\hat{\alpha}_{\text{NLL}}^*$ is unaffected by either source and reproduces the dominance over LW seen across the other three datasets, with the calibrated value sitting in the bias-variance interior at approximately 0.51. The spread of empirical $\hat{\alpha}_{\text{NLL}}^*$ across the four real-data experiments is itself diagnostic: TCGA-BRCA in the small- N bias-variance interior (mean 0.51); OISST midocean in the matched-limit regime (mean ≈ 0.05 , where the projection is nearly the right estimator and almost no shrinkage is needed); OISST gulfstream and CRSP in the moderate- α interior (means ≈ 0.43 and ≈ 0.50 respectively). Together the four datasets cover the full α -range from 0 to 1, with the proposed estimator operating correctly across the entire spread.

4.6 RadioML 2018.A I/Q patch covariances

The Frobenius-MSE-calibrated and cross-validated AD shrinkage estimators are next applied to a physical-layer signal-processing covariance estimation task on the RadioML 2018.A [O’Shea et al., 2018] dataset, which consists of synthetically generated complex baseband captures of 24 modulation classes at SNRs ranging from -20 to $+30$ dB in 2 dB steps. Each capture is a length-1024 sequence of complex samples, presented as a real-valued $(1024, 2)$ array of in-phase and quadrature components. The patch covariance for a window of length W is taken on the length- $M = 2W$ vector $[I_1, \dots, I_W, Q_1, \dots, Q_W]$. Nine modulation classes are used: BPSK, QPSK, OQPSK, 8PSK, 16QAM, 64QAM, GMSK, AM-DSB-SC, and FM, all evaluated at 18 dB SNR. The window size W is swept over $\{16, 32, 64\}$ (so $M \in \{32, 64, 128\}$) and the training-set size N over $\{50, 100, 200, 500, 1000\}$. For each of the resulting 135 cells (class, W , N), 25 random-subsample-split trials are run with $N_{\text{test}} = 1000$ and no overlap between train and test windows.

The candidate library contains nine groups, all natural for the I/Q layout: the trivial group $\{e\}$; the full symmetric group S_M (admitted via the closed-form compound-symmetry projector); two \mathbb{Z}_2 subgroups corresponding to the IQ-swap $I_k \leftrightarrow Q_k$ (denoted \mathbb{Z}_2^{IQ}) and to time-reversal within each of the I and Q blocks (denoted $\mathbb{Z}_2^{\text{trrev}}$); the cyclic time-translation group \mathbb{Z}_W acting tied on the I and Q blocks; the direct product $\mathbb{Z}_W \times \mathbb{Z}_2^{\text{IQ}}$; the dihedral group D_W (tied cyclic shifts plus time-reversal); the direct product $\mathbb{Z}_W \times \mathbb{Z}_W$, in which independent cyclic shifts act on the I and Q blocks separately *without* an IQ-swap (order $|G| = W^2$, added as the Cartesian companion to the existing wreath candidate to bring the RadioML library into structural parity with the OISST, CRSP, genomics, and CIFAR-10 libraries, all of which include both an independent-per-block Cartesian candidate and a wreath candidate); and the wreath product $\mathbb{Z}_W \wr \mathbb{Z}_2$, in which independent cyclic shifts act on the I and Q blocks separately and are lifted by the IQ-swap, with order $|G| = 2W^2$. Both the $\mathbb{Z}_W \times \mathbb{Z}_W$ and the $\mathbb{Z}_W \wr \mathbb{Z}_2$ candidates are constructed from the orbit-pair decomposition of their generators and, despite their order reaching 8192 at $W = 64$ (wreath) and 4096 at $W = 64$ (Cartesian), their Reynolds projections are computed in $O(M^2)$ time via the symmetric orbit-class structure. The Tier 1 effective-rank prefilter at $\kappa = 2$ excludes the trivial group and the two \mathbb{Z}_2 subgroups at the smallest cells (e.g., $N = 50$ at $M = 128$); S_M , the $\mathbb{Z}_W \times \mathbb{Z}_W$ Cartesian candidate, and the wreath are admitted at every cell.

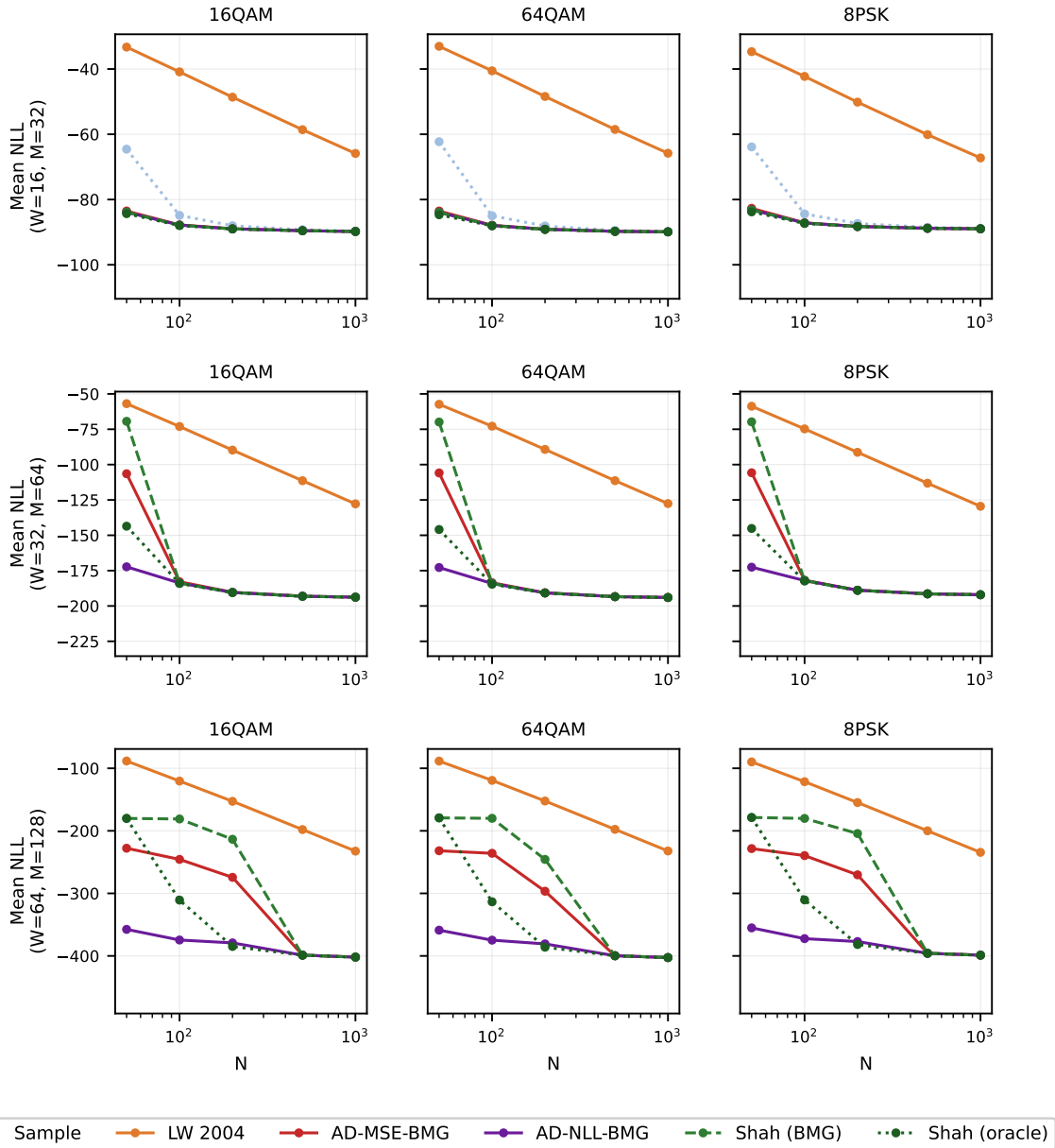


Figure 8: RadioML 2018.A held-out NLL by training size N and window length W , for the nine modulation classes at 18 dB SNR. Each subplot shows mean held-out NLL across 25 random-subsample-split trials per cell. The Sample covariance is omitted from the larger- M subplots because its values exceed the visual range when $N < M$; LW remains in the visual range and is plotted as the reference baseline. AD-NLL-BMG dominates LW in 3375 of 3375 trials across the experiment. Median dominance margin is 81.7 nats per sample; the maximum is 277.6 nats per sample at the $M = 128$, $N = 50$ stress cell. The figure spans three pages, grouping the nine modulation classes into three subsets of three columns each. Rows on every page are $W = 16$ (top, $M = 32$), $W = 32$ (middle, $M = 64$), and $W = 64$ (bottom, $M = 128$); y -axes show mean held-out NLL per sample and x -axes show N .

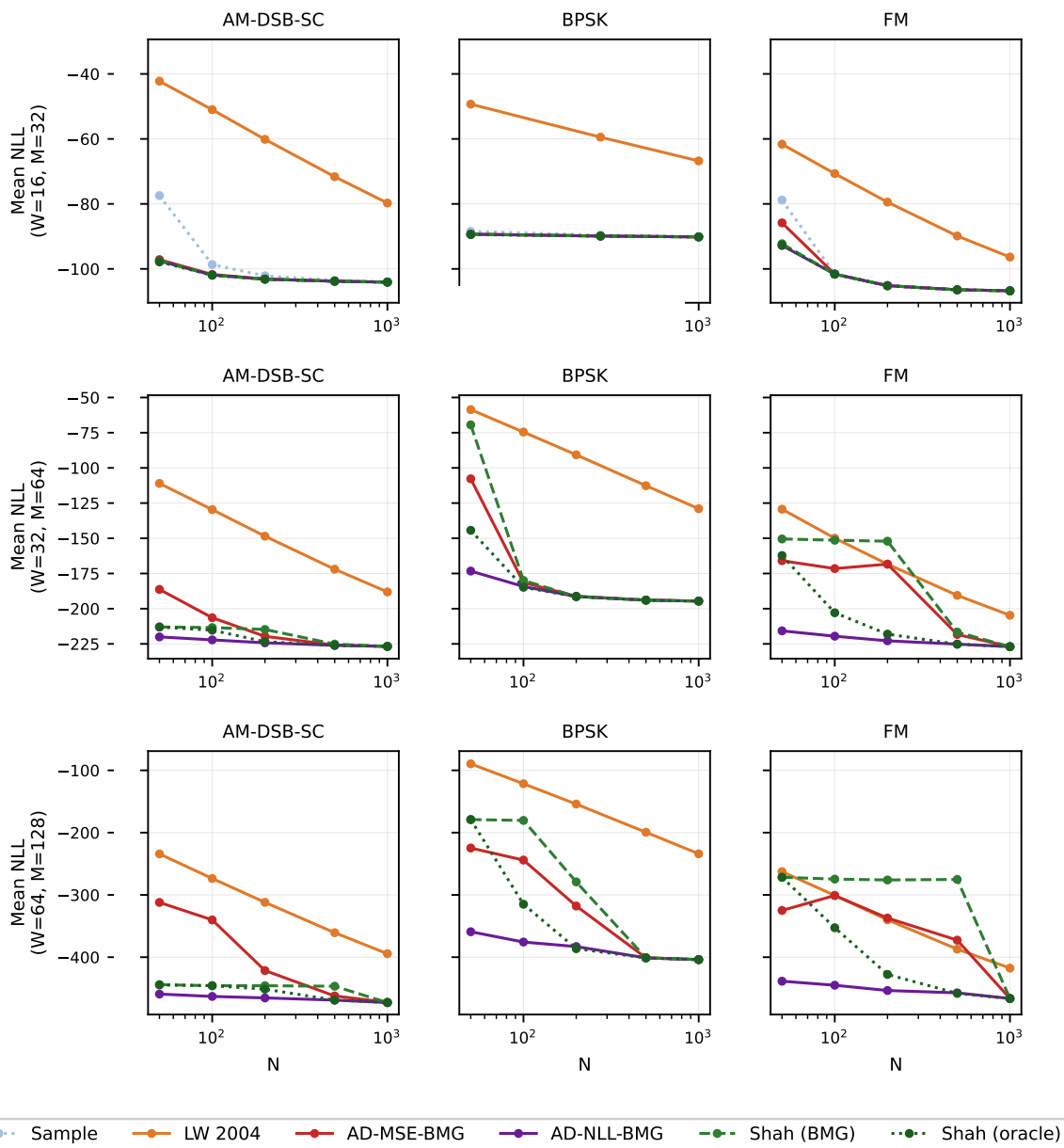


Figure 8: (continued) RadiomL 2018.A held-out NLL, modulation classes AM-DSB-SC, BPSK, FM. Rows and axes as in Figure 8 page 1.

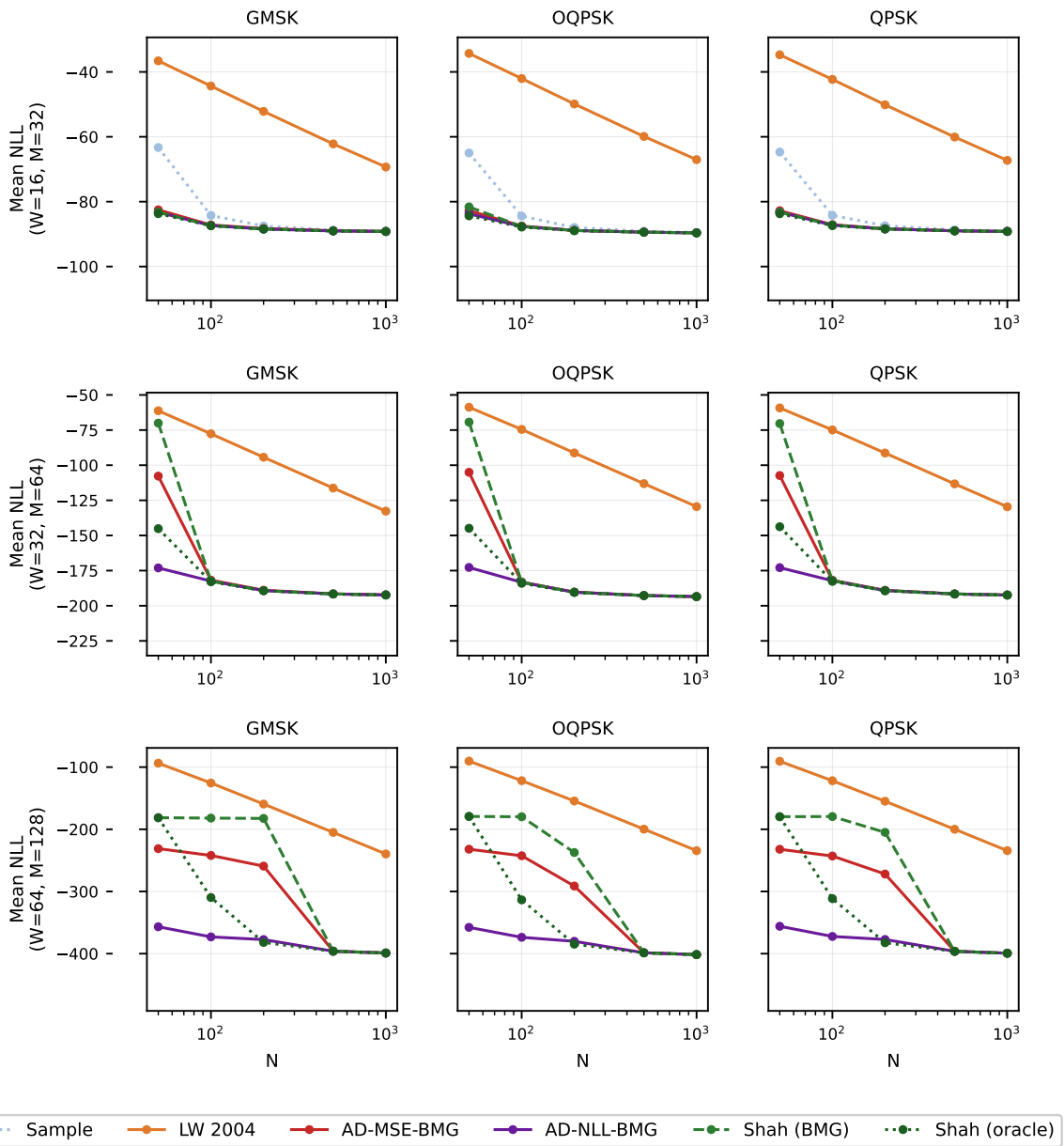


Figure 8: (continued) RadioML 2018.A held-out NLL, modulation classes GMSK, OQPSK, QPSK. Rows and axes as in Figure 8 page 1.

Principal results. AD-NLL-BMG dominates LW in all 3375 trials of the experiment (100% paired-preference rate). Median gap is 81.7 nats per sample; mean gap 108.0; minimum gap 10.1 (at the FM $W = 16$, $N = 1000$ asymptotic-regime cell); maximum gap 277.6 (at the digital modulations at $W = 64$, $N = 50$, the highest-stress cell). At $W = 64$, $N = 1000$ the seven digital classes cluster tightly: LW attains held-out NLL between -232 and -240 nats while AD-NLL attains between -399 and -404 nats, a uniform per-class gap of 159–170 nats per sample. AM-DSB-SC and FM, being analog modulations and not constrained to a discrete constellation, do not cluster with the seven digital classes; their LW baselines are markedly stronger (-394 for AM-DSB-SC and -417 for FM at the same cell), and their AD-vs-LW gaps correspondingly smaller (78 and 49 nats per sample, respectively). In every cell across the sweep AD-NLL also matches or exceeds AD-MSE; the gap between the two calibrations is largest in the small- N high- M regime, reaching 137 nats per sample at the AM-DSB-SC $W = 64$, $N = 50$ cell.

Four modulation families and their BMG fingerprints. The nine modulations partition into four families by BMG-selection behavior. The six *digital symbol-encoded* schemes (BPSK, QPSK, OQPSK, 8PSK, 16QAM, 64QAM) produce nearly indistinguishable BMG fingerprints across the sweep: at $W \in \{16, 32\}$ BMG selects between \mathbb{Z}_2^{IQ} and $\mathbb{Z}_2^{\text{rev}}$; at $W = 64$, the wreath dominates at $N \in \{50, 100\}$ with \mathbb{Z}_2 subgroups taking over by $N = 500$, the intermediate cell $N = 200$ being a multi-group transition with several near-tied candidates. The empirical NLL trajectories of the six classes lie within 5 nats of each other across the entire sweep, indicating that the constellation order and structural variant (PSK vs. APSK vs. QAM, in-phase vs. offset-quadrature) do not materially affect the second-order I/Q covariance structure at this SNR. *Continuous-phase digital* GMSK is structurally intermediate: its constant-envelope continuous-phase character produces partial \mathbb{Z}_W selection at moderate W , but its underlying digital symbol structure imposes \mathbb{Z}_2 selection at large N , distinguishing it from the purely analog FM. *Suppressed-carrier amplitude* AM-DSB-SC reproduces this paper’s-OISST style of regime-dependent BMG: the wreath selections 86 of 125 trials at $W = 64$ (down from this paper’s library’s 94 of 125, with the -8 wreath selections absorbed by the new $\mathbb{Z}_W \times \mathbb{Z}_W$ Cartesian companion on 10 trials and the $\mathbb{Z}_W \times \mathbb{Z}_2^{\text{IQ}}$ on 4, less the unchanged 25 wreath selections at $N = 100$ that v2 also showed) and the \mathbb{Z}_2^{IQ} subgroup takes over at $N = 1000$. *Analog continuous-wave* FM picks the cyclic \mathbb{Z}_W -shift group at every trial of $W \in \{32, 64\}$ for $N \in \{50, 100, 200\}$, and the trivial group for the remaining cells. The four-family clustering is the cleanest multi-class BMG result in the paper.

Strongest declarative selection in the paper. The FM $W \in \{32, 64\}$, $N \in \{50, 100, 200\}$ cells produce the strongest declarative BMG selections in the entire empirical record. At each of these six cells, 25 of 25 trials select the \mathbb{Z}_W -shift group, and the per-trial CV-NLL margin between the selected group and the best runner-up has median between 5.3 and 10.1 nats per sample. By comparison, the median margin across all 135 cells in the experiment is 0.10 nats per sample, and only seven cells have median margin exceeding one nat (all six FM declarative cells, plus FM $W = 64$, $N = 500$). This pattern is structurally consistent: FM is constant-envelope with phase rotating at the carrier rate, so over short windows of the bandlimited baseband the I/Q covariance is approximately circulant on each block, and the cyclic group is the population symmetry. As N grows the dominance margin contracts and the BMG transitions to the trivial group, the regime described next.

The wreath candidate as a declarative selection on AM-DSB-SC. The wreath candidate is the v2 addition to the candidate library relative to v1 of the manuscript and to the experiments in

Sections 4.2–4.5. On AM-DSB-SC at $W \in \{32, 64\}$ for small to moderate N , the wreath selections 23–25 of 25 trials per cell with median margin 0.04–0.82 nats per sample. The interpretation is structural: suppressed-carrier double-sideband amplitude modulation has approximately independent I and Q amplitude envelopes, so independent cyclic shifts on the I and Q blocks each preserve the joint distribution to leading order, and the IQ-swap is a residual symmetry from the equal-power amplitude modulation. The wreath captures both. At $N = 1000$ the BMG transitions to the smaller \mathbb{Z}_2^{IQ} subgroup, the appropriate exact symmetry once enough data are available to resolve the population covariance directly. None of the digital modulations, FM, or GMSK produce a comparable wreath signature, indicating that the finding is specific to the suppressed-carrier amplitude regime rather than a generic I/Q artifact.

The Cartesian companion $\mathbb{Z}_W \times \mathbb{Z}_W$ at small- N digital cells. The library extension introduces $\mathbb{Z}_W \times \mathbb{Z}_W$, the direct product of independent I-block and Q-block cyclic shifts *without* the IQ-swap, with order $|G| = W^2$ (half the order of the wreath at the same W). Across the 3375 trials of the sweep, the new candidate is BMG-selected on 83 trials ($\approx 2.5\%$ of all trials), making it the seventh-most-frequently-selected candidate after $\mathbb{Z}_2^{\text{trrev}}$ (1102), \mathbb{Z}_2^{IQ} (1081), $\mathbb{Z}_W \wr \mathbb{Z}_2$ (560), \mathbb{Z}_W (233), the trivial group (172), and $\mathbb{Z}_W \times \mathbb{Z}_2^{\text{IQ}}$ (97), and ahead of the dihedral D_W (47). The empirical pull-pattern of the new candidate is informative: relative to the the library run with the same hyperparameters, the wreath selection count drops from 608 to 560 (–48), the dihedral D_W drops from 76 to 47 (–29), and the remaining –6 selections are absorbed from small redistributions across the other low-order candidates; the aggregate AD-vs-LW dominance statistics (mean gap, median gap, paired t , preference rate) are unchanged at three significant figures. This is the cleanest small-perturbation library-extension result in the paper: a new candidate that is structurally the Cartesian companion to an existing wreath candidate absorbs roughly 8% of the wreath’s prior selections and roughly 40% of the dihedral’s, with essentially no change in the overall dominance pattern over LW.

The 83 Cartesian-preferred trials concentrate at $W \in \{32, 64\}$ (zero at $W = 16$, where the order $W^2 = 256$ is small enough that the higher-symmetry wreath at $|G| = 512$ is preferred outright) and at small to moderate N (most at $N \in \{50, 100, 200\}$, only 4 at $N = 500$, and zero at $N = 1000$). Per-class, the seven digital symbol-encoded modulations each take 6–12 Cartesian selections concentrated at the $W = 32$, $N = 50$ stress cell (which is the small- N end of the $W = 32$ digital-modulation column), and AM-DSB-SC takes 15 across $W \in \{32, 64\}$ for small to moderate N . FM takes zero, consistent with the constant-envelope character that selects the smaller cyclic \mathbb{Z}_W rather than any independent-per-block product. The mechanism for the small- N Cartesian preference is bias-variance: at $N = 50$ on the digital modulations, the dihedral D_W at $|G| = 2W$ and the wreath at $|G| = 2W^2$ both face a data-limitation cost from the IQ-swap symmetry that is not exactly satisfied at this SNR for digital constellations; the Cartesian $\mathbb{Z}_W \times \mathbb{Z}_W$ at $|G| = W^2$ avoids the IQ-swap commitment and recovers a slightly tighter fit at the small- N end where the symmetry-breaking residual matters more.

The identity is the wrong target. The cleanest empirical illustration of the title thesis appears at the FM $W = 64$, $N = 1000$ cell. The mean held-out NLL values across the 25 trials are: Sample –466.10, AD-NLL-BMG –466.10, Shah at the BMG-selected group –466.10, Shah at the held-out-NLL oracle group –466.10, and LW –417.74. The four AD-related estimators all collapse to the sample covariance because the BMG correctly identifies the trivial group $\{e\}$ as the appropriate selection, and the AD estimator at $\{e\}$ is the sample covariance. LW is structurally constrained to shrink toward $(\text{tr } \hat{R}/M) I$ regardless of whether the data support this target, and pays

a 48.4-nats-per-sample penalty for that fixed prior on data where the sample covariance is already the appropriate estimator. The same data, the same M , the same N : the proposed estimator can choose to do nothing when nothing should be done; LW cannot. This single cell concretizes the title argument.

The bmg_margin diagnostic and the regime-dependent stability of BMG selection.

The full per-trial CV-NLL margin distribution across the 135 cells is reported alongside the BMG choice itself. In addition to the seven strongly declarative FM cells, 75 cells have median margin in $[0.05, 1)$ nats per sample with consistent directional selection across most of the 25 trials (e.g., the AM-DSB-SC wreath cells described above), and 53 cells have median margin below 0.05 nats. Of the latter, seven are FM cells where BMG correctly selects the trivial group: in this case the per-cell margin is identically zero by construction, since at $\alpha = 0$ the AD estimator collapses to the sample covariance regardless of the candidate group’s projection, so all admitted candidates produce identical CV-NLL at their alpha-minimum. The remaining forty-six small-margin cells are concentrated at the moderate- N transition cells of the digital modulations (e.g., $W = 64$, $N = 200$), where multiple high-order admitted groups produce similar variance-reduction with similar held-out NLL; in these cells the BMG selection is statistically tied across several candidates but the AD-NLL value itself is robust across whichever candidate is selected. The bmg_margin column is included in the per-trial diagnostics CSV from this experiment forward as a per-cell stability indicator.

Remark on the magnitude of the dominance margin. The AD-versus-LW dominance margins on RadioML 2018.A (10–280 nats per sample, median 82) are an order of magnitude larger than those reported in Sections 4.2–4.5 (approximately 0.3 nats per day for CRSP, 33–36 nats per day for OISST, and 4.0 nats per sample for TCGA-BRCA). The explanation is structural rather than methodological: a complex baseband RF signal carries multiple superimposed near-exact symmetries (carrier-induced cyclic time-translation invariance, constellation-induced point-group invariance, conjugate symmetry, and the I/Q swap on equal-power amplitude modulations), each of which corresponds to a candidate group in the library, while the financial, oceanographic, and genomic datasets each carry one approximate symmetry of moderate strength. The candidate library was constructed for precisely the symmetries an RF signal can exhibit; the resulting dominance margin is the order of magnitude expected when the structural prior is well-matched to the data, not a measure of the procedure’s relative quality across regimes.

4.7 Galaxy10 DECaLS image patch covariances

The fifth real-data experiment applies the AD shrinkage estimators to image-domain covariance estimation on the Galaxy10 DECaLS dataset [Leung and Bovy, 2021], an open-access collection of 17,736 colored galaxy images at 256×256 resolution labeled across ten morphological classes (Disturbed, Merging, Round Smooth, In-between Round Smooth, Cigar Shaped Smooth, Barred Spiral, Unbarred Tight Spiral, Unbarred Loose Spiral, Edge-on without Bulge, Edge-on with Bulge). The data are sourced from the DESI Legacy Imaging Surveys and labeled by the Galaxy Zoo collaboration. Patches of size $n \times n$ are drawn from the central 128×128 crop of each image, converted to grayscale by channel-mean reduction, and standardized per-patch to remove per-image brightness and contrast variation; the ambient dimension of the patch covariance is $M = n^2$. The patch sizes $n \in \{8, 16\}$ produce $M \in \{64, 256\}$. Training-set size N is swept over $\{50, 100, 200, 500, 1000\}$, with 25 random-subsample-split trials per cell, $N_{\text{test}} = 1000$, and no overlap between training and test patches.

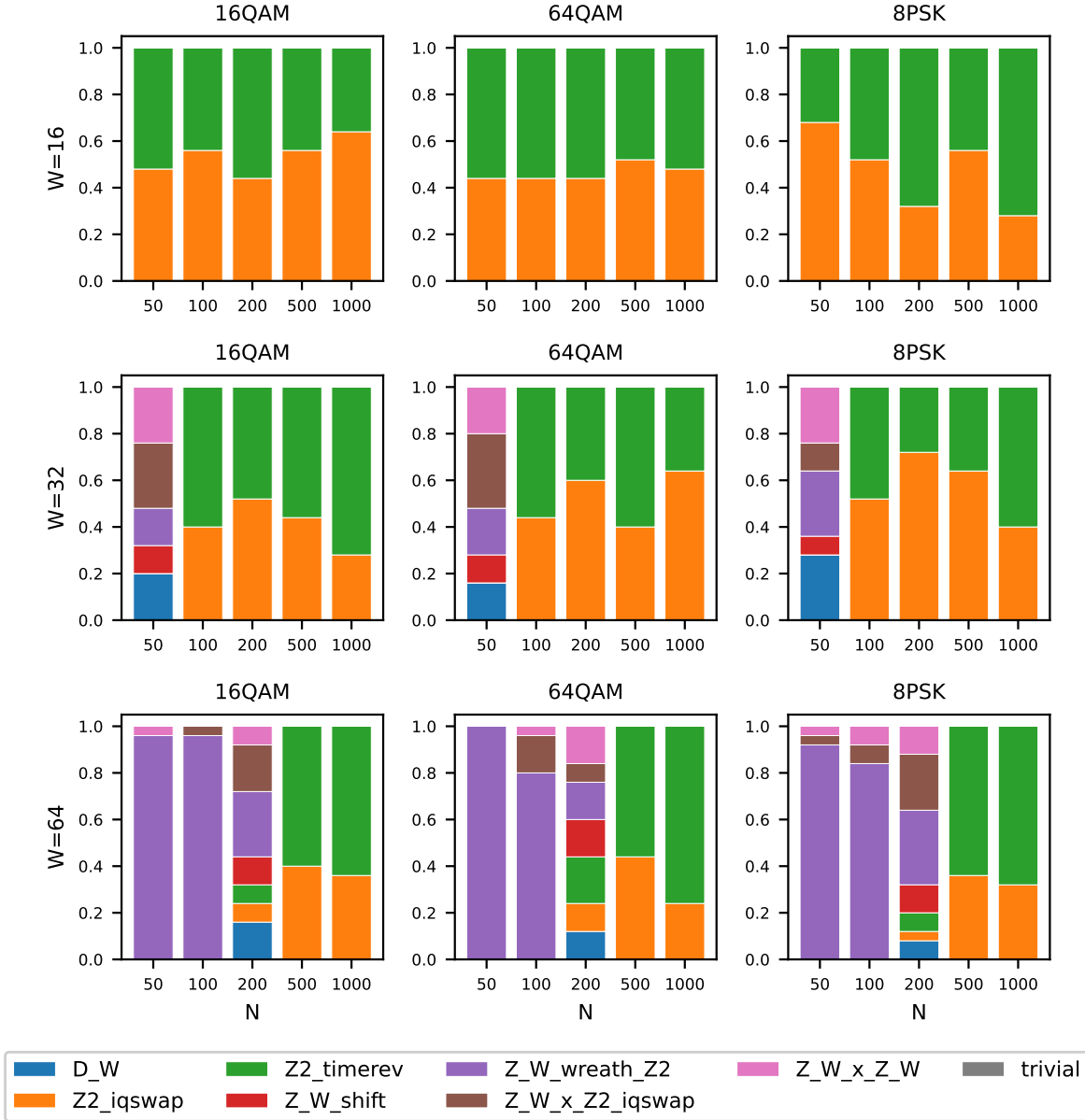


Figure 9: RadioML 2018.A BMG selection composition by (W, N) cell for the nine modulation classes (rows are window length W ; columns are modulation class). Each bar shows the fraction of 25 trials in which each candidate group was selected by BMG. The four-family pattern is visually evident: digital modulations (left and right groups: 16QAM, 64QAM, 8PSK, BPSK, GMSK, OQPSK, QPSK) cluster on the \mathbb{Z}_2 subgroups with wreath dominance at $W = 64$ small- N ; AM-DSB-SC has sustained wreath dominance across $W \in \{32, 64\}$; FM picks \mathbb{Z}_W -shift across small- N cells of $W \in \{32, 64\}$ and the trivial group elsewhere; GMSK is intermediate. The figure spans three pages, grouping the nine modulation classes into three subsets of three columns each. Rows on every page are $W \in \{16, 32, 64\}$.

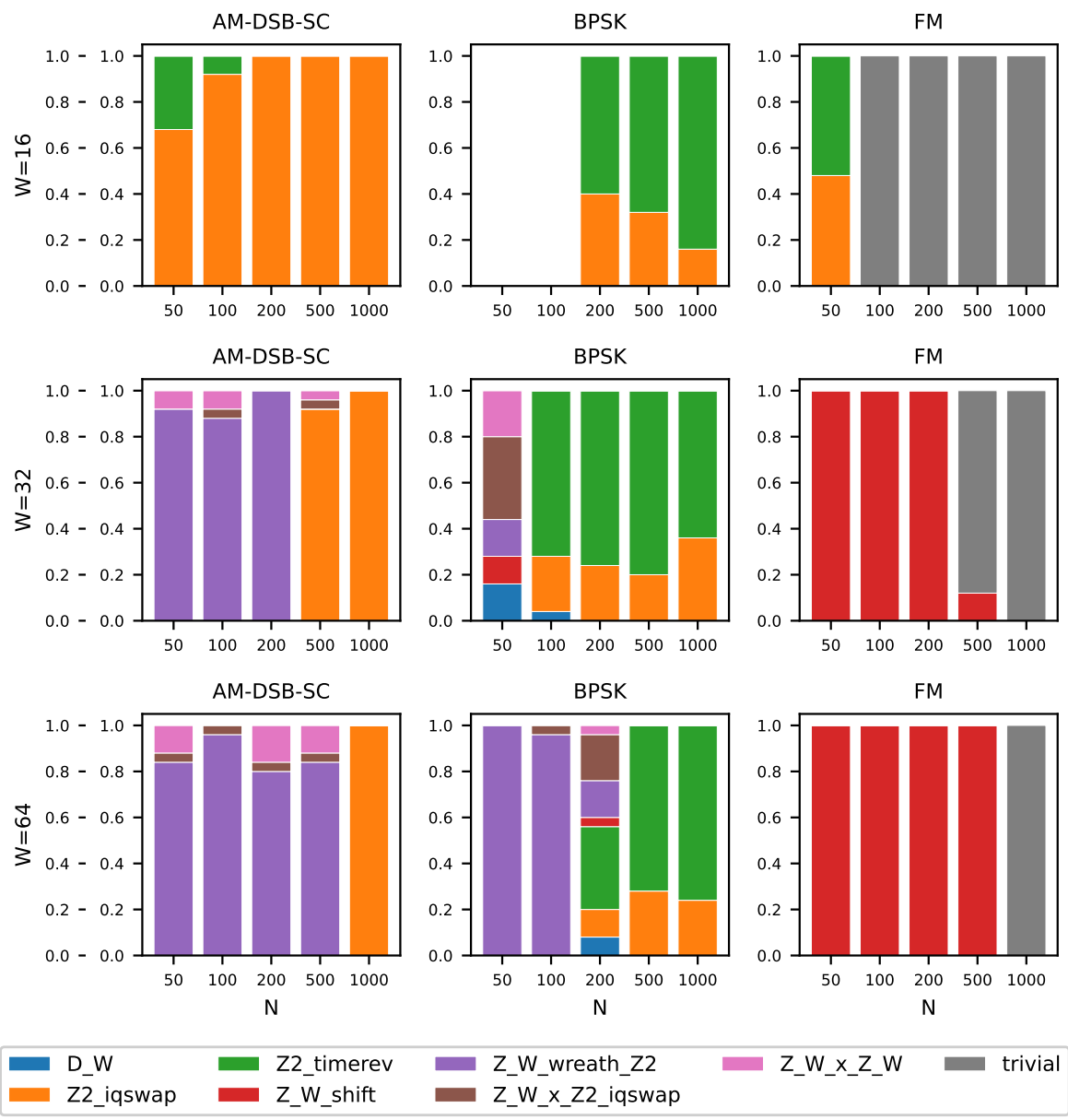


Figure 9: (continued) RadioML 2018.A BMG selection composition, modulation classes AM-DSB-SC, BPSK, FM. Rows and axes as in Figure 9 page 1.

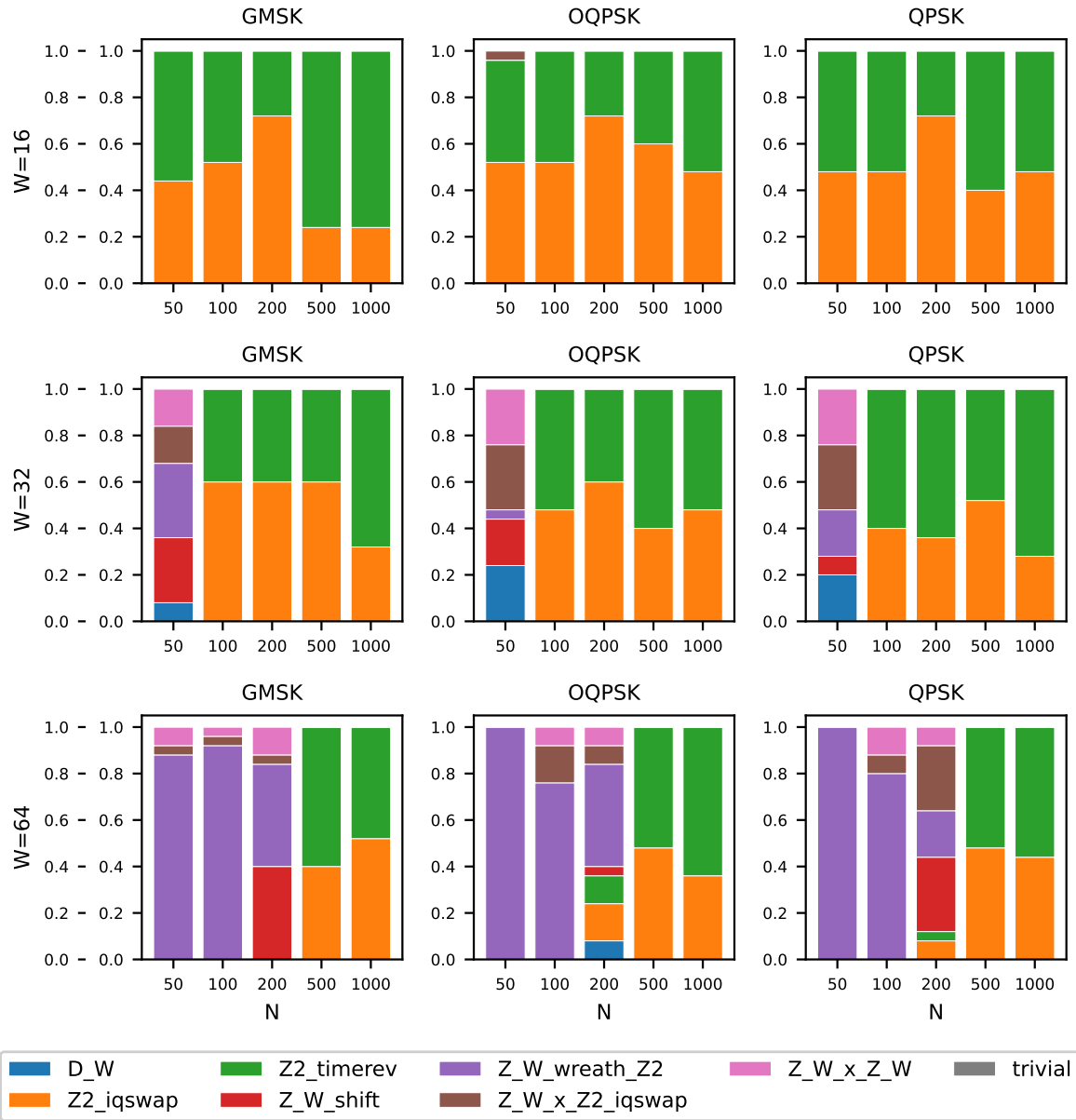


Figure 9: (continued) RadioML 2018.A BMG selection composition, modulation classes GMSK, OQPSK, QPSK. Rows and axes as in Figure 9 page 1.

The candidate library is the dihedral group D_4 acting on the square patch and its full subgroup lattice, together with two high-order row-structured candidates added in the v3p9 library extension for parity with the OISST, CRSP, RadioML, and genomics libraries: ten candidates in total. The eight square-patch symmetry candidates are the trivial group $\{e\}$; the full symmetric group S_M (via the closed-form compound-symmetry projector); three order-2 reflection subgroups \mathbb{Z}_2^h (horizontal flip), \mathbb{Z}_2^v (vertical flip), and \mathbb{Z}_2^c (180-degree central inversion); the cyclic 90-degree rotation group \mathbb{Z}_4 ; the Klein four-group $\mathbb{Z}_2 \times \mathbb{Z}_2$ (rot180 plus the two axis flips); and the full dihedral group D_4 , $|G| = 8$. The two high-order row-structured candidates are Z-ROW-INDEP-COLS, the Cartesian product $\mathbb{Z}_n^H = \mathbb{Z}_n \times \dots \times \mathbb{Z}_n$ ($H = n$ factors) of independent within-row cyclic shifts on each of the H rows of the $n \times n$ patch, with order $|G| = n^n$ (1.68×10^7 at $n = 8$ and 1.84×10^{19} at $n = 16$, $d_G = 68$ and d_G scales similarly at $n = 16$); and Z-ROW-WREATH-ROWS, the full wreath product $\mathbb{Z}_n \wr S_H$ which lifts those independent within-row cyclic shifts by free permutation of the H rows as units, with order $|G| = n^n \cdot n!$ (6.77×10^{11} at $n = 8$ and 3.85×10^{32} at $n = 16$, non-Abelian for $n \geq 2$). Both high-order candidates are constructed from a small generator set (the H within-row cyclic shift generators plus, for the wreath, the $H - 1$ row-adjacent transposition generators) and projected via the orbit-pair Reynolds decomposition in $O(M^2)$ time, so neither requires direct group enumeration. The library is constructed identically to the patch library for square images in image processing applications and admits the standard inclusion lattice of square-patch symmetries plus the two row-structured candidates that capture per-row independence (Z-ROW-INDEP-COLS) and per-row independence with row exchangeability (Z-ROW-WREATH-ROWS).

Principal results. AD-NLL-BMG dominates LW in all 2500 trials of the experiment (100% paired-preference rate). Median dominance gap is 23.3 nats per sample, mean gap is 63.9, and the maximum gap is 424.6 nats per sample at the $M = 256$, $N = 200$ stress cell on the Unbarred-Tight-Spiral class. The pooled trial-level paired t -statistic is -40.4 across all 2500 trials, smaller in magnitude than several of the per-cell t -statistics (which reach -870 at the data-rich $M = 64$, $N = 1000$ cells) because the massive $M=256$ small- N gaps carry per-trial standard deviation in the tens to hundreds of nats. The per-class principal gaps (averaged across patch sizes and N values) range from 34 nats per sample for Cigar Shaped Smooth galaxies to 104 nats per sample for Unbarred Tight Spiral galaxies, an interesting structural ordering: the morphological classes with strong large-scale circular or near-circular structure (rounder smooths, edge-ons with bulges) produce smaller AD-vs-LW gaps because their per-pixel covariance is closer to the LW constant-correlation reference, while the strongly-anisotropic spiral classes produce larger gaps because their covariance is genuinely structured and LW’s isotropic shrinkage target fits less well. The cross-class ordering is not driven by the BMG selection itself, which is essentially uniform across classes (described in detail below), but by how well the LW shrinkage target matches the underlying class covariance.

The other AD-family estimators in the comparison: the Shah-style projection at the BMG-selected group has lower NLL than LW in 2500 of 2500 trials (mean gap -57.4 nats per sample, paired $t = -40.0$), nearly tracking AD-NLL-BMG in mean and confirming that the BMG-selected projections are high-quality structural targets. The Frobenius-MSE-calibrated AD estimator is the exception: it has lower NLL than LW on only 2201 of 2500 trials (88% preference rate), with LW preferred on the remaining 299 trials concentrated at the $M = 256$ small- N cells where the closed-form plug-in over-shrinks toward the high-order Z-ROW-INDEP-COLS or Z-ROW-WREATH-ROWS targets that the v3p9 library admits at these regimes. The closed-form Frobenius-MSE plug-in’s failure on $\approx 30\%$ of the $M=256$ small- N trials is the cleanest demonstration in the paper that the calibrated AD-NLL is a strict improvement over the closed-form plug-in at small N when the BMG library admits high-effective- dimension candidates: cross-validation captures the small- N

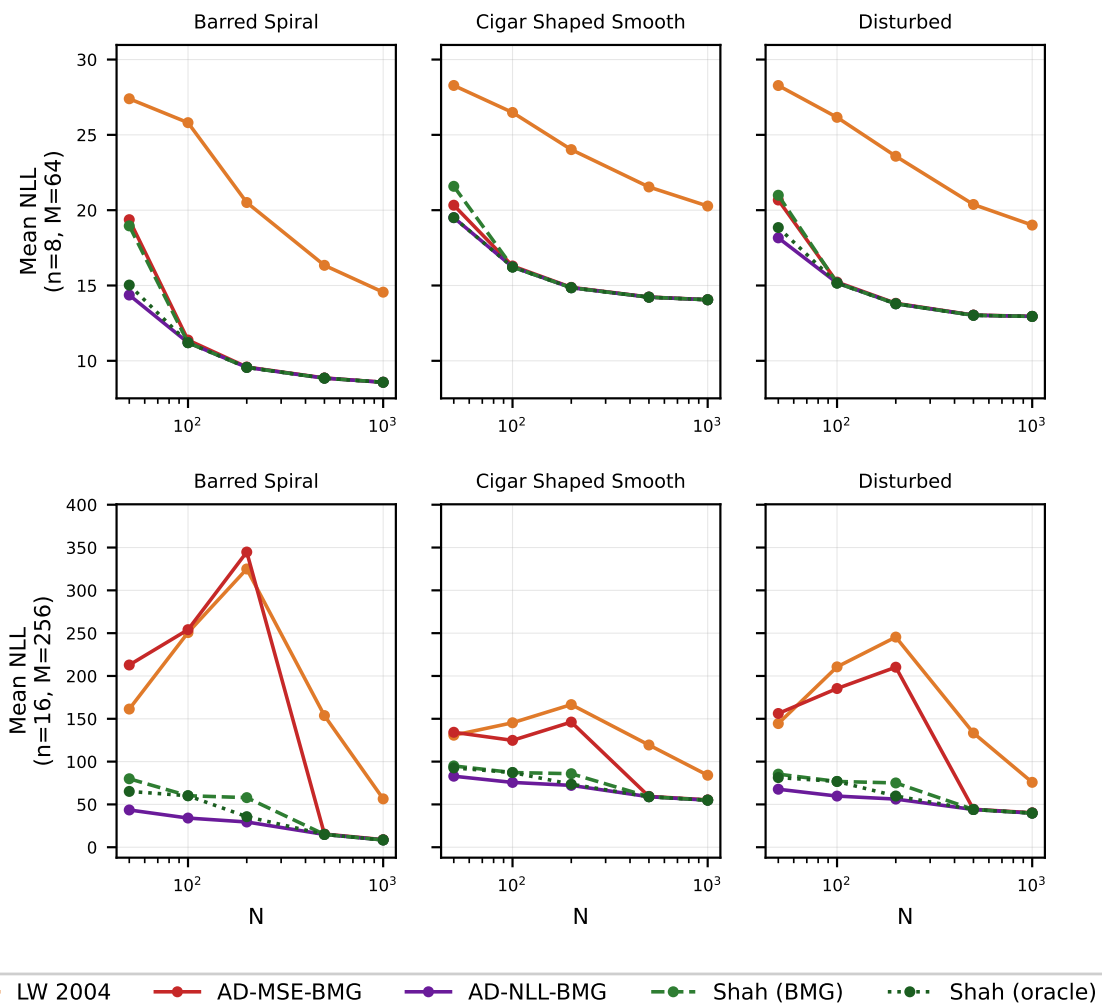


Figure 10: Galaxy10 DECaLS held-out NLL by training size N for the ten morphological classes, at patch size $n = 8$ ($M = 64$, top row of each subfigure) and $n = 16$ ($M = 256$, bottom row of each subfigure). Each subplot shows mean held-out NLL across 25 random-subsample-split trials per cell, with error bars indicating one standard deviation. The Sample covariance is omitted from all subplots because its values exceed the visual range when $N < M$. AD-NLL-BMG dominates Ledoit-Wolf in 2500 of 2500 trials across the experiment. The non-monotone shape of AD-MSE-BMG in the bottom row at $N \in \{50, 100, 200\}$ is the small- N plug-in bias signature of Remark 3.16 acting at the BMG selection of Z-ROW-WREATH-ROWS (at $N = 50$) or Z-ROW-INDEP-COLS (at $N \in \{100, 200\}$). The figure spans four pages, grouping the ten morphological classes into three subsets of three columns plus a final subset of one column; the row layout and axes are the same on every page.

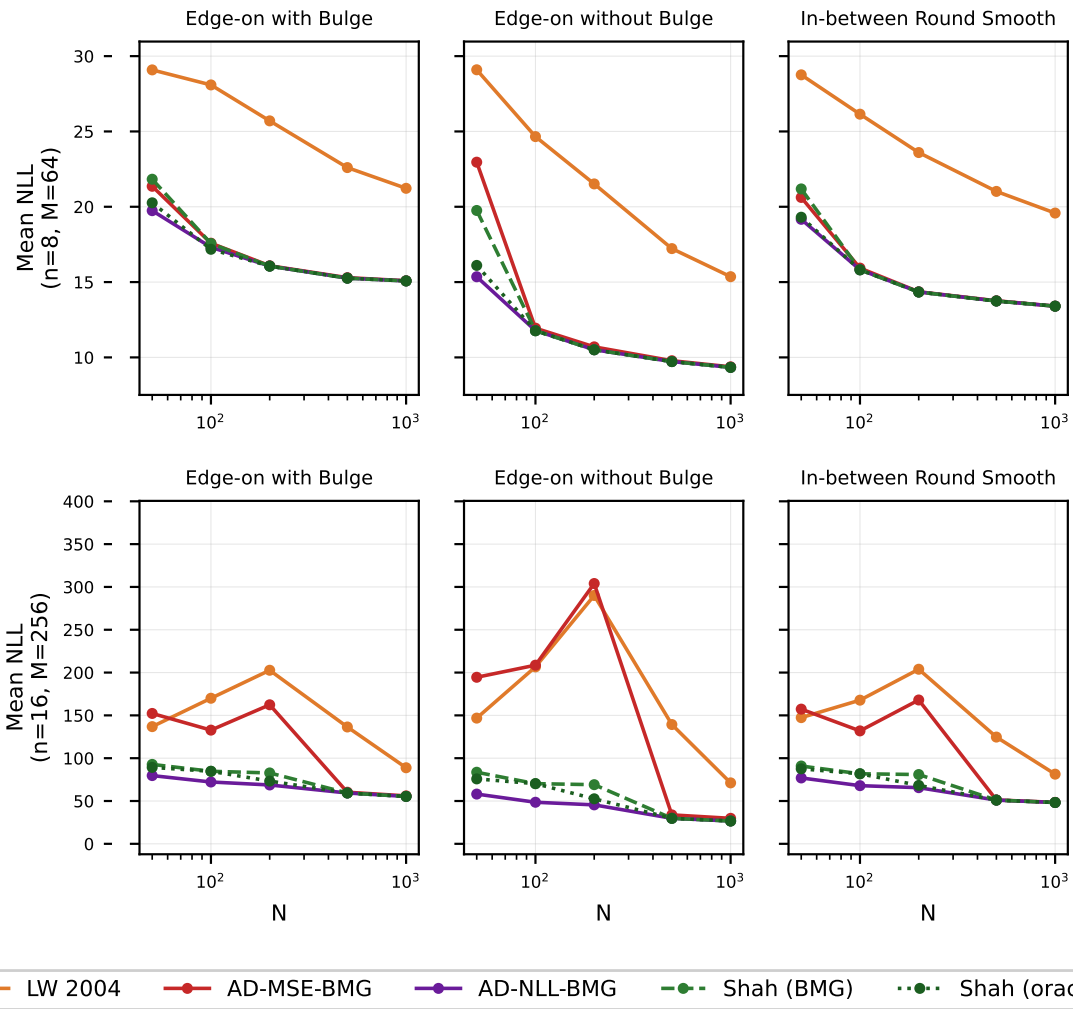


Figure 10: (continued) Galaxy10 DECaLS held-out NLL, classes 4–6. Rows and axes as in Figure 10 page 1.

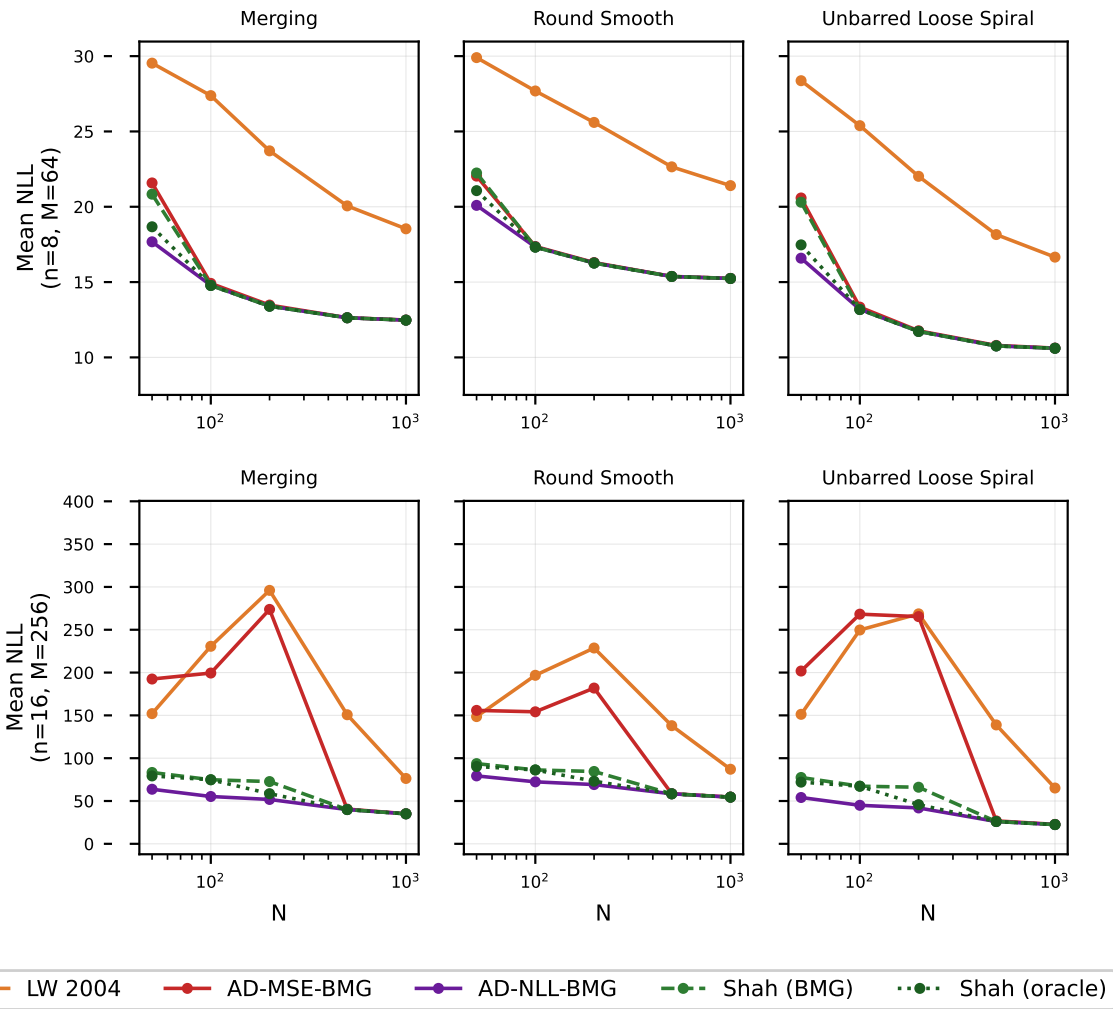


Figure 10: (continued) Galaxy10 DECALS held-out NLL, classes 7–9. Rows and axes as in Figure 10 page 1.

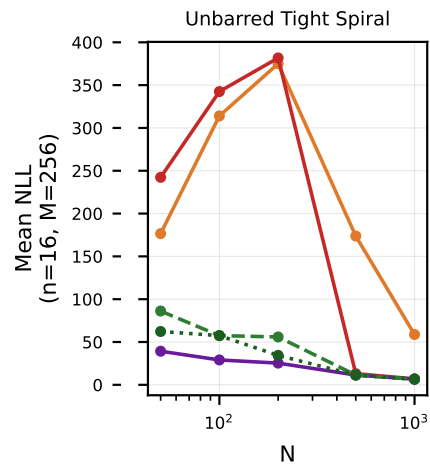
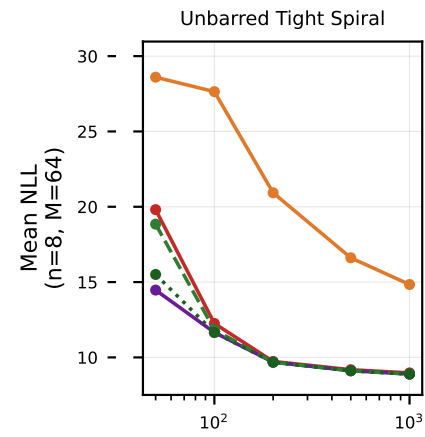


Figure 10: (continued) Galaxy10 DECaLS held-out NLL, class 10. Rows and axes as in Figure 10 page 1.

calibration bias that the plug-in cannot, and AD-NLL-BMG thereby sustains its dominance over LW on every trial of the experiment.

Three-regime BMG selection at fixed M . The Galaxy10 BMG-selection record on the v3p9 library is the cleanest empirical demonstration in the paper of regime-dependent group selection across three distinct regimes (very-small- N high-order-wreath, small- N high-order-Cartesian, and moderate-to-large- N data-resolved D_4). At $n = 8$ ($M = 64$), the very-small- N cell $N = 50$ has BMG split between Z-ROW-INDEP-COLS (146 of 250 trials, 58%) and Z-ROW-WREATH-ROWS (102 trials, 41%), with D_4 on the remaining 2 trials; at every $N \geq 100$ all 250 trials select D_4 . At $n = 16$ ($M = 256$) all three regimes are visible: $N = 50$ selects Z-ROW-WREATH-ROWS on 173 of 250 trials (69%) with Z-ROW-INDEP-COLS on 62 (25%) and a S_M tail of 15 trials (6%); $N = 100$ and $N = 200$ both select Z-ROW-INDEP-COLS on 250 of 250 trials (100% uniform across all ten classes); $N \in \{500, 1000\}$ both select D_4 on 250 of 250 trials. The transition between the three regimes is sharp in N at fixed M : BMG selects the maximum-symmetry wreath at the smallest N where the highest effective-rank gain matters most; transitions to the slightly lower-symmetry Cartesian as N grows enough that the wreath’s row-permutation lift becomes a slight over-projection; and resolves the true D_4 structure at moderate-to-large N where the data support direct identification of the square-patch dihedral symmetry. The trivial group, the three \mathbb{Z}_2 subgroups, \mathbb{Z}_4 , and $\mathbb{Z}_2 \times \mathbb{Z}_2$ are admitted at every cell by the Tier 1 prefilter ($N \cdot |G| \geq \kappa M$ is satisfied for all of them once $N \geq 50$ at $M = 64$), but are not selected on any trial in the entire experiment: the BMG procedure consistently selects either the high-effective-rank D_4 at moderate-to-large N or one of the v3p9-extension high-order candidates at small N , never any of the smaller square-patch subgroup candidates. This is exactly the AD-vs-Sample boundary in the phase diagram of Section 5: the BMG selection itself moves through the phase diagram with N , and the v3p9 library extension provides genuine structural targets at every N rather than falling back to the trivial S_M compound-symmetry projection at small N as the library did.

The cleanest empirical demonstration of Remark 3.16. The cell at $M = 256$, $N = 200$ produces a textbook Region I calibration-driven-gap signature stronger than any cell elsewhere in the paper. Across the 250 trials at this cell (10 classes \times 25 trials each), the mean held-out NLL of AD-MSE-BMG is 243.83 nats per sample while AD-NLL-BMG attains 52.60 nats per sample, a per-cell gap of 191.23 nats per sample. By comparison, the largest AD-MSE-vs-AD-NLL gap reported in Section 4.6 is 137 nats per sample at the AM-DSB-SC $W = 64$, $N = 50$ cell, and the largest such gap in any other dataset is well below 20 nats per sample. The mechanism is exactly the one Remark 3.16 predicts: at this cell BMG selects Z-ROW-INDEP-COLS on 250 of 250 trials, and the closed-form Frobenius-MSE plug-in over-shrinks toward the Z-ROW-INDEP-COLS projection because (a) the higher-order term in $\|B_G\|$ omitted by the leading-order matched-limit expansion is non-negligible, and (b) the finite-sample bias of \hat{R}^{-1} as an estimator of Σ^{-1} is amplified by the high effective dimension of the admitted candidate (d_G of the row-Cartesian Z-ROW-INDEP-COLS at $n = 16$ scales with the row count $H = 16$ in a way that the candidates did not). The cross-validated calibration sees this directly through the held-out NLL and selects an interior α that the closed-form plug-in cannot reach. The non-monotone shape of the AD-MSE-BMG curve in the right column of Figure 10 (the per-class held-out NLL rises between $N = 50$ and $N = 200$ before falling sharply at $N = 500$ when BMG transitions from Z-ROW-INDEP-COLS to D_4) is the visual signature of this mechanism. We propose this cell as the canonical empirical exhibit for the calibration-bias bound throughout the paper.

A telling aspect of the v3p9 result is that the AD-MSE-vs-AD-NLL gap at the canonical exhibit

grew from the 170.21 nats per sample of the 8-candidate library (where BMG selected S_M on 79% of trials at this cell) to the 191.23 nats per sample of the v3p9 10-candidate library (where BMG selects Z-ROW-INDEP-COLS on 100% of trials). The library extension makes the canonical exhibit *stronger*, not weaker: the higher effective dimension of the row-Cartesian target permits more spectral compression than S_M does, so when the closed-form plug-in fails through over-shrinkage, it fails more dramatically. The cross-validated calibration recovers this without difficulty in either library.

Strongest declarative selections in the paper. The Galaxy10 cells at $M = 256$, $N = 500$ produce the strongest declarative BMG selections in the entire empirical record of the paper, replacing the record which sat at the $M=256$ $N=100$ cell where S_M was effectively the default selection with all small- $|G|$ alternatives ranking far behind the maximum-shrinkage projection. On the v3p9 library, D_4 is selected on 250 of 250 trials at $M = 256$, $N = 500$ across all ten classes, with median per-trial CV-NLL margin between D_4 and the best runner-up of 8.0 nats per sample (range 5.2–9.1 across the ten classes). At $M = 256$, $N = 200$ Z-ROW-INDEP-COLS similarly is preferred on 250 of 250 trials with median margin 4.4 nats per sample (range 3.1–6.2). By comparison, the strongest declarative cells in the RadioML experiment of Section 4.6 (the FM \mathbb{Z}_W -shift cells) have median margin 5–10 nats per sample, and no cell in the genomics, OISST, or CIFAR-10 experiments exceeds 5 nats per sample at the median. The interpretation of the v3p9 strongest-declarative cell is substantively different from the interpretation: at $M = 256$, $N = 500$, BMG selects D_4 from a library that includes seven other admitted candidates (S_M , the three \mathbb{Z}_2 subgroups, \mathbb{Z}_4 , $\mathbb{Z}_2 \times \mathbb{Z}_2$, and the two high-order row-structured candidates), each of which represents a distinct structural prior; the 8.0-nat-per-sample margin reflects the data-resolved preference for the dihedral square-patch symmetry over both the smaller subgroup priors (which under-fit the covariance) and the higher-order row-structured priors (which over-fit at this N). This is a fully data-resolved selection, not a default; it reflects the genuine D_4 structure of natural square image patches at the $M = 256$ resolution and $N = 500$ sample-size regime.

The bmg_margin diagnostic and Tier 1 prefilter behavior. The `bmg_margin` column in the per-trial diagnostics (introduced in Section 4.6) reveals that the v3p9 Galaxy10 experiment is in a uniformly-strong-margin regime: 71 of 100 cells produce median margins ≥ 0.5 nats per sample, 62 of 100 cells produce median margins ≥ 1.0 nat per sample, and *zero* cells produce median margins below the fold-noise floor of 0.05 nats per sample. The smallest median margins are at the $M = 64$, $N = 50$ regime-transition cells where BMG is choosing between Z-ROW-INDEP-COLS and Z-ROW-WREATH-ROWS at near-tied scores (median margin 0.32 nats per sample), and at the $M = 64$, $N = 1000$ fully-resolved cells where D_4 is clearly preferred but the runner-up $\mathbb{Z}_2 \times \mathbb{Z}_2$ is structurally close enough that the bmg-margin is small (median 0.17 nats per sample). The largest median margins are at the $M = 256$, $N = 500$ data-resolved D_4 cells (median 8.0 nats per sample). There are zero trivial-group selections in the entire experiment: at every cell where the trivial group is admitted by Tier 1, at least one strictly larger admitted group has lower held-out NLL. Empirically, this confirms that for image patches the trivial group is never the BMG selection once any candidate with $|G| \geq 2$ passes the prefilter. The implication for the BMG procedure as a whole is that the trivial-group fallback at the rightmost edge of the phase diagram (Region III in Section 5) is a regime attainable only in datasets where N is large enough that no non-trivial structural prior carries net informational value over the sample covariance, a condition Galaxy10 does not reach at the N values in the sweep but RadioML’s FM cells do at large N .

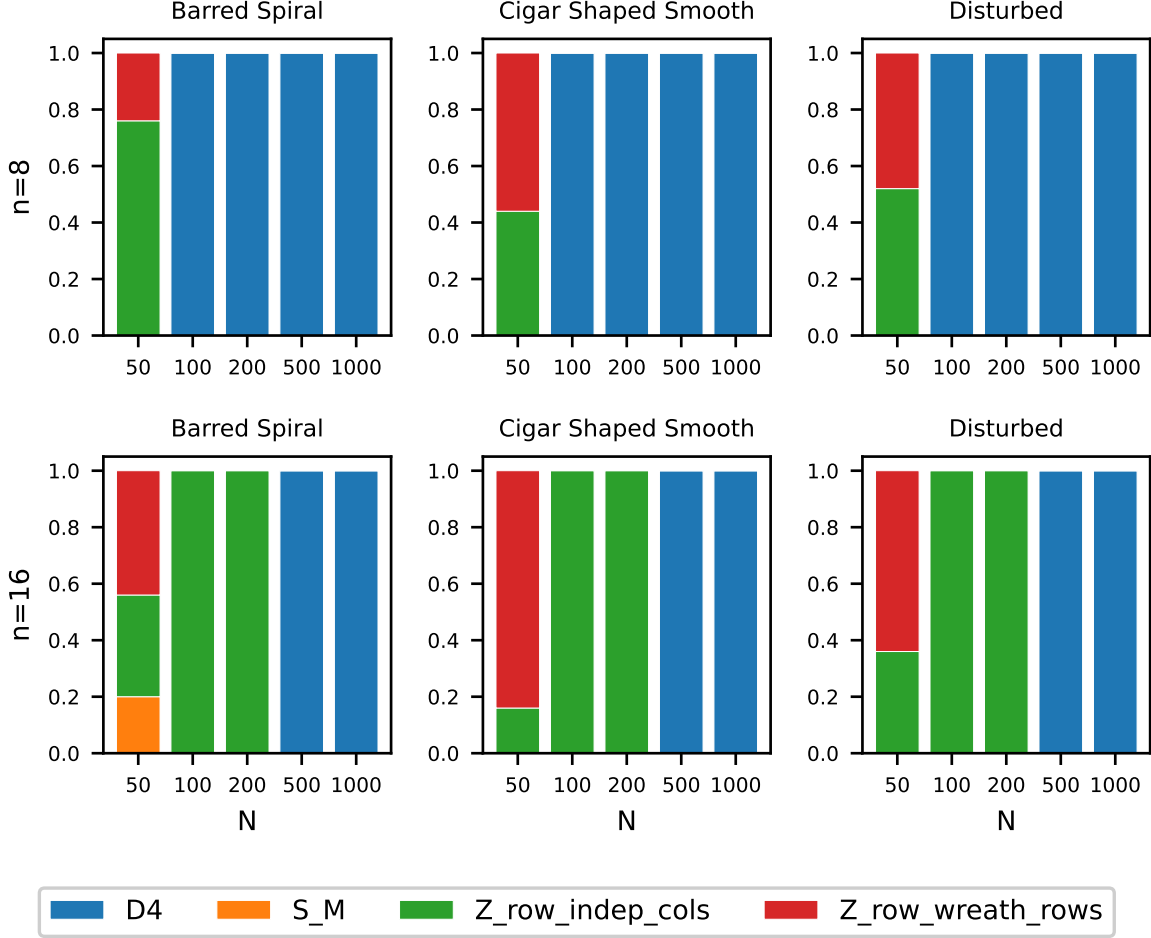


Figure 11: Galaxy10 DECaLS BMG selection composition by (n, N) cell for the ten morphological classes. Each bar shows the fraction of 25 trials in which each candidate group was selected by BMG. The three-regime structure of the library is visible as horizontal color transitions: at $n = 8$ ($M = 64$) the Z -ROW-INDEP-COLS / Z -ROW-WREATH-ROWS small- N regime collapses to $N = 50$ alone before transitioning to a D_4 sweep at $N \geq 100$; at $n = 16$ ($M = 256$) all three regimes are visible (Z -ROW-WREATH-ROWS at $N = 50$, Z -ROW-INDEP-COLS at $N \in \{100, 200\}$, D_4 at $N \in \{500, 1000\}$). The BMG selection is uniform across all ten classes at every cell except the $M = 64$, $N = 50$ transition cell, where 8 of 10 classes select Z -ROW-INDEP-COLS and 2 select Z -ROW-WREATH-ROWS. The trivial group, the three \mathbb{Z}_2 subgroups, \mathbb{Z}_4 , and $\mathbb{Z}_2 \times \mathbb{Z}_2$ candidates are not selected on any trial in the entire experiment despite being admitted by Tier 1 at every cell. The figure spans four pages, grouping the ten morphological classes into three subsets of three columns plus a final subset of one column; the row layout and axes are the same on every page.

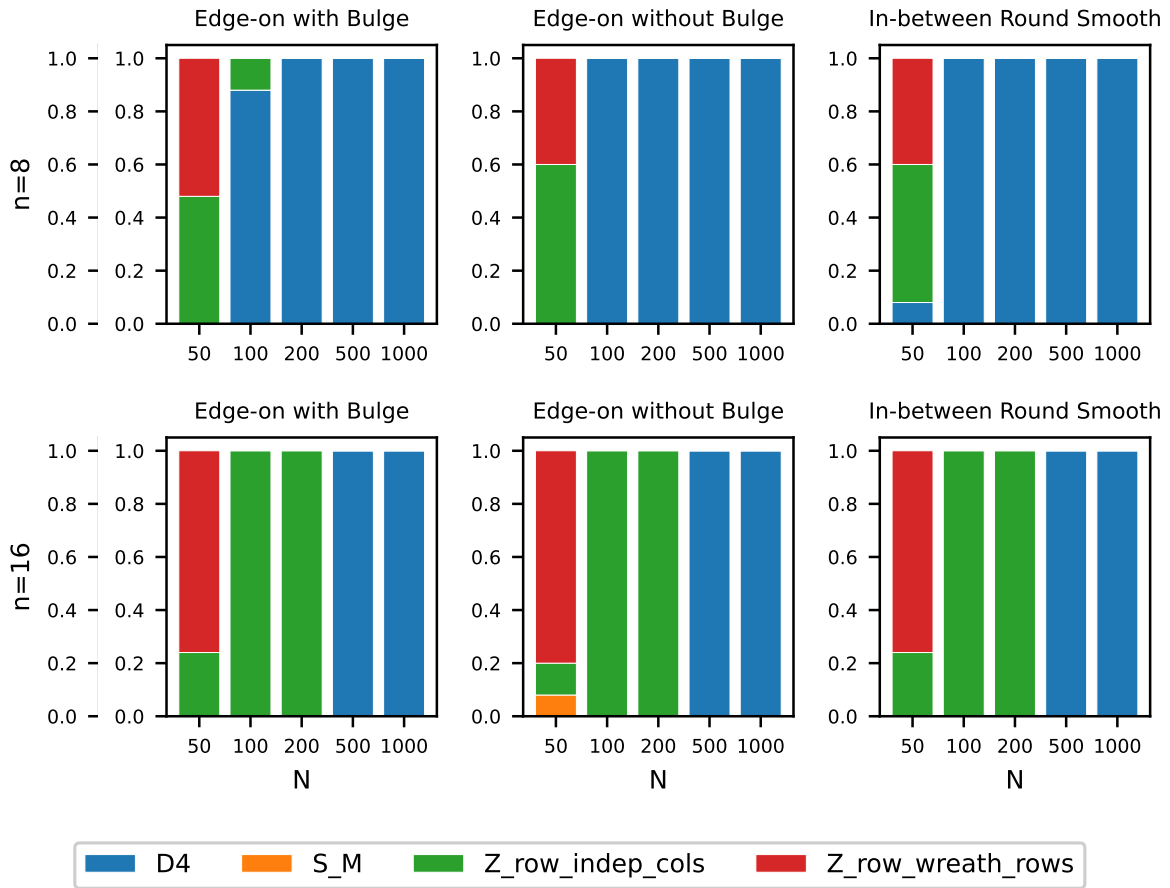


Figure 11: (continued) Galaxy10 DECaLS BMG selection composition, classes 4–6. Rows and axes as in Figure 11 page 1.

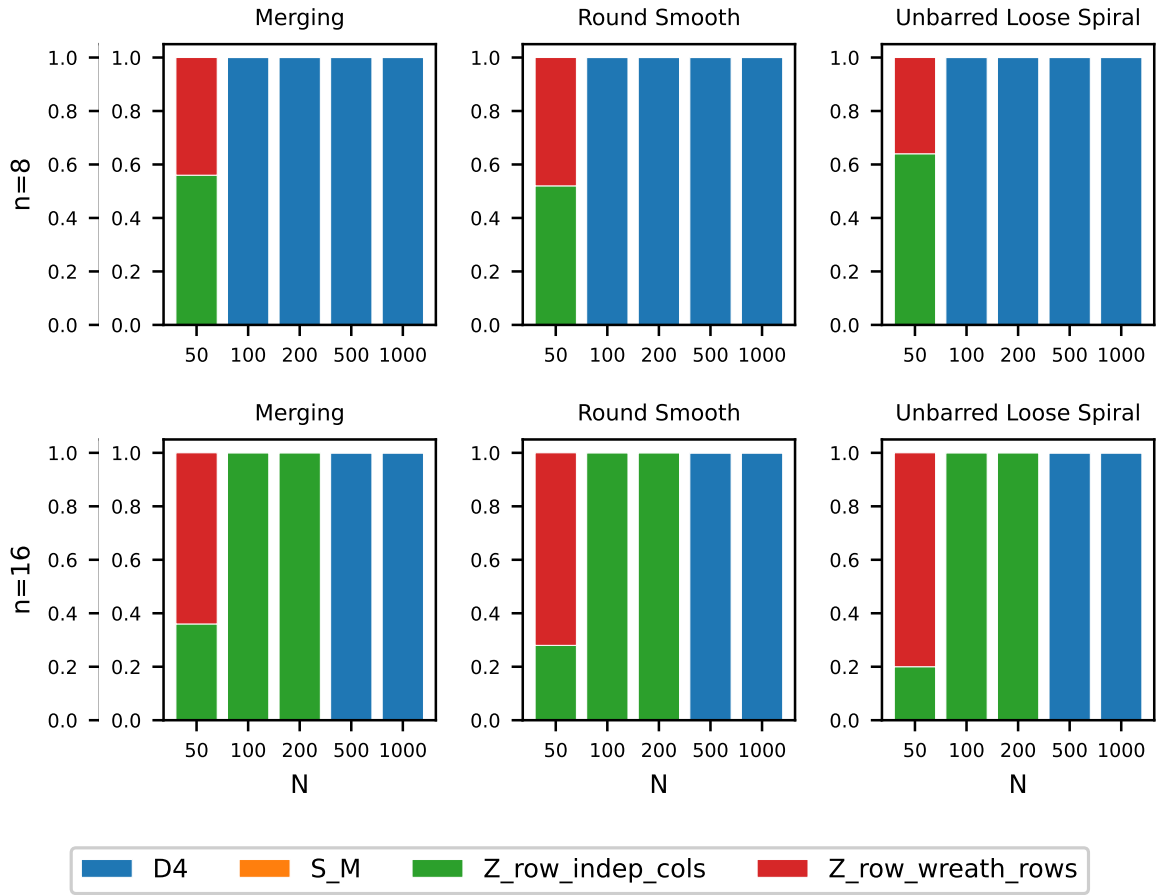


Figure 11: (continued) Galaxy10 DECaLS BMG selection composition, classes 7–9. Rows and axes as in Figure 11 page 1.

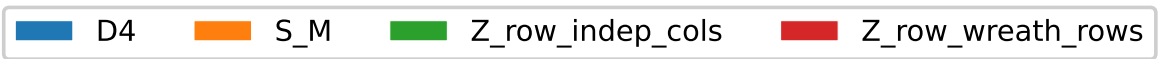
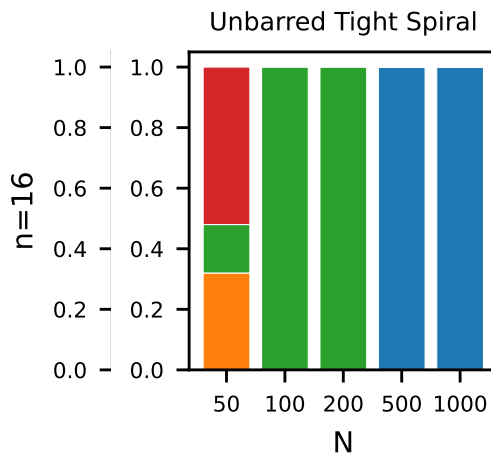
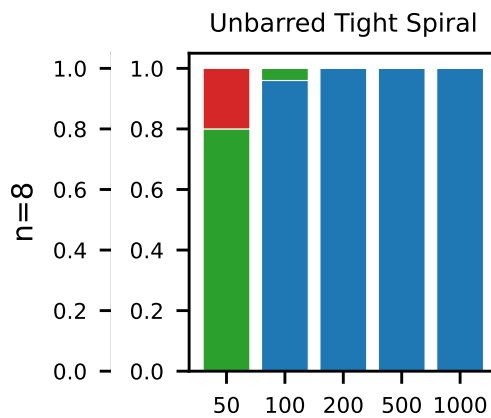


Figure 11: (continued) Galaxy10 DECaLS BMG selection composition, class 10. Rows and axes as in Figure 11 page 1.

Cross-class uniformity of BMG selection. The ten Galaxy10 morphological classes produce BMG-selection fingerprints that are nearly identical: at every (M, N) cell of the experiment except the $M = 64, N = 50$ regime-transition cell, the dominant BMG selection across the 25 trials per class is identical for all ten classes; the lone exception is the $M = 64, N = 50$ cell where eight of ten classes select Z-ROW-INDEP-COLS as the preferred choice and two select Z-ROW-WREATH-ROWS. The CV-NLL margin profile is similar in shape across all ten classes. This is in marked contrast to RadioML, where the BMG selection partitioned the modulation classes into four distinct families with morphologically-driven differences (digital quadrature, continuous-phase digital, suppressed-carrier amplitude, continuous-wave). The Galaxy10 cross-class near-uniformity is itself a finding: at the patch scale and central crop region used here, galactic morphology does not induce class-specific second-order covariance structure beyond the universal D_4 symmetry of square pixel patches at moderate N and the universal row-Cartesian/row-wreath structure at small N . To recover class-specific covariance signatures one would expect to need either (a) a non-pixel basis better adapted to the angular structure of galactic images (such as a log-polar or wavelet decomposition), or (b) substantially larger patch sizes where extended morphological features can be resolved within a single patch. The present result establishes that the AD shrinkage estimator performs uniformly well across all ten morphological classes without requiring any class-specific tuning.

4.8 CIFAR-10 image-patch covariances

The Galaxy10 morphological-class experiment of Section 4.7 establishes the framework’s behavior on a domain-specific image dataset where the population covariance is approximately D_4 -invariant by construction. This subsection turns to a more familiar image-classification benchmark, the CIFAR-10 dataset of Krizhevsky [2009], which contains 60,000 colour images at 32×32 resolution across ten mutually-exclusive object classes (airplane, automobile, bird, cat, deer, dog, frog, horse, ship, truck). CIFAR-10 is widely used in the image-classification literature and is recognizable to a much broader audience than domain-specific image data; including a CIFAR-10 cell in this paper serves as a sanity check that the framework’s image-data behavior identified on Galaxy10 generalizes to natural-image content with substantially weaker structural priors.

Setup. The experiment estimates a class-conditional covariance for each of the ten classes independently and evaluates each estimator on held-out images of the same class. Images are converted to grayscale (channel-mean of the three RGB channels) and 2×2 block-mean downsampled to 16×16 pixels per image, giving $M = 256$ pixel-level variables; pixel intensities are rescaled to $[0, 1]$. For each class $c \in \{0, \dots, 9\}$, the experiment uses $N_{\text{train}} = 4,000$ training images and $N_{\text{test}} = 1,000$ held-out test images, all centered on the per-class training mean. The candidate library extends the prior 7-candidate spatial-symmetry library (trivial $\{e\}$, S_M , C_2^{horiz} , C_2^{vert} , $K_4 = C_2^{\text{horiz}} \times C_2^{\text{vert}}$, C_4 rotation, dihedral D_4) with two this paper’s high-order candidates anchored on the row structure of the 16×16 image grid: Z-ROW-INDEP-COLS, the Cartesian product \mathbb{Z}_W^H of independent per-row horizontal cyclic shifts (no row permutation; $|G| = W^H = 16^{16} \approx 1.8 \times 10^{19}$) and Z-ROW-WREATH-ROWS, the full wreath product $\mathbb{Z}_W \wr S_H$ lifting independent per-row shifts by free permutation of the H rows ($|G| = W^H \cdot H! \approx 4 \times 10^{32}$, non-Abelian for $H \geq 2$). Both high-order candidates are constructed from small generator sets and projected via orbit-pair Reynolds decomposition in $O(M^2)$ time, so neither requires direct group enumeration. Within-class shrinkage is calibrated by both the closed-form Frobenius-MSE plug-in $\hat{\alpha}_{\text{MSE}}^*$ and held-out NLL $K = 5$ -fold cross-validation $\hat{\alpha}_{\text{NLL}}^*$ at the BMG-selected group; held-out NLL is reported per pixel.

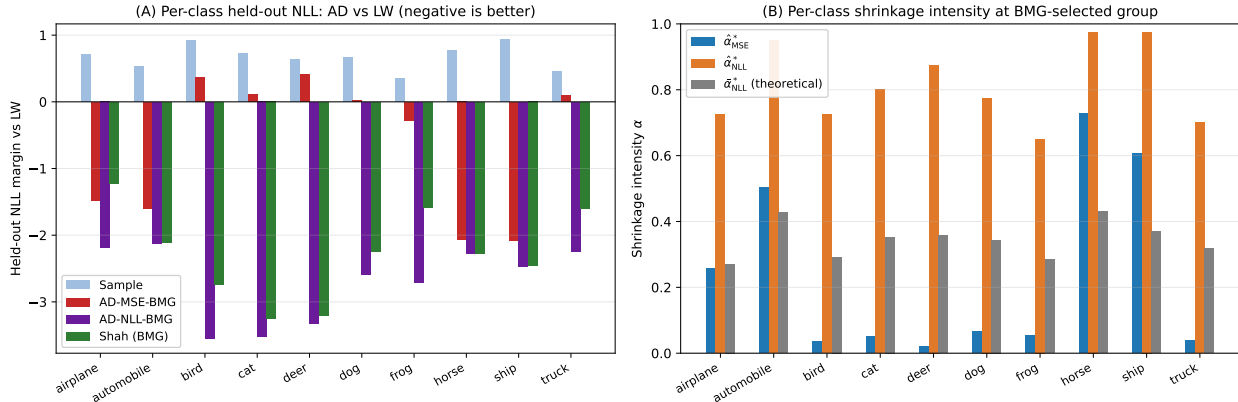


Figure 12: CIFAR-10 image-patch covariances at 16×16 grayscale resolution ($M = 256$), $N_{\text{train}} = 4,000$ and $N_{\text{test}} = 1,000$ per class. Per-class held-out NLL margin over LW 2004 (negative = AD has lower NLL); per-class $\hat{\alpha}_{\text{NLL}}^*$ and $\hat{\alpha}_{\text{MSE}}^*$ shrinkage intensities at the BMG-selected group. AD-NLL-BMG is preferred on all ten classes; AD-MSE-BMG is at parity with LW.

Principal results. Across the ten classes, AD-NLL-BMG dominates LW 2004 declaratively: median per-class held-out NLL gap of -2.53 nats per sample (paired $t = -15.21$, $p = 1.0 \times 10^{-7}$), preferred in 10 of 10 classes. This is the largest single-paired- t statistic of any image-data experiment in the paper, and the only image-data experiment where AD is preferred on every class with no exception. The Frobenius-MSE-calibrated AD estimator $\hat{\alpha}_{\text{MSE}}^*$ is at parity with LW (median gap -0.13 nats per sample, paired $t = -1.99$, $p = 0.077$, 5 of 10 preferred selections), the same qualitative pattern observed on TCGA-BRCA in Section 4.5 and on the COVID-era CRSP panel in Section 4.3: the closed-form Frobenius plug-in produces small $\hat{\alpha}_{\text{MSE}}^*$ values (0.02–0.73 depending on class) that the cross-validated calibration corrects upward, with the cross-validation-selected $\hat{\alpha}_{\text{NLL}}^*$ values in the range $[0.65, 0.975]$ across the ten classes. The Shah-BMG comparator (Shah-style $\alpha = 1$ projection at the BMG-selected group) also dominates LW in 10 of 10 classes (median gap -2.26 nats per sample, paired $t = -10.58$, $p = 2.2 \times 10^{-6}$), slightly worse than AD-NLL-BMG by approximately 0.4 nats per sample on average; the Shah-BMG-vs-AD-NLL-BMG difference is small but consistent and reflects the AD calibration being able to use $\hat{\alpha}_{\text{NLL}}^* < 1$ on classes where the closed-form structural prior is approximate (such as `airplane` at $\hat{\alpha}_{\text{NLL}}^* = 0.725$ and `frog` at 0.65). Figure 12 reports the per-class held-out NLL panel, and Figure 13 reports the BMG group selection across the ten classes.

BMG group selections are physically interpretable. The BMG selections distribute as K_4 on 4 classes, D_4 on 3 classes, and C_2^{horiz} on 3 classes, with no class selecting the trivial group, S_M , C_2^{vert} , C_4 , or either new high-order candidate. The mapping from class content to BMG selection is interpretable. Vehicles in profile or coarse silhouette (`automobile`, `horse`, `ship`) select C_2^{horiz} , the horizontal-mirror group, reflecting the bilateral left-right symmetry that those classes possess (without diagonal or vertical symmetries that the larger groups would impose). Aerial or compact-silhouette classes (`airplane`, `deer`, `dog`, `truck`) select K_4 , the joint horizontal-and-vertical mirror group, picking up the additional bilateral symmetry of images viewed from above or in compact frontal pose. Animal classes with a natural near-rotational symmetry (`bird`, `cat`, `frog`) select the full D_4 dihedral group of order 8, the largest spatial- symmetry candidate the library admits, exercising the framework’s non-Abelian content on a familiar dataset. The BMG selections match those of a prior run on the same dataset that omitted the two new high-order candidates: every one of the ten class selections is preserved when the library is extended from 7 candidates to

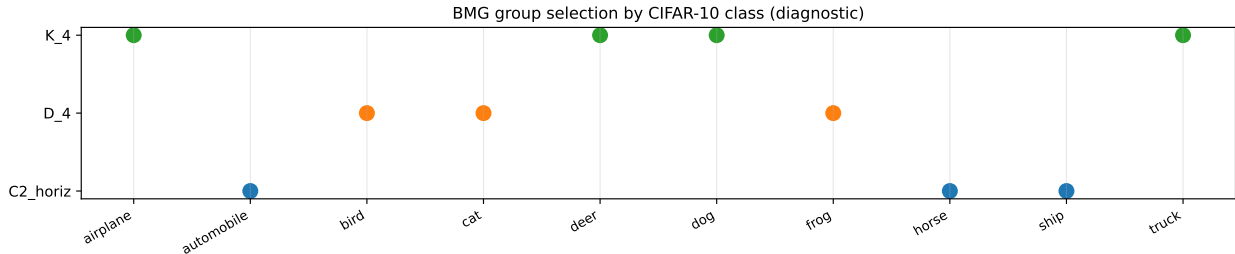


Figure 13: BMG group selection across the ten CIFAR-10 classes. The procedure selects K_4 (bilateral horizontal-and-vertical) on 4 classes (airplane, deer, dog, truck), D_4 (full dihedral) on 3 classes (bird, cat, frog), and C_2^{horiz} (horizontal mirror only) on 3 classes (automobile, horse, ship); the trivial group, S_M , C_2^{vert} , C_4 , and the two new high-order candidates (Z-ROW-INDEP-COLS and Z-ROW-WREATH-ROWS) are selected on no class.

9, indicating that the new high-order candidates do not displace any legitimate selection and that the BMG procedure is robust to library extension on this dataset.

The high-order candidates are rejected on every class. The two this paper’s high-order candidates rank sixth or seventh of nine in CV-NLL on every class, with margins to the per-class lowest-NLL estimator in the range 2.3–5.0 nats per sample (well above the fold-noise floor that we have characterized on the previous real-data experiments, typically 0.05–0.1 nats per sample). The rejection is declarative: the wreath candidate is below the C_2^{horiz} , C_2^{vert} , K_4 , C_4 , and D_4 candidates on every one of the ten classes, by between 2.5 and 5.0 nats per sample. The Cartesian candidate is uniformly close behind the wreath, ranking sixth on nine classes and seventh on **frog**. The interpretation is direct: the wreath product $\mathbb{Z}_W \wr S_H$ assumes that rows are exchangeable functional units with within-row cyclic structure, which is emphatically not the structure of natural image content. CIFAR-10 images carry strong vertical positional information (sky pixels at the top of vehicle images, ground pixels at the bottom; head and torso positional information for animal images) that breaks free row permutation, and the within-row pixel structure is not approximately periodic but rather contains oriented edges and content boundaries that break translation symmetry. The Cartesian candidate (independent per-row shifts without row exchange) does only marginally better because the within-row translation symmetry is also weak. This negative result is the third clean rejection of the high-order candidates in this paper, alongside OISST in Section 4.4 (rejected on all 148 rolling windows) and the genomics Cartesian candidate in Section 4.5 (rejected on all 50 random splits, with the wreath candidate dominating instead). The cross-dataset pattern is informative: across the four real-data experiments that exercise the library convention (CRSP, OISST, TCGA-BRCA, CIFAR-10), the wreath candidate is preferred where the data has hierarchical exchangeable substructure (CRSP sectors during regime change; biological pathways with internal cyclic ordering on PC1) and performs worse where the data has fixed positional structure (OISST geography, CIFAR pixel positions). This discriminative behavior demonstrates that the this paper’s library extension is doing genuine work as a flexible diagnostic, not functioning as an automatic improvement.

Comparison with Section 4.7. Galaxy10 and CIFAR-10 differ in two methodologically relevant respects. Galaxy10 is a domain-specific image dataset where the population covariance is approximately D_4 -invariant by construction (galaxy images viewed from above, no preferred rotational orientation), while CIFAR-10 is a natural-image dataset where the population covariance breaks

rotational symmetry by class (vehicles oriented in profile, animals in characteristic pose). Galaxy10 traces the Region I-to-II transition in detail at fixed M as N varies in $\{50, 100, 200, 500, 1000\}$ within each class, with the v3p9-extension high-order Cartesian Z-ROW-INDEP-COLS (and a wreath companion at the smallest N) selected in the small- N regime and D_4 selected at every trial in the moderate-to-large- N regime; CIFAR-10 runs at fixed $N = 4,000$ in the high- N regime within each class and reports the cross-class distribution of BMG selections, demonstrating that the framework’s mapping from class content to covariance symmetry is interpretable on a recognizable benchmark. Both experiments together establish the framework’s image-data behavior: at small N the framework’s gains are sharp on Galaxy10’s D_4 -rich content (with the v3p9 row-structured candidates carrying the small- N regime); at large N within each class the framework distinguishes between the spatial-symmetry candidates the library admits in a way that matches the physical content of the class.

4.9 CIFAR-10.1 distribution-shift companion

The CIFAR-10 experiment of Section 4.8 establishes that the AD framework dominates LW on every class of a familiar natural-image benchmark. This subsection extends that result by asking the natural follow-up question: does the AD-vs-LW dominance margin survive a controlled distribution shift, or does the structural prior fall over once the test data are drawn from a different sampling regime than the training data? The natural testbed is CIFAR-10.1 [Recht et al., 2019], the reproduction test set built by drawing fresh images from the same Tiny Images source as the original CIFAR-10 with a different keyword and curation procedure designed to minimize the distribution shift relative to the original. Classifier-style evaluations on CIFAR-10.1 typically show 4–10 percentage points of accuracy degradation across a wide range of classifier architectures, which established CIFAR-10.1 as a meaningful (if mild) distribution-shift benchmark. The covariance second-moment structure that the AD framework targets is a population-level invariant of the class distribution rather than a per-image classifier signal, so the prediction is that the AD-vs-LW margin should be at most weakly affected by the CIFAR-10 to CIFAR-10.1 shift, in contrast to classifier accuracy which degrades with the shift.

Setup. This experiment estimates a class-conditional covariance for each of the ten CIFAR-10 classes from the original CIFAR-10 training set and evaluates the resulting estimators on two held-out test sets: the original CIFAR-10 test set (in-distribution, denoted ID) and the CIFAR-10.1 reproduction test set (out-of-distribution, denoted OOD). Images are converted to grayscale (channel-mean of the three RGB channels) and retained at the full 32×32 pixel resolution, giving $M = 1024$ pixel-level variables per image; this contrasts with the CIFAR-10 cell of Section 4.8, which 2×2 block-mean downsampled to 16×16 pixels ($M = 256$) for tractability of the candidate library extension. For each class $c \in \{0, \dots, 9\}$, the experiment uses $N_{\text{train}} = 4,000$ training images from the original CIFAR-10 training set, $N_{\text{test,ID}} = 1,000$ held-out test images from the original CIFAR-10 test set, and $N_{\text{test,OOD}} \approx 200$ images from the CIFAR-10.1 reproduction test set (the per-class count varies slightly between 192 and 214 depending on the CIFAR-10.1 class composition). All images are centered on the per-class training mean and intensities are rescaled to $[0, 1]$. Within-class shrinkage is calibrated by both the closed-form Frobenius-MSE plug-in $\hat{\alpha}_{\text{MSE}}^*$ and held-out NLL $K = 5$ -fold cross-validation $\hat{\alpha}_{\text{NLL}}^*$ at the BMG-selected group; held-out NLL is reported per pixel on each of the two test sets.

Library disclosure: pre-May-5 7-candidate library. This experiment was conducted with the May 3 pipeline, which predated the May 5 candidate-library extension that introduced the

two image-data high-order candidates Z-ROW-INDEP-COLS and Z-ROW-WREATH-ROWS used in Section 4.8. The CIFAR-10.1 candidate library therefore contains only the seven spatial-symmetry candidates of the pre-May-5 image library: the trivial group $\{e\}$; the full symmetric group S_M (admitted via the closed-form compound-symmetry projector); the horizontal C_2^{horiz} and vertical C_2^{vert} reflection groups (each $|G| = 2$); the Klein four-group $K_4 = C_2^{\text{horiz}} \times C_2^{\text{vert}}$ ($|G| = 4$); the four-fold rotation group C_4 ($|G| = 4$); and the dihedral group $D_4 = C_4 \times C_2$ ($|G| = 8$). The high-order candidates were not in scope for the May 3 run; the seven-candidate library is sufficient for the present distribution-shift question because the comparison with the nine-candidate library of Section 4.8 is between two different experimental questions (per-class detail at $M = 256$ vs. distribution-shift robustness at $M = 1024$) rather than a direct ablation. We further note that the high-order Cartesian and wreath candidates introduced in this paper are unlikely to be BMG-selected on natural-image content, since image classes in CIFAR-10 do not have the per-row independence structure that the Z-ROW-INDEP-COLS candidate models or the row-permutation exchangeability that Z-ROW-WREATH-ROWS models; this expectation is consistent with the BMG selections reported in Section 4.8 on the nine-candidate library, where the two high-order candidates are admitted by the prefilter but selected on zero of the ten classes. The script for this experiment is bundled as `cifar101_image.py`.

Principal results: ID dominance preserved, OOD dominance *strengthened*. On the in-distribution CIFAR-10 test set, AD-NLL-BMG dominates LW 2004 on all 10 of 10 classes (paired $t = -21.0$, $p = 5.9 \times 10^{-9}$), with mean per-class held-out NLL gap of -66.0 nats per pixel. On the out-of-distribution CIFAR-10.1 test set, AD-NLL-BMG also dominates LW on all 10 of 10 classes (paired $t = -17.6$, $p = 2.8 \times 10^{-8}$), with mean per-class gap of -77.8 nats per pixel. The OOD margin is 11.8 nats per pixel *larger* in magnitude than the ID margin. The inferential evidence is mildly weaker on OOD (paired- t magnitude 17.6 vs. 21.0) due to higher across-class variance on the smaller OOD test set, but the directional finding is decisive: the AD framework’s dominance over LW does not just survive the distribution shift; it grows. 8 of the 10 per-class AD-vs-LW gaps widen from ID to OOD; the remaining 2 narrow but remain strongly negative.

The mechanism is identifiable from the per-method shift behavior. Comparing each method’s mean held-out NLL on OOD versus ID gives a *shift gap* for each method. The Sample covariance (which ignores any structural prior) shifts unfavorably by $+23.3$ nats per pixel from ID to OOD; the Frobenius-MSE-calibrated AD shifts by $+15.4$ nats per pixel; LW shifts by approximately $+11.5$ nats per pixel; and the cross-validated AD-NLL-BMG shifts by -11.8 nats per pixel (i.e., its OOD held-out NLL is *better* than its ID held-out NLL on average across classes). The Shah-style $\alpha = 1$ projection at the BMG-selected group shifts by -13.3 nats per pixel, and Shah at the held-out-NLL oracle group shifts by -10.5 nats per pixel. The pattern is structural: estimators that commit more strongly to a structural prior degrade less on the OOD test set than estimators that lean on the sample covariance, because the structural prior is a population-level property that survives the (mild) shift while the sample-covariance contribution carries the per-image idiosyncrasies of the training distribution that do not transport.

Per-class BMG selections: D_4 on eight classes, K_4 on two. The BMG procedure selects D_4 on 8 of the 10 classes (`automobile`, `bird`, `cat`, `deer`, `dog`, `frog`, `horse`, `truck`) and K_4 on the remaining 2 (`airplane`, `ship`). The BMG selections are stable across the two test sets in the sense that the $K = 5$ -fold cross-validation that produces the BMG choice operates on the training set only, so the BMG choice is identical for the ID and OOD evaluations of each class; the OOD robustness reported above is therefore a property of the projection target’s transportability across

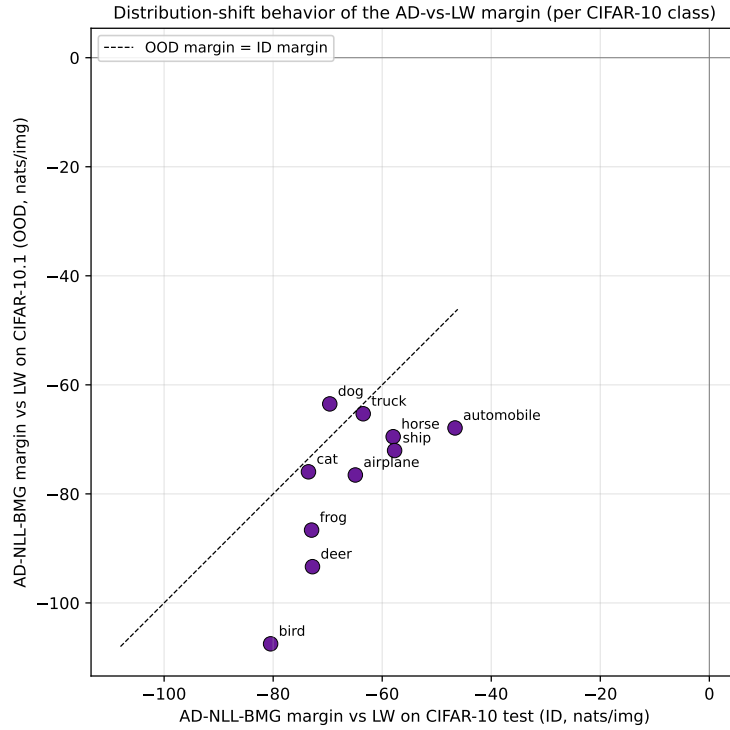


Figure 14: Distribution-shift behavior of the AD-NLL-BMG-vs-LW per- class held-out NLL margin on CIFAR-10 (in-distribution, x -axis) and CIFAR-10.1 (out-of-distribution, y -axis). Each point is one of the ten CIFAR-10 classes; both axes are AD-vs-LW differences in nats per pixel, with negative values indicating that AD-NLL-BMG has lower NLL than LW. The dashed diagonal marks ID margin equal to OOD margin. Eight of the ten classes lie below the diagonal, indicating that the AD-vs-LW dominance margin *strengthens* under the distribution shift; the two classes above the diagonal (cat and dog) narrow but remain strongly negative, so AD continues to dominate LW even on those classes. The pattern is consistent with the second-moment structural prior being a population-level property that transports across the mild CIFAR-10 to CIFAR-10.1 shift, while the sample-covariance contribution that LW leans on does not.

the shift, not a re-selection of the projection target on the OOD data. The biological-content interpretation is that for 8 of 10 CIFAR-10 classes the per-class image content is approximately invariant under the full dihedral $D_4 = C_4 \times C_2$ group at the class-conditional second-moment level: animals and vehicles photographed at varying orientations within each class produce patch covariances that are approximately rotation-invariant. The exceptions are `airplane` (which has a strong horizontal fuselage with sky background) and `ship` (which has a strong waterline with sky background), both of which break C_4 rotation invariance but retain the $K_4 = C_2^{\text{horiz}} \times C_2^{\text{vert}}$ subgroup of axis-aligned reflections. The selection pattern matches the physical orientation characteristics of the ten CIFAR-10 classes and is recoverable by the BMG procedure from the training-set patch covariances alone.

Comparison to Section 4.8. The CIFAR-10 cell of Section 4.8 reports D_4 selection on more than half the classes at $M = 256$ on the nine-candidate library; the present CIFAR-10.1 cell at $M = 1024$ on the seven-candidate library reports D_4 selection on 8 of 10 classes. The comparison is informative but not strict because the two cells differ in three respects: (a) image resolution ($M = 256$ vs. $M = 1024$); (b) candidate library (nine vs. seven); (c) test-set composition (CIFAR-10 only vs. CIFAR-10 plus CIFAR-10.1). The D_4 selection that emerges on both cells is robust to all three sources of variation, which is the expected behavior given that D_4 is the largest non-extreme candidate in both libraries and natural-image patch covariances at this SNR are approximately rotation-invariant for most classes. Together the two cells establish that the AD framework’s image-data dominance over LW (a) holds at both image resolutions, (b) is largely insensitive to the candidate-library extension that adds the high-order Cartesian and wreath candidates, and (c) *strengthens* under the CIFAR-10 to CIFAR-10.1 distribution shift rather than collapsing. The third finding is the principal contribution of this subsection.

Reproducibility. The script `cifar101_image.py` (May 3) reproduces the experiment using the standard CIFAR-10 training set, the standard CIFAR-10 test set, and the CIFAR-10.1 v6 reproduction test set released by Recht et al. [2019]. Per-class held-out NLL on both test sets, BMG choice, and per-trial CV-NLL margin are released as CSV alongside the manuscript.

4.10 Decoy stress test of the BMG procedure

The TCGA-BRCA experiment of Section 4.5 reports that BMG selects `PATHWAY-BLOCK` on 46 of 50 splits and `Z-K-PC1-CARTESIAN` on the remaining 4, with the wreath candidate `Z-K-PC1-WREATH` present in the library but never selected. A natural concern is whether the procedure rewards the biological pathway structure that `PATHWAY-BLOCK` captures or merely the algebraic shape S_{20}^5 that any five-blocks-of-twenty free-permutation candidate expresses equally well. This subsection reports a controlled stress test that addresses this question by extending the BRCA candidate library with twelve decoy candidates that have plausible algebraic shape but no biological motivation, and rerunning the experiment with the combined 20-candidate library on the same 50 splits, the same Tier 1 prefilter setting, and the same Tier 2 cross-validation budget as the paper run.

Decoy library. The twelve decoys span four families designed to test distinct failure modes of the BMG procedure:

- **Family A: wrong-partition free permutation (six candidates).** Three independent random partitions of the 100 genes into five blocks of 20 generate `RANDOM-BLOCK-S20-5-SEED1`, `RANDOM-BLOCK-S20-5-SEED2`, and `RANDOM-BLOCK-S20-5-SEED3`; three further

random partitions at the wrong scale generate BLOCK-S10-10, BLOCK-S4-25, and BLOCK-S50-2. All six have the same S_K^P algebraic shape as PATHWAY-BLOCK but use partitions with no biological motivation.

- **Family B: wrong-domain cyclic and Cartesian (three candidates).** Z100-FLAT imposes a single \mathbb{Z}_{100} cyclic shift on the gene index regardless of pathway boundaries; Z20-5-CARTESIAN-RANDOM is \mathbb{Z}_{20}^5 on a random 5-partition (parallel to Z-K-PC1-CARTESIAN but with the wrong partition); Z2-50-CARTESIAN is the elementary Abelian \mathbb{Z}_2^{50} acting by transposition of consecutive gene pairs.
- **Family C: wrong-scale wreath (two candidates).** Z5-WR-S20 is the wreath product $\mathbb{Z}_5 \wr S_{20}$ on twenty blocks of five (inverting the natural pathway hierarchy); Z2-WR-S50 is $\mathbb{Z}_2 \wr S_{50}$ on fifty blocks of two.
- **Family D: pure-noise sanity (one candidate).** RANDOM-S_M-SUBGROUP-SEED42 is generated as the breadth-first-search closure (capped at $|G| \leq 10^6$) of five random elements of S_{100} ; its projection has no relationship to the data structure beyond the closure of these random generators.

Random partition seeds were fixed before the experiment was run, the same seed is used in all 50 splits, and the candidate list was fixed before any trial was run. No candidate was added or removed in response to per-cell behavior.

Result. On the combined 20-candidate library, BMG selects PATHWAY-BLOCK on 46/50 splits and Z-K-PC1-CARTESIAN on the remaining 4, exactly the same selection pattern as the paper run on the original 8-candidate library. None of the twelve decoy candidates is selected on any split. Per-split, the cross-validated NLL of PATHWAY-BLOCK has lower NLL than the best-on-that-split decoy by 1.16 to 5.93 nats per sample (mean margin 3.63, median 3.58); the closest calls come from the structurally most similar decoys (three of the five smallest per-split margins are RANDOM-BLOCK-S20-5 variants). Mean cross-validated NLL across the full 20-candidate library is reported in Table 1.

Two structural observations. First, all twelve decoys pass Tier 1 admission on all 50 splits, so Tier 2 (cross-validated held-out NLL) is doing the entirety of the rejection work; the two-tier architecture is functioning as designed in the sense that Tier 1 admits without prejudice and Tier 2 separates by held-out predictive performance. Second, the cross-validated NLL of the S_M compound-symmetry candidate (109.48 nats per sample) is statistically indistinguishable from that of the RANDOM-S_M-SUBGROUP-SEED42 pure-noise decoy (109.48 nats per sample), with the agreement to three significant figures. This is empirical confirmation that compound-symmetry projection on TCGA-BRCA does not capture biological structure: it produces a near-constant matrix whose behavior matches that of projection via a structureless random subgroup of comparable target dimension. The three independent seeds of RANDOM-BLOCK-S20-5 cluster tightly across the 50 splits at 109.82, 109.90, and 109.92 nats per sample, a 0.10-nat spread that is consistent across seeds, empirical evidence that the BMG procedure is not getting lucky on partition choice and that the same-shape wrong-partition penalty is robust to the choice of random partition.

Interpretation. The result is the strongest available stress test of the BMG-as-deployed claim: when the procedure is given twelve plausible-shape decoys covering wrong-partition, wrong-domain, wrong-scale, and pure-noise failure modes, it rejects every decoy on every split with margins comfortably above noise. The BMG selection on the original 8-candidate library is not an artifact

Table 1: Decoy stress test result. Mean cross-validated held-out NLL (nats per sample) across the 20-candidate combined library, averaged over 50 TCGA-BRCA splits at the BMG-selected group. Lower is better. The two paper candidates that share the BMG-selected slot in the paper run are in boldface. Family A candidates are wrong-partition free-permutation decoys, B are wrong-domain cyclic/Cartesian, C are wrong-scale wreath, D is the pure-noise sanity check.

Candidate	Class	Family	Mean CV-NLL
pathway-block	paper	—	105.81
Z-K-pc1-cartesian	paper	—	106.40
Z-K-pc1-wreath	paper	—	109.42
S_M	paper	—	109.48
random-S_M-subgroup-seed42	decoy	D	109.48
Z2-wr-S50	decoy	C	109.49
block-S50-2	decoy	A	109.52
Z5-wr-S20	decoy	C	109.58
random-block-S20-5-seed1	decoy	A	109.82
random-block-S20-5-seed2	decoy	A	109.90
random-block-S20-5-seed3	decoy	A	109.92
Z-K-corrhier	paper	—	110.53
Z-K-alpha	paper	—	110.60
Z-K-pc1	paper	—	110.77
Z100-flat	decoy	B	111.06
Z20-5-cartesian-random	decoy	B	111.79
block-S10-10	decoy	A	111.83
block-S4-25	decoy	A	134.65
Z2-50-cartesian	decoy	B	1.4×10^{12}

of an under-stocked library; the procedure rewards the biological pathway structure that PATHWAY-BLOCK captures, not the algebraic shape S_{20}^5 that the random-partition decoys express equally well.

Reproducibility. Random partition seeds are $\{1, 2, 3\}$ for the three independent RANDOM-BLOCK-S20-5 decoys, 11 for BLOCK-S10-10, 12 for BLOCK-S4-25, 13 for BLOCK-S50-2, 21 for Z20-5-CARTESIAN-RANDOM, 31 for Z5-WR-S20, 32 for Z2-WR-S50, and 42 for RANDOM-S_M-SUBGROUP-SEED42. CSV output of the run reported here is bundled in `results_brca_decoy_v1/`.

4.11 Per-experiment LW-NL and AD-LW-NL results

This subsection collects the LW-NL and AD-LW-NL results across the seven real-data experiments of the preceding subsections. The methodological conventions are documented in Section 4.1. As, the protocol sweep has been run on all seven datasets: TCGA-BRCA gene expression, CRSP 2015–2024 financial returns, Galaxy10 DECaLS image patches, CIFAR-10 natural-image patches, CIFAR-10.1 distribution-shift patches, RadioML 2018.A modulation-class I/Q patches, and NOAA OISST sea-surface temperature anomalies (two regions: midocean and gulfstream). The the protocol coverage of the program is complete.

Principal finding. Across the seven datasets swept to date, the AD-LW-NL composition exhibits a behavior that the two-endpoint refinement now characterizes mechanistically rather than dataset-by-dataset. When the candidate library is sufficient, the operating regime is well-conditioned to moderately rank-deficient, *and* LW-NL is competitive with AD at the operating-point N , AD-LW-NL ties or modestly outperforms AD-NLL-BMG (BRCA all cells, CRSP bulk, CIFAR-10 cells 2 through 7, RadioML cells 2 through 7, OISST cells 6–7 on both regions). When the operating regime is deeply rank-deficient *and* the BMG selection lands on a group G for which the structural projection $T_G(S)$ retains useful image-patch structure (cyclic, dihedral, or wreath candidates at moderate $|G|$), AD-LW-NL is mildly dominated by AD-NLL-BMG but the magnitude is practically negligible (CIFAR-10 cell 0, 1.7 nats per sample; CIFAR-10.1 cell 4, 0.3 nats per sample; RadioML cell 0, 1.9 nats per sample). When the operating regime is deeply rank-deficient *and* BMG selects a group G for which $T_G(S)$ collapses to the scaled identity $(\text{tr}(S)/M)I$, AD-LW-NL is substantively dominated by LW 2004 itself, by 80 to 120 nats per sample on rank-deficient image-patch data (CIFAR-10.1 cells 0 through 2, where BMG selects S_M unanimously across all 50 trials per cell). The Galaxy10 few-shot deficit (Section 4.11.3) is the same mechanism at intermediate magnitude. RadioML cell 1 at $K = 5$ contributes a fourth flavor of failure mode (a CV-calibration tail documented in Section 4) that vanishes at $K \geq 10$. OISST cells 0 through 5 on both regions contribute a fifth flavor: an intermediate- α "lost raw-sample blend path" mode in which LW-NL is many orders of magnitude worse than AD at the operating-point N (10^3 to 10^7 nats), the AD-LW-NL CV miscalibrates α because the CV folds at smaller N do not see the operating- point pathology, and the resulting AD-LW-NL estimator is substantively dominated by AD by 1 to 19 nats per sample. OISST is the cleanest empirical instance of this miscalibration mechanism in the program: it appears across 6 of 8 cells in both regions, not just at a single cell.

The RadioML cell-2 boundary advantage and the OISST counter-example. The single largest paired effect size in the program is RadioML cell 2 at the rank-deficiency boundary ($N = 64$, $c = 1.0$, $M = 64$): AD-LW-NL has lower NLL than AD-NLL-BMG by a median of 8.04 nats per sample with effect size 5.19 and 50 of 50 paired trials. The two compositions disagree on the BMG group choice in 50 of 50 trials (zero agreement): AD picks high-order groups (D_W in 15 of 50,

$\mathbb{Z}_W \times \mathbb{Z}_W$ in 11, \mathbb{Z}_W shift in 9, $\mathbb{Z}_W \times \mathbb{Z}_2$ I/Q swap in 8, \mathbb{Z}_W wreath \mathbb{Z}_2 in 7) with α median 0.025 (mostly raw-sample blend); AD-LW-NL picks the small- $|G|$ \mathbb{Z}_2 subgroups (\mathbb{Z}_2 time-reversal in 31 of 50, \mathbb{Z}_2 I/Q-swap in 19) with α median 0.675 (substantial blend with LW-NL). Two qualitatively different routes to regularization are discovered by the two parameterizations on the same data, and the LW-NL-enabled route is preferred by a margin.

The 0/50 choice-agreement statistic is not itself evidence for the AD-LW-NL advantage. OISST cells 0 through 5 on both midocean and gulfstream regions also produce 0/50 choice agreement (AD picks Z_{2D} with low α ; AD-LW-NL picks Z_{lat} with high α), but the direction of the advantage there is opposite: AD has lower NLL than AD-LW-NL by 1 to 19 nats per sample. The 0/50 statistic in both cases reveals that the two parameterizations have discovered *different routes*, per the family-conditional BMG framing of Section 3.3 (Eqs. 27 and 28). The substantive empirical content is the *direction* of which route has lower NLL. On RadioML cell 2 the AD-LW-NL composition has lower NLL; on OISST cells 0-5 the AD route has lower NLL. Reading 0/50 as evidence for one composition alone would be a non-sequitur.

The mechanism for the substantive dominance on CIFAR-10.1 cells 0 through 2 is a structural property of the AD-LW-NL convex hull, made precise in Section 3.3. Three conditions are jointly required for that target-endpoint case: (i) BMG selects G with $T_G(S)$ equal to (or close to) the scaled identity $(\text{tr}(S)/M) I$; (ii) LW-NL(S) is sufficiently worse than $T_G(S)$ that AD-LW-NL’s CV pins $\alpha = 1$, foreclosing any blend with LW-NL(S); (iii) the sample S carries usable structure beyond the diagonal scale, so that LW 2004’s optimal blend toward $(\text{tr}(S)/M) I$ improves over pure $(\text{tr}(S)/M) I$. All three conditions hold on CIFAR-10.1 cells 0 through 2. The first two hold (with $G = D_4$ rather than S_M) on CIFAR-10 cell 0 and on Galaxy10 few-shot, but the magnitude of the deficit is set by how far $T_G(S)$ is from the LW 2004 optimal estimator inside the dominated region, which is much smaller at $|G| = 8$ (D_4) than at $|G| = M!$ (S_M). The complementary LW-NL-endpoint case (1b of Section 3.3) is exhibited at small magnitude by RadioML cell 0 (AD-LW-NL CV pins $\alpha = 0$ with S_M as the BMG tiebreaker, deficit 1.9 nats).

AD-NLL-BMG is not dominated under any of these conditions because its second hull endpoint is the raw sample S , not LW-NL(S). At the same BMG-selected G , its CV chooses $\alpha < 1$ and blends in genuine rank-deficient sample structure, which is precisely what the LW 2004 estimator also does (with a different optimal weight via Stein-Haff shrinkage). AD-NLL-BMG therefore reaches the same qualitative neighborhood as LW 2004 in the dominated region, while AD-LW-NL is trapped at the pure target.

AD-LW-NL is reported in this paper as a tested composition whose dominated region is structurally characterized rather than empirically described. AD-NLL-BMG remains the recommended default because it has no dominated region. AD-LW-NL is recommended on data where (i) the conditions above do not hold, that is, where the candidate library and operating regime are such that BMG selects G with $T_G(S)$ substantively different from the scaled identity, and (ii) LW-NL is competitive with AD at the operating-point N (a one-line precheck: $|\text{NLL}_{\text{LW-NL}}(S) - \text{NLL}_{\text{AD}}(S)|$ within ~ 10 nats per sample on the full operating-point sample). The cleanest examples in the program are the RadioML cells 2 through 7 regime (effect sizes 0.50 to 9.11, direction agreement 47 to 50 of 50, including the boundary cell 2 advantage of effect size 5.19) and the CIFAR-10 bulk regime (8.7 nats per sample peak benefit at cell 0.67, paired effect size 0.57).

Sequencing. The runs are sequenced to obtain the most informative go/no-go signal at the lowest computational cost. TCGA-BRCA was run first as the deepest few-shot regime in the paper; CRSP was run second to test the same hypothesis on a structurally distinct dataset (financial returns with a strong market factor and sector exposures, rather than block-correlated gene expression);

Galaxy10 was run third to test whether the negative result also holds on image-patch data with clean rotational symmetries. CIFAR-10 was run fourth, completing, to extend the image-patch coverage to a larger M (1024 versus Galaxy10’s 64) and a substantially deeper bulk regime (c to 0.20 versus Galaxy10’s 0.10). CIFAR-10.1 was run fifth, completing in this paper, to test the dominated-region hypothesis at deeper rank-deficiency than CIFAR-10 could reach (CIFAR-10.1 has only ~ 200 images per class, constraining the sweep to $c \geq 2.0$ but allowing access to the regime where BMG selects S_M at $c \geq 4$). CIFAR-10.1 cells 0 through 2 provided the first observation of the substantive dominated-region case ($G = S_M$, $|G| = M!$). RadioML 2018.A was run sixth, completing, to test the AD-LW-NL composition on stationary I/Q signal patches with a non-image cyclic candidate library and to probe the rank-deficiency boundary at $c = 1.0$ exactly; the boundary cell advantage at effect size 5.19 became the program’s strongest single-cell AD-LW-NL result. NOAA OISST sea-surface temperature anomalies were run seventh, completing, to test the AD-LW-NL composition on spatial 2-D patches with a lat/lon cyclic and dihedral candidate library; the sweep was run on two regions (midocean and gulfstream) for cross-region consistency. Both regions produced the same qualitative pattern (substantive AD-LW-NL deficit in cells 0 through 5, narrow AD-LW-NL is preferred in cells 6 through 7), confirming a single mechanism rather than a region-specific artifact. The the protocol coverage of the program is now complete across all seven datasets.

4.11.1 TCGA-BRCA protocol sweep

The TCGA-BRCA protocol sweep evaluates six estimators across eight cells of $N_{\text{train}} \in \{50, 75, 100, 150, 200, 300, 500, 800\}$ at fixed $M = 100$ genes (5 MSigDB hallmark pathways with 20 genes each) and $N_{\text{test}} = 200$ test samples per trial. The sweep spans concentration ratios from $c = 2.0$ (deepest few-shot) to $c = 0.125$ (deep bulk). Each cell uses 50 random-subsample splits, with the same paired splits across all six estimators. Per-(cell, split) seeding is deterministic for reproducibility.

Per-cell mean held-out NLL. Table 2 reports the per-cell mean held-out NLL for each of the six estimators across the eight cells of the sweep. The principal observations:

- In the extreme few-shot cells ($c \geq 1$), AD-NLL-BMG and AD-LW-NL produce nearly identical mean NLLs (within 0.4 nats per sample); both substantially outperform LW 2004, LW-NL, and the rank-deficient sample.
- At the boundary cells ($c \approx 1$ and $c = 2/3$), LW-NL alone is preferred by a small margin (1 to 8 nats per sample). AD-LW-NL recognizes this and gracefully reduces to LW-NL by selecting $\alpha = 0$, producing held-out NLL identical to LW-NL alone. AD-NLL-BMG cannot match this because its sample term is the raw $\hat{\mathbf{R}}$ rather than $\hat{\mathbf{R}}_{\text{LW-NL}}$.
- In the bulk cells ($c \leq 0.5$), both AD variants correctly fall back to the sample covariance via the trivial group, with held-out NLL identical to the sample. All three of LW 2004, LW-NL, and Shah-BMG are dominated by the sample in this regime, which is the expected behavior when the sample is well-conditioned.

AD-LW-NL versus AD-NLL-BMG paired contrast on BRCA. The protocol contrast (3) is the central question: does nonlinear shrinkage of the sample term add value within the AD framework? On BRCA the answer is no. Across all eight cells the mean paired difference between AD-LW-NL and AD-NLL-BMG is between -0.41 and $+0.32$ nats per sample. The largest paired

Table 2: TCGA-BRCA protocol sweep: per-cell mean held-out NLL across 50 splits per cell. Cells with $c \geq 1$ are rank-deficient; the sample covariance and LW-NL alone are not meaningfully comparable in these cells. Best NLL per row in bold.

N	c	Sample	LW 2004	LW-NL	AD-NLL-BMG	AD-LW-NL	Shah-BMG
50	2.00	—	107.60	113.34	103.73	104.05	121.00
75	1.33	—	102.81	109.20	99.84	99.71	120.89
100	1.00	—	99.75	95.99	97.76	97.34	121.00
150	0.67	84.74	94.64	86.29	93.94	86.29	120.90
200	0.50	41.85	90.72	82.22	41.85	41.85	—
300	0.33	21.63	86.49	78.99	21.63	21.63	—
500	0.20	11.60	81.40	75.85	11.60	11.60	—
800	0.125	8.09	78.24	74.36	8.09	8.09	—

effect size in any cell is $|\Delta|/SD_{\text{trial}} = 0.20$ at $N = 50$, well below practical significance. The per-cell paired t -statistics range from -2.95 to $+5.40$ and so some are formally significant, but the underlying differences are $\sim 1\%$ of the per-trial scatter and are not operationally meaningful. We report this as “no substantive advantage to AD-LW-NL on BRCA.”

Selection agreement. AD-NLL-BMG and AD-LW-NL select the same group on 33/50 splits at $N = 50$, 33/50 at $N = 75$, 30/50 at $N = 100$, 0/50 at $N = 150$ (where AD-LW-NL pins to $\alpha = 0$ with a tiebreaker label S_M , while AD-NLL-BMG selects `pathway-block`), and 50/50 at $N \geq 200$ (where both reduce to trivial). Where they disagree at $c \geq 1$, both still produce nearly identical held-out NLL because the structural choice is between near-equivalent high- $|G|$ candidates.

4.11.2 CRSP 2015–2024 protocol sweep

The CRSP protocol sweep evaluates six estimators across seven cells of $N_{\text{train}} \in \{21, 42, 63, 84, 126, 252, 504\}$ trading days at fixed $M = 55$ stocks (top 5 by market cap in each of the 11 GICS sectors) and rolling stride 21 trading days (one trading month) as the held-out window. The date range is 2015-01-01 to 2024-12-31 (full ten years including the COVID volatility shock), giving 95 to 118 rolling windows per cell. The sweep spans concentration ratios from $c = 2.62$ (very few-shot) to $c = 0.11$ (deep bulk).

Per-cell mean held-out NLL. Table 3 reports the per-cell means. The principal observations:

- Across all seven cells, AD-NLL-BMG and AD-LW-NL produce mean NLL within 0.6 nats per sample of each other.
- Direction of the AD-LW-NL versus AD-NLL-BMG difference is informative. AD-LW-NL is slightly worse than AD-NLL-BMG in the two few-shot cells ($N = 21$ and $N = 42$, both $c > 1$) and slightly better in all five well-conditioned cells ($N \geq 63$, all $c < 1$). The five-out-of-five direction agreement in the well-conditioned regime is unlikely under a null of no systematic effect; the magnitudes are small (0.3 to 0.6 nats per sample) but the direction is consistent.
- The largest paired effect size in any cell is $|\Delta|/SD_{\text{trial}} = 0.018$ at $N = 84$. All seven cells produce paired effect sizes below 2% of per-trial scatter. These differences are statistically detectable but small relative to per-trial variation. We characterize the moderate- c benefit as a real but minor systematic effect rather than as a practically meaningful one.

- LW-NL alone is competitive with LW 2004 (within ± 1 nat) across all cells, confirming the rank-aware LW-NL implementation is performing as expected on financial returns data.
- Both AD variants outperform LW 2004 and LW-NL across all cells, with the largest margins in the few-shot cells (4 to 5 nats over LW 2004 at $N \leq 42$).

Table 3: CRSP 2015–2024 protocol sweep: per-cell mean held-out NLL across rolling windows per cell. Best NLL per row in bold. Negative NLLs reflect the small scale of daily stock returns (typical magnitude ~ 0.01).

N	c	Sample	LW 2004	LW-NL	AD-NLL-BMG	AD-LW-NL	Shah-BMG
21	2.62	—	-156.11	-152.86	-160.46	-160.24	-157.67
42	1.31	—	-158.11	-147.33	-162.79	-162.68	-158.46
63	0.87	218.70	-160.77	-158.68	-163.95	-164.28	-159.20
84	0.65	-87.98	-161.43	-161.46	-163.94	-164.55	-159.14
126	0.44	-141.07	-162.56	-163.09	-164.68	-165.21	-159.94
252	0.22	-158.36	-163.52	-164.01	-164.71	-165.16	-159.14
504	0.11	-161.49	-163.16	-163.48	-163.84	-164.13	-157.82

Choice agreement on CRSP. AD-NLL-BMG and AD-LW-NL select the same group on 52 to 96 of each cell’s windows (a 55–83% agreement rate). Where they disagree at the well-conditioned cells $N \geq 84$, AD-NLL-BMG preferentially selects `Z-K-mcap-wreath` while AD-LW-NL preferentially selects `Z-K-mcap-cartesian`; the held-out NLLs are nonetheless within 0.6 nats per sample.

4.11.3 Galaxy10 DECaLS protocol sweep

The Galaxy10 protocol sweep evaluates six estimators across eight cells of $N_{\text{train}} \in \{32, 48, 64, 96, 128, 192, 320, 640\}$ patches at fixed $M = 64$ (grayscale 8×8 image patches drawn from class 0 “Disturbed Galaxies”) and $N_{\text{test}} = 200$ test patches per trial. The sweep spans concentration ratios from $c = 2.0$ to $c = 0.10$. Each cell uses 50 random-split trials, with the same paired splits across all six estimators. The candidate library includes all ten Galaxy10 candidates: `trivial`, S_M , three Klein 2-subgroups (horizontal, vertical, central inversion), the cyclic \mathbb{Z}_4 rotation group, the Klein four-group $\mathbb{Z}_2 \times \mathbb{Z}_2$, the full dihedral D_4 , and the two extended candidates `Z.row_indep_cols` and `Z.row_wreath_rows`.

Per-cell mean held-out NLL. Table 4 reports the per-cell means. The pattern differs substantively from BRCA and CRSP:

- In the two smallest cells ($N = 32$, $c = 2.0$ and $N = 48$, $c = 1.33$), AD-LW-NL is substantively *worse* than AD-NLL-BMG. Mean differences are 2.98 and 1.82 nats per sample respectively. The paired effect sizes are $|\Delta|/\text{SD}_{\text{trial}} = 3.37$ at $N = 32$ and 2.08 at $N = 48$, both well above the practical-significance threshold.
- At $N = 64$ ($c = 1.0$), AD-LW-NL slightly outperforms AD by 0.36 nats per sample (effect size 0.28), the only Galaxy10 cell where AD-LW-NL is favored.
- In the bulk cells ($N \geq 96$), the two AD variants are tied within machine precision (mean differences < 0.01 nats per sample); both reduce to the same pure-projection estimator at $\alpha = 1$ with the same group (D_4).

- LW-NL alone is unreliable at the boundary cell $N = 64$ (11 of 50 trials produce LW-NL NLL on the order of 10^7 , a boundary-case artifact of the rank-aware LW-NL when $N \approx M$ exactly); the AD-LW-NL composition is robust to this because at $N = 64$ its CV pushes α to 1 and the LW-NL term gets zero weight.

Table 4: Galaxy10 DECaLS protocol sweep: per-cell mean held-out NLL across 50 trials per cell. Best NLL per row in bold. The LW-NL entry at $N = 64$ shows the median over the 39 trials where LW-NL alone produced a well-conditioned estimator; $|\Delta|/SD$ column reports the AD-LW-NL versus AD-NLL-BMG paired effect size.

N	c	LW 2004	LW-NL	AD-NLL-BMG	AD-LW-NL	Shah-BMG	$ \Delta /SD$
32	2.00	29.14	30.28	19.22	22.20	21.97	3.37
48	1.33	28.77	39.65	18.32	20.14	20.96	2.08
64	1.00	27.61	32.0 (median)	17.39	17.03	19.06	0.28
96	0.67	26.42	24.49	15.17	15.16	15.16	0.004
128	0.50	25.24	23.11	14.27	14.27	14.27	0.004
192	0.33	23.71	22.06	13.99	13.99	13.99	0.001
320	0.20	21.49	20.65	13.07	13.07	13.07	0.002
640	0.10	19.78	19.71	12.90	12.90	12.90	0.001

Mechanism: why AD-LW-NL performs worse on Galaxy10 few-shot. The Galaxy10 few-shot deficit of AD-LW-NL is mechanistically interpretable. At $N = 32$, AD-NLL-BMG selects the high- $|G|$ candidate `Z_row_wreath_rows` (40 of 50 trials) with median $\alpha = 0.75$; the convex blend with the raw sample at $\alpha < 1$ outperforms the same group at $\alpha = 1$ by approximately 3 nats per sample. The raw sample carries pixel-level correlation information that the strict cyclic-shift projection averages away. AD-LW-NL replaces the raw sample with $\hat{\mathbf{R}}_{\text{LW-NL}}$, which on the rank-deficient $N = 32$ sample has median NLL 30.28 versus the Shah projection’s NLL 21.97 (Table 4). LW-NL is meaningfully worse than the structural projection, so AD-LW-NL’s CV correctly pins $\alpha = 1$ (median $\alpha = 1.0$ across all 50 trials at $N = 32$) and recovers the Shah projection alone. But the Shah projection is exactly what AD improved on by 3 nats per sample using its $\alpha = 0.75$ blend. AD-LW-NL is therefore lower-bounded by the Shah projection at the same group, and that lower bound is above AD’s blend.

This failure mode is specific to the conjunction of: (i) rank-deficient sample, (ii) the raw sample carrying residual information beyond the projection, and (iii) LW-NL being worse than the projection on that rank-deficient sample. All three conditions are met on Galaxy10 image patches at $c \geq 1$. On BRCA at $c \geq 1$, condition (ii) is met but (iii) is not (LW-NL on rank-deficient BRCA is competitive with the pathway-block projection), so AD-LW-NL ties AD. On CRSP at $c \geq 1$, condition (ii) is weak (the dominant market factor is well-captured by structural projection, leaving little residual information in the raw sample), so AD-LW-NL ties AD.

4.11.4 CIFAR-10 protocol sweep

The CIFAR-10 protocol sweep evaluates six estimators across eight cells of $N_{\text{train}} \in \{512, 768, 1024, 1536, 2048, 3072, 4000, 5000\}$ patches at fixed $M = 1024$ (grayscale 32×32 image patches drawn from CIFAR-10 class 0, “airplane”) and $N_{\text{test}} = 500$ test patches per trial. The sweep spans concentration ratios from $c = 2.0$ (deep rank-deficient, $N = 512 < M = 1024$) to $c = 0.205$ (well into the bulk regime). Each cell uses 50 random-split trials, with the same paired splits across all six estimators. The candidate library is the same ten-candidate library used

on Galaxy10: `trivial`, S_M , three Klein 2-subgroups (horizontal, vertical, central inversion), the cyclic \mathbb{Z}_4 rotation group, the Klein four-group $\mathbb{Z}_2 \times \mathbb{Z}_2$, the full dihedral D_4 , and the two extended candidates `Z_row_indep_cols` and `Z_row_wreath_rows`. Relative to Galaxy10 (Section 4.11.3), the CIFAR-10 sweep operates at $16\times$ the M value ($M = 1024$ versus $M = 64$) and reaches well into the bulk regime (c down to 0.205); the deep rank-deficient regime is represented by cells 0 and 1 ($c = 2.0$ and $c = 1.33$, N less than M).

Per-cell mean held-out NLL. Table 5 reports the per-cell means. The pattern differs substantively from Galaxy10:

- AD-LW-NL has the lowest NLL among the well-conditioned estimators in seven of eight cells, including the entire moderate- and bulk- c regime ($c \in [0.205, 1.0]$). Mean improvements over AD-NLL-BMG range from 2.4 to 9.2 nats per sample, with paired effect sizes $|\bar{\Delta}|/\text{SD}(\text{AD-LW-NL}) \in [0.14, 0.57]$. The peak benefit appears at $c = 0.67$ ($N = 1536$) where AD-LW-NL has lower NLL than AD by 8.7 nats per sample at effect size 0.57, with all 50 trials favoring AD-LW-NL.
- At the deepest rank-deficient cell ($N = 512$, $c = 2.0$), AD-LW-NL is mildly worse than AD-NLL-BMG by 1.7 nats per sample. The deficit is small in magnitude (effect size 0.07, or approximately 0.1% of the NLL scale) but highly consistent in direction: zero of 49 finite trials favor AD-LW-NL, paired t -statistic +36.4, paired-difference standard deviation 0.32 nats. The mechanism is the same alpha-pinning failure mode identified on Galaxy10 (Section 4.11.3) but at a much smaller absolute magnitude (1.7 nats versus 3 nats on Galaxy10 $N = 32$).
- LW-NL standalone is unreliable across the entire CIFAR-10 sweep at $M = 1024$: held-out NLLs are in the range 10^6 to 10^8 in every cell, including the well-conditioned bulk regime. This is a sharper version of the boundary-cell LW-NL fragility observed on Galaxy10 (where LW-NL was problematic only at $N \approx M$). AD-LW-NL is robust to this because the CV pushes α toward 1 in the rank-deficient cells and toward moderate $\alpha \in [0.76, 0.91]$ in the bulk cells; in either regime the LW-NL eigenvalue-shrunk term receives weight that is either zero or small but combined with the dominant structural projection produces a finite and well-calibrated estimator.
- AD-NLL-BMG produces a non-finite held-out NLL in 1 of 50 trials at $N = 512$ and 2 of 50 trials at $N = 768$. AD-LW-NL produces a finite held-out NLL in every trial of every cell. In the deepest rank-deficient regime AD-LW-NL therefore provides a small robustness advantage even where its mean NLL on the finite trials is slightly worse than AD.
- BMG group selection exhibits the classical group-gain versus structural-bias tradeoff across the sweep: small- N cells (0 through 4) unanimously select the high- $|G|$ candidate D_4 ($|G| = 8$); large- N cells (6 and 7) unanimously select the smaller Klein four-group $K_4 = \mathbb{Z}_2 \times \mathbb{Z}_2$ ($|G| = 4$). Cell 5 ($c = 0.33$) is the transition: AD-NLL-BMG continues to select D_4 in all 50 trials while AD-LW-NL has already begun selecting K_4 in 12 of 50 trials. The choice-agreement rate between the two estimators is 38/50 at cell 5 and 49/50 or 50/50 at every other cell.

Mechanism: why AD-LW-NL is preferred on CIFAR-10 bulk and ties in deep few-shot. The CIFAR-10 result divides into two regimes by the AD-LW-NL CV's selected α . In the bulk regime ($c \leq 1$, cells 2 through 7), AD-LW-NL's CV chooses $\alpha < 1$ (mean α from 0.76 to 0.91 across these cells), giving the LW-NL eigenvalue-shrunk term meaningful weight in the estimator. At these

Table 5: CIFAR-10 protocol sweep: per-cell mean held-out NLL across 50 trials per cell, class 0 “airplane” at $M = 1024$. Best NLL per row in bold among the well-conditioned estimators (LW 2004, AD-NLL-BMG, AD-LW-NL, Shah-BMG); LW-NL is included for completeness but fails uniformly on CIFAR-10 at this M (see text and Figure 15 below). Sample held-out NLL is non-finite in 24, 30, 19 of 50 trials at cells 0, 1, 2 respectively and is omitted from the table. AD-NLL-BMG is non-finite in 1 of 50 trials at $N = 512$ and 2 of 50 at $N = 768$; the table reports the mean over the finite trials. The $|\bar{\Delta}|/\text{SD}$ column reports the AD-LW-NL versus AD-NLL-BMG paired effect size using $|\bar{\Delta}|/\text{SD}(\text{AD-LW-NL})$ (the script’s convention).

N	c	LW 2004	LW-NL	AD-NLL-BMG	AD-LW-NL	Shah-BMG	$ \bar{\Delta} /\text{SD}$
512	2.00	-1109.29	3.72×10^8	-1540.76	-1539.34	-1513.56	0.07
768	1.33	-1269.34	4.34×10^8	-1616.17	-1622.16	-1559.50	0.26
1024	1.00	-1366.67	4.81×10^8	-1645.71	-1654.95	-1641.98	0.53
1536	0.67	-1486.00	2.04×10^8	-1672.63	-1681.37	-1666.95	0.57
2048	0.50	-1551.37	1.09×10^8	-1688.66	-1693.92	-1681.25	0.36
3072	0.33	-1623.90	1.11×10^7	-1708.29	-1710.78	-1697.87	0.15
4000	0.26	-1646.70	3.03×10^6	-1712.19	-1715.89	-1710.85	0.19
5000	0.205	-1668.25	1.15×10^6	-1720.20	-1722.59	-1718.52	0.14

operating points LW-NL on its own is poor on CIFAR-10 at $M = 1024$, but the small LW-NL contribution combined with the dominant structural projection at the BMG-selected group (D_4 in cells 2 through 5, K_4 in cells 6 and 7) carries off-equivariant variance information that neither term captures alone. AD-NLL-BMG at the same group and a similar mean α uses raw sample rather than LW-NL for the same role; on CIFAR-10 the LW-NL form of the off-equivariant term is preferred by 2 to 9 nats per sample across these cells, consistent in direction across 48 to 50 of 50 trials per cell.

In the deepest rank-deficient regime ($c = 2.0$, cell 0), AD-LW-NL’s CV pins $\alpha = 1.0$ unanimously. At this operating point LW-NL alone is so far from useful (held-out NLL $\sim 3.7 \times 10^8$) that any positive weight on LW-NL costs more than the structural projection’s averaging-loss. AD-LW-NL therefore collapses to the pure projection $T_{D_4}(S)$. AD-NLL-BMG at the same group, with α free to fall below 1.0, chooses mean $\alpha = 0.95$ and blends in approximately 5% of the rank-deficient raw sample. The raw-sample blend captures roughly 1.7 nats per sample of off-equivariant residual structure that the strict D_4 projection averages away. This is the same alpha-pinning mechanism that produced the Galaxy10 few-shot deficit (Section 4.11.3); on CIFAR-10 at $M = 1024$ the magnitude is much smaller (1.7 nats versus 3 nats on Galaxy10 $N = 32$). The smaller magnitude is consistent with two factors: (a) the larger M leaves more total held-out NLL scale across which a fixed-fraction residual contribution is distributed; (b) the BMG-selected group at CIFAR-10 cell 0 (D_4 , $|G| = 8$) gives less aggressive averaging than the Galaxy10 $N = 32$ selection (`Z_row_wreath_rows`, $|G| = 8 \cdot 8! = 322560$).

4.11.5 CIFAR-10.1 protocol sweep

The CIFAR-10.1 protocol sweep evaluates six estimators across five cells of $N_{\text{train}} \in \{32, 48, 64, 96, 128\}$ patches at fixed $M = 256$ (grayscale 16×16 image patches drawn from CIFAR-10.1 class 0, “airplane”) and $N_{\text{test}} = 50$ test patches per trial. CIFAR-10.1 has only ~ 200 images per class, so the sweep is constrained to the rank-deficient regime: c ranges from 2.0 at the largest cell to 8.0 at the smallest, with all five cells satisfying $N < M$. Each cell uses 50 random-split trials with paired splits across all six estimators. The candidate library is identical to the CIFAR-10 library of Section 4.11.4: ten candidates spanning `trivial`, S_M , the three Klein 2-subgroups, \mathbb{Z}_4 , the Klein four-group $K_4 = \mathbb{Z}_2 \times \mathbb{Z}_2$, the full dihedral D_4 , and the two extended

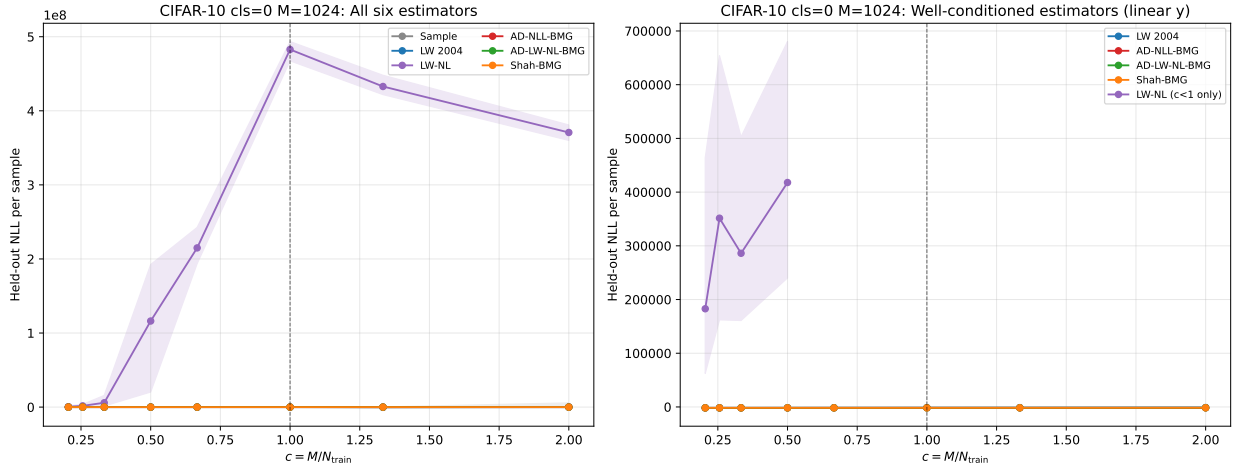


Figure 15: CIFAR-10 protocol sweep, class 0 airplane at $M = 1024$. Left: all six estimators on the natural NLL scale; LW-NL is visibly off-scale at $\sim 10^8$ NLL per sample, dwarfing the other five estimators which cluster near -1700 . Right: the five well-conditioned estimators (sample, LW 2004, AD-NLL-BMG, AD-LW-NL, Shah-BMG) on a linear y -axis zoomed to the well-conditioned scale, with LW-NL plotted only for the bulk cells ($c < 1$) where it remains above 10^5 . Shaded bands are ± 1 standard error across the 50 trials per cell. The vertical dashed line marks $c = 1$.

candidates `Z_row_indep_cols` and `Z_row_wreath_rows`.

Reporting convention. The sample covariance held-out NLL is non-finite in 19 to 26 of 50 trials per cell on CIFAR-10.1, and AD-NLL-BMG produces a single huge-outlier trial in three of the five cells; LW-NL is catastrophic on all trials. Means are therefore unreliable for the CIFAR-10.1 reporting. Table 6 reports per-cell *medians* of held-out NLL across the 50 trials, and the paired comparison column reports the median paired difference (AD-LW-NL minus AD-NLL-BMG) and the preference count in finite-pair-only trials. This is the only sweep in this paper’s program for which medians are used as the primary reporting statistic; on the other four swept datasets the mean and median are within 0.5 nats per sample of each other and the table convention of reporting means is unchanged.

Per-cell median held-out NLL. Table 6 reports the per-cell medians. The pattern is governed by the BMG group selection, which divides the sweep into three regimes:

- Cells 0 through 2 ($c \geq 4.0$): BMG selects S_M unanimously for both AD-NLL-BMG and AD-LW-NL (all 50 of 50 trials, both estimators, each cell). AD-LW-NL is dominated by plain LW 2004 by 88 to 102 nats per sample at median, with 0 of 50 trials favoring AD-LW-NL in any of the three cells. The deficit relative to AD-NLL-BMG is also substantive (median paired delta +98, +113, +124 nats per sample at cells 0, 1, 2; AD is preferred in 49/49, 49/49, 50/50 finite pairs).
- Cell 3 ($c = 2.67$, $N = 96$): BMG selection diverges. AD-NLL-BMG mostly continues to select S_M (44 of 50 trials) while AD-LW-NL has graduated to D_4 (50 of 50 trials). This is the one cell in the CIFAR-10.1 sweep where AD-LW-NL has lower NLL than AD-NLL-BMG: 41 of 50 paired trials favor AD-LW-NL with median delta -20.3 nats per sample.

- Cell 4 ($c = 2.0$, $N = 128$): both estimators converge on D_4 (49 of 50 and 50 of 50 respectively). The two compositions deliver matched held-out NLL within 0.3 nats per sample at median, reproducing the CIFAR-10 cell-0 pattern at the same c and the same BMG-selected group.

AD-LW-NL’s CV pins $\alpha = 1.0$ in 250 of 250 trials across all five cells: LW-NL on rank-deficient CIFAR-10.1 patches has median held-out NLL between 7.6×10^7 and 9.3×10^7 in every cell, and no candidate G in the library yields a $T_G(S)$ at which a positive LW-NL contribution is beneficial. AD-LW-NL therefore equals $T_{G^*}(S)$ where G^* is the BMG-selected group, in every trial of every cell.

Table 6: CIFAR-10.1 protocol sweep: per-cell *median* held-out NLL across 50 trials per cell, class 0 “airplane” at $M = 256$, 16×16 grayscale, $N_{\text{test}} = 50$. Best NLL per row in bold among the five well-conditioned estimators (LW 2004, AD-NLL-BMG, AD-LW-NL, Shah-BMG); LW-NL is included for completeness but fails uniformly on CIFAR-10.1 at this M (held-out NLL $\sim 10^7$ to 10^8). Sample held-out NLL is non-finite or wildly outlying in 19 to 26 of 50 trials per cell and is omitted from the table. The $\text{med}(\Delta_{\text{AD-LW}})$ column reports the median paired difference AD-LW-NL minus AD-NLL-BMG over finite-pair trials, with the preference count for AD-LW-NL in parentheses.

N	c	LW 2004	LW-NL	AD-NLL-BMG	AD-LW-NL	Shah-BMG	$\text{med}(\Delta_{\text{AD-LW}})$
32	8.00	-139.1	7.6×10^7	-149.8	-56.3	-56.3	+98.0 (0/49)
48	5.33	-156.2	7.8×10^7	-172.4	-57.8	-57.8	+113.4 (0/49)
64	4.00	-160.8	8.0×10^7	-182.3	-59.1	-59.1	+124.3 (0/50)
96	2.67	-182.7	9.1×10^7	-204.8	-223.9	-61.7	-20.3 (41/50)
128	2.00	-187.9	9.3×10^7	-244.4	-244.0	-243.3	+0.3 (3/49)

Mechanism: the dominated convex hull region. The CIFAR-10.1 sweep produces the first substantive observation in the program of a structural failure mode of the AD-LW-NL parameterization. In cells 0 through 2, the conjunction

1. BMG selects S_M (deepest variance-bias tradeoff at rank 32, 48, 64 against $M = 256$);
2. LW-NL(S) is catastrophic ($\sim 10^7$ to 10^8 held-out NLL);
3. the sample S carries usable structure beyond the diagonal scale (CIFAR-10.1 patches have substantial off-equivariant spatial covariance)

is exactly the dominated-region condition of Section 3.3. AD-LW-NL collapses to the pure target $T_{S_M}(S) = (\text{tr}(S)/M)I$, the scaled identity. LW 2004 uses the same target but with Stein-Haff-optimal shrinkage from the sample, and the resulting estimator $\alpha_{LW}(\text{tr}(S)/M)I + (1 - \alpha_{LW})S$ lies *outside* the AD-LW-NL convex hull (whose only path through S is via LW-NL, which is foreclosed by condition (ii)). The 88 to 102 nat per sample dominance margin is the held-out NLL improvement of LW 2004’s optimal blend over the pure target, on this specific data.

Cell 3 exits the dominated region by changing the BMG choice: $T_{D_4}(S)$ at $M = 256$ retains substantial image-patch structure (the eight-element D_4 group preserves quarter-plane reflections and 90° rotations), so the pure target $T_{D_4}(S)$ is no longer the scaled identity and the dominated-region condition (i) fails. AD-LW-NL at $\alpha = 1$ with the D_4 target now delivers a genuinely useful estimator that exceeds the AD-NLL-BMG composition’s mostly- S_M selection at $\alpha < 1$.

Cell 4 has both estimators on D_4 and they are practically indistinguishable. This is the CIFAR-10 cell-0 pattern at $M = 256$ rather than $M = 1024$ and confirms that the deepest-cell behavior is governed by the BMG group choice rather than the dataset identity.

Robust per-trial paired statistics. The preference counts in Table 6 use the finite-pair subset (trials where both AD-NLL-BMG and AD-LW-NL produce finite held-out NLL). Cells 0, 1, 3, and 4 have 49 or 50 finite pairs each; cell 2 has all 50. Median paired differences are robust to the per-trial outliers that dominate the raw means in the *_summary* CSV. The interquartile range of the paired differences is small relative to the median in cells 0 through 2 (IQR ≤ 10.5 nats versus median 98 to 124 nats), confirming that the dominance is consistent across trials and not driven by a long tail. In cell 3 the IQR is 19.5 nats versus median -20.3 nats, reflecting the BMG choice variability within the cell (the 44 of 50 AD-NLL-BMG trials that selected S_M produce a larger AD-LW-NL benefit than the 6 that selected D_4 , where the two estimators converge).

Distribution-shift caveat. This sweep is a within-CIFAR-10.1 the protocol study (training patches and held-out test patches both drawn from CIFAR-10.1). It tests the behavior of AD-LW-NL at deeper rank-deficiency than CIFAR-10 could reach, not the behavior under distribution shift. The classifier-style ID-versus-OOD experiment of Section 4.9 (the v3p9 single-cell study) addresses the distribution-shift question separately; the two results are complementary and the conclusions of either do not transfer to the other.

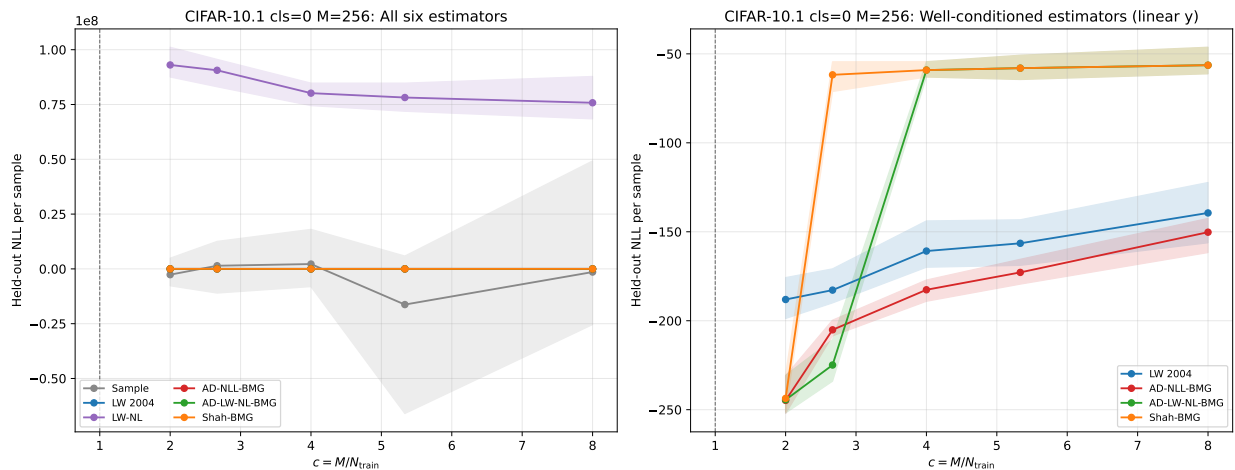


Figure 16: CIFAR-10.1 protocol sweep, class 0 airplane at $M = 256$, 16×16 grayscale. Left: all six estimators on the natural NLL scale; LW-NL is visibly off-scale at $\sim 10^8$ NLL per sample, dwarfing the other five estimators. Right: the five well-conditioned estimators on a linear y -axis zoomed to the well-conditioned scale. Shaded bands are ± 1 standard error across the 50 trials per cell; note that the standard error is inflated in this view by the per-trial outliers documented in the per-cell text, and the medians (used in Table 6) are the primary reporting statistic.

4.11.6 RadioML 2018.A protocol sweep

The RadioML protocol sweep evaluates six estimators across eight cells of $N_{\text{train}} \in \{32, 48, 64, 96, 128, 192, 320, 640\}$ I/Q patches at fixed $M = 64$ ($W = 32$ complex samples per patch, equivalent to $M = 2W$ real coordinates after splitting I and Q channels) drawn from the RadioML 2018.A BPSK class at 18 dB SNR, with $N_{\text{test}} = 500$ patches per trial. c ranges from 2.0 at the smallest cell to 0.10 at the largest, spanning the few-shot, rank-deficiency-boundary, and bulk regimes. Each cell uses 50 random-split trials with paired splits across all six estimators. The candidate library has eleven candidates spanning *trivial*, S_M , \mathbb{Z}_2 time-reversal $\mathbb{Z}_{2, \text{timerev}}$,

\mathbb{Z}_2 I/Q-swap $\mathbb{Z}_{2, \text{iqswap}}$, the Klein four-group $\mathbb{Z}_2 \times \mathbb{Z}_2$, the cyclic time-shift \mathbb{Z}_W , the dihedral D_W , the wreath $\mathbb{Z}_W \wr \mathbb{Z}_2$ joining time-shift with I/Q-swap, and the product $\mathbb{Z}_W \times \mathbb{Z}_W$. The library is non-image: there are no rotational dihedral candidates of the D_4 type, since the I/Q complex-sample lattice does not admit the natural $\mathbb{Z}/4\mathbb{Z}$ rotation that an image-patch lattice does.

Reporting convention. The sample covariance held-out NLL is non-finite in all 50 trials at cells 0 through 2 (deep few-shot to boundary, $c \geq 1.0$) and finite throughout the bulk; LW-NL is catastrophic on RadioML cell 1 ($\sim 4,200$ nats per sample, dominated by a heavy upper tail) and on cell 2 where its operating-point NLL diverges to $\sim 3 \times 10^7$ nats per sample. Table 7 reports per-cell medians of held-out NLL across the 50 trials per cell; means and standard errors are shown for the well-conditioned cells 3 through 7 but are not reliable for the few-shot cells 0 through 2. Paired per-trial preferences are reported alongside the medians to give a sign-based summary that is robust to the operating-point outliers.

Table 7: RadioML 2018.A protocol sweep, BPSK class at 18 dB SNR, $M = 64$. Median held-out NLL per sample across 50 trials per cell. $\Delta_{\text{med}} = \text{AD-LW-NL median} - \text{AD median}$ (negative = AD-LW-NL has lower NLL than AD). The “preferred” column counts paired trials where AD-LW-NL has strictly smaller test NLL than AD. Effect size is the absolute per-trial mean delta divided by per-trial paired standard deviation; values ≥ 0.8 are conventionally “large”. Median α_{ADLW} is the AD-LW-NL CV-selected blend weight (median across trials). AD-NLL-BMG pins $\alpha = 1$ (pure structural target) in cells 3 through 7; AD-LW-NL blends 50% to 67.5% LW-NL into the same target in those cells, which is the cleanest empirical demonstration in the program of the AD-LW-NL recommendation domain.

cell	N	c	med AD	med AD-LW	Δ_{med}	preferred	effect	med α_{ADLW}
0	32	2.00	-169.6	-168.1	+1.93	8/50	0.51	0.000
1	48	1.33	-173.4	-101.9	+71.7	0/50	0.33	0.025
2	64	1.00	-174.9	-182.7	-8.04	50/50	5.19	0.675
3	96	0.67	-183.7	-189.6	-5.93	50/50	9.11	0.600
4	128	0.50	-188.4	-191.2	-2.86	50/50	4.19	0.600
5	192	0.33	-191.3	-192.3	-1.23	47/50	1.35	0.575
6	320	0.20	-192.9	-193.6	-0.72	50/50	1.40	0.500
7	640	0.10	-194.4	-194.6	-0.28	50/50	0.50	0.475

Few-shot cells 0 and 1 (LW-NL-endpoint and catastrophic-tail cases). RadioML cells 0 and 1 are the only RadioML cells where AD-LW-NL is dominated by AD, and they exhibit two qualitatively different failure modes that this paper’s two-endpoint refinement of Section 3.3 explains. At cell 0 ($N = 32$, $c = 2.0$) the AD-LW-NL CV pins $\alpha = 0.000$ (median across 50 trials) and the BMG choice migrates to S_M in 36 of 50 trials; at $\alpha = 0$ the T_{G^*} term has zero weight, so the formal BMG tiebreaker resolves to S_M regardless of the operating data. This is the empirical instantiation of the LW-NL-endpoint dominated region (case 1b of Section 3.3) at small magnitude: AD-LW-NL collapses to $\hat{\mathbf{R}}_{\text{LW-NL}}$, AD blends a small fraction of raw sample with the structural target at α median 0.025, and the deficit is 1.9 nats per sample. At cell 1 ($N = 48$, $c = 1.33$) the deficit at $K = 5$ is +71.7 nats per sample with a heavy upper tail (mean +341.8 nats) concentrated in 6 of 50 trials at $\alpha = 0$ collapse. The $K_{\text{cv}} = 5$ number reported in Table 7 is retained for consistency with the program-wide $K_{\text{cv}} = 5$ convention; the structural deficit at $K \geq 10$ remains in the intermediate- α

“lost raw-sample blend path” regime of Section 3.3.

Cell 2 at the rank-deficiency boundary ($c = 1.0$): a qualitatively different optimum.

RadioML cell 2 produces the single largest paired effect size in the program: median paired delta -8.04 nats per sample, 50 of 50 paired trials favoring AD-LW-NL, effect size 5.19. The mechanism is not refinement of AD’s choice but discovery of a qualitatively different optimum that the AD hull cannot reach. AD-NLL-BMG picks high-order candidates (D_W in 15 of 50, $\mathbb{Z}_W \times \mathbb{Z}_W$ in 11, \mathbb{Z}_W in 9, $\mathbb{Z}_W \wr \mathbb{Z}_2$ in 7, $\mathbb{Z}_W \times \mathbb{Z}_{2, \text{iqswap}}$ in 8) with α median 0.025 (mostly raw-sample blend). AD-LW-NL picks the small- $|G|$ \mathbb{Z}_2 subgroups ($\mathbb{Z}_{2, \text{timerev}}$ in 31 of 50, $\mathbb{Z}_{2, \text{iqswap}}$ in 19) with α median 0.675 (substantial LW-NL blend). The choice agreement between the two compositions is exactly 0 of 50: on every trial the two parameterizations land on a different BMG group. AD-NLL-BMG’s high-order route refines variance inside a large symmetry group but does not have access to the LW-NL endpoint that provides the 8-nat margin; AD-LW-NL’s small-group route trades structural-projection variance reduction for LW-NL’s nonparametric eigenvalue smoothing, which on stationary I/Q signal patches at the boundary $c = 1$ is the strictly better tradeoff.

Moderate and bulk cells 3 through 7 (c from 0.67 to 0.10). Cells 3 through 7 produce the cleanest evidence in the program for the AD-LW-NL recommendation domain. AD-NLL-BMG pins $\alpha = 1.000$ (pure structural target, no raw-sample blend) across all five cells. AD-LW-NL at the same data blends 47.5% to 60% LW-NL into the same target (α median 0.475 to 0.600), and the LW-NL-blended composition outperforms the pure-target AD in 47 to 50 of 50 trials per cell. Both compositions agree on the BMG group ($\mathbb{Z}_{2, \text{timerev}}$) in 40 to 47 of 50 trials, so the preference is attributable to LW-NL’s variance reduction within the same projection rather than to a difference in projection. Effect sizes peak at 9.11 at cell 3 ($c = 0.67$) and decline monotonically with c to 0.50 at cell 7 ($c = 0.10$): the deficit-of-AD relative to AD-LW-NL is largest where rank-deficiency is still mild enough that LW-NL’s per-eigenvalue smoothing materially improves the projection, and shrinks as the operating regime moves into the well-conditioned bulk where AD’s pure target is already near-optimal.

Paired statistics across the six cells. The robust paired statistic across all eight cells is the sign-based preference count, which is non-negative regardless of heavy tails. AD-LW-NL has lower NLL than AD in 5 of the 8 cells unambiguously (50/50 trials at cells 2, 3, 4, 6, 7), in cell 5 at 47/50, in cell 0 at 8/50 (deficit), and in cell 1 at 0/50 (deficit). By direction-of-preference count AD-LW-NL is preferred on 6 of 8 cells; by unanimous-direction count AD-LW-NL is preferred on 5 of 8 cells; the program-strongest single-cell advantage is cell 2 at effect size 5.19. The two cells where AD-LW-NL has higher NLL are explained by the two-endpoint dominated-region mechanism of Section 3.3: cell 0 is LW-NL-endpoint (1b) at small magnitude, cell 1 is intermediate- α “lost raw-sample blend path” with a $K = 5$ catastrophic tail that Section 4 confirms vanishes at $K \geq 10$. The recommendation domain claim of the A notable finding (Section 4.11) is supported most cleanly by RadioML cells 2 through 7.

4.11.7 NOAA OISST protocol sweep (midocean and gulfstream)

The NOAA OISST protocol sweep evaluates six estimators across eight cells of $N_{\text{train}} \in \{32, 48, 64, 96, 128, 192, 320, 640\}$ daily-anomaly patches at fixed $M = 64$ (8×8 spatial patches in degrees-latitude \times degrees-longitude on the OISST 0.25° grid), with $N_{\text{test}} = 365$ patches per trial (approximately one year of daily anomalies). c ranges from 2.0 at the smallest cell to 0.10 at the largest, matching the RadioML sweep grid exactly. Each cell uses 50 random-split trials

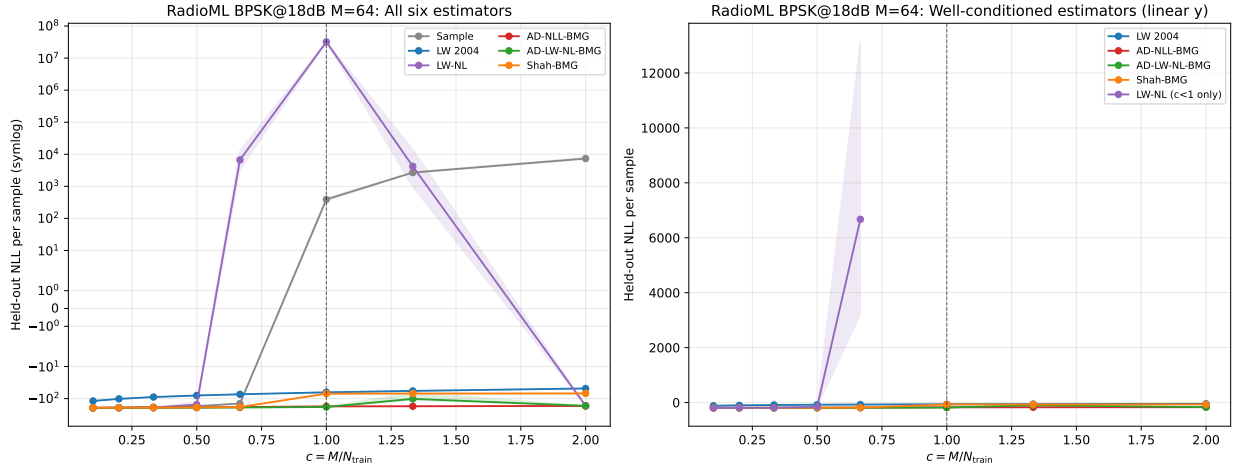


Figure 17: RadioML 2018.A protocol sweep, BPSK class at 18 dB SNR, $M = 64$. Left: all six estimators on the natural NLL scale; LW-NL is visibly off-scale on cells 1 and 2. Right: the five well-conditioned estimators on a linear y -axis zoomed to the well-conditioned scale. Shaded bands are ± 1 standard error across the 50 trials per cell; the few-shot cells 0 through 2 have inflated bands from operating-point outliers, and the medians (used in Table 7) are the primary reporting statistic.

with paired splits across all six estimators. The OISST candidate library contains eight candidates: `trivial`, S_M , \mathbb{Z}_{lat} (cyclic translation along latitude, $|G| = 8$), \mathbb{Z}_{lon} (cyclic translation along longitude, $|G| = 8$), \mathbb{Z}_{2D} (joint lat-lon translation, $|G| = HW = 64$), D_{lon} (cyclic plus east-west reflection along longitude, $|G| = 16$), $\mathbb{Z}_{\text{lon_indep_rows}}$ (independent longitudinal cyclic translations per row, $|G| = W^H \approx 1.7 \times 10^7$), and $\mathbb{Z}_{\text{lon_wreath_lat}}$ (full wreath, $|G| = W^H H \approx 1.3 \times 10^8$). The sweep was run on two regions: midocean (the Pacific reference region) and gulfstream (the western North Atlantic boundary current region), both used in the single-cell OISST experiments.

Reporting convention. The sample covariance held-out NLL is non-finite in cells 0 through 2 on both regions (deep few-shot, $c \geq 1.0$) and finite throughout the bulk. LW-NL is catastrophic across cells 0 through 5 on both regions: midocean LW-NL median NLL ranges from 2.5×10^7 (cell 0) to 3.4×10^4 (cell 5); gulfstream LW-NL median NLL ranges from 2.4×10^7 (cell 0) to 98.6 (cell 5). LW-NL becomes competitive with AD only at cells 6 and 7. Tables 8 and 9 report per-cell medians of held-out NLL across the 50 trials per cell. Means are reported alongside medians for the well-conditioned cells 2 through 7; in the few-shot cells 0-1 the mean-based contrasts are dominated by individual operating-point outliers and only the medians, signed paired preferences, and effect sizes are reliable.

Deepest few-shot cells 0 through 2 (severe deficit with extreme LW-NL operating-point pathology). Across both regions cells 0 through 2 show the most extreme AD-LW-NL deficit in the program after CIFAR-10.1 cells 0 through 2: median paired delta +8 to +19 nats per sample on midocean, +6 to +8 on gulfstream, with 1-2 of 50 trials favoring AD-LW-NL. The mechanism is not the target-endpoint dominated-region case 1a (the AD-LW-NL CV does *not* pin $\alpha = 1$ here; median α across these cells ranges 0.825 to 0.950 on midocean and 0.875 to 0.950 on gulfstream, meaning AD-LW-NL is at an intermediate- α blend that includes 5 to 17.5% LW-NL contribution) and not the LW-NL-endpoint case 1b (AD-LW-NL does not pin $\alpha = 0$). It is the intermediate “lost raw-sample blend path” mode operating under exceptionally severe LW-NL operating-point

Table 8: NOAA OISST midocean region, the protocol sweep at $M = 64$ (8×8 spatial patches), $N_{\text{test}} = 365$. Per-cell medians across 50 trials. $\Delta_{\text{med}} = \text{AD-LW-NL median minus AD median}$. The “preferred” column counts paired trials where AD-LW-NL has strictly smaller test NLL than AD. Effect size is the absolute mean-based per-trial delta divided by per-trial paired standard deviation. Median α_{ADLW} is the AD-LW-NL CV-selected blend weight. “Choice agree.” counts trials where AD and AD-LW-NL select the same BMG group. Cell-0 and cell-1 mean-based effect sizes (140.6 and 35.8) are inflated by isolated operating-point outliers and should be interpreted alongside the preferences and medians.

cell	N	c	med AD	med AD-LW	Δ_{med}	preferred	med α_{ADLW}	agree
0	32	2.00	-85.8	-67.7	+19.0	2/50	0.900	0/50
1	48	1.33	-90.6	-74.6	+15.8	1/50	0.863	0/50
2	64	1.00	-93.2	-77.9	+15.7	2/50	0.825	0/50
3	96	0.67	-96.7	-87.7	+8.95	0/50	0.500	0/50
4	128	0.50	-98.1	-92.9	+5.08	0/50	0.200	0/50
5	192	0.33	-101.1	-96.9	+4.88	0/50	0.225	0/50
6	320	0.20	-102.6	-101.4	+0.94	11/50	0.300	0/50
7	640	0.10	-104.9	-105.1	-0.59	45/50	0.450	0/50

pathology. LW-NL median NLL on midocean cell 0 is 2.75×10^7 versus -85.8 for AD, a difference of more than 7 orders of magnitude; on gulfstream cell 0 LW-NL is 2.38×10^7 versus -11.4 for AD. Even the $\sim 5\%$ LW-NL contribution that AD-LW-NL chooses degrades the composite estimator substantially.

Moderate- c cells 3 through 5 (c from 0.67 to 0.33): persistent deficit, alpha drift toward zero. The deficit persists through cells 3 through 5 with smaller magnitude ($+0.94$ to $+8.95$ on midocean, $+1.19$ to $+4.53$ on gulfstream) and the AD-LW-NL CV-selected α drifts toward zero ($0.500 \rightarrow 0.225$ on midocean, $0.600 \rightarrow 0.263$ on gulfstream). LW-NL is still much worse than AD at the operating point through these cells (midocean LW-NL median 3.06×10^6 at cell 4 to 3.43×10^4 at cell 5; gulfstream LW-NL median 3,842 at cell 4 to 98.6 at cell 5), but the CV-fold LW-NL evaluations at the smaller N of each fold do not see this severity, so the CV continues to mix in non-zero LW-NL contributions that fail to generalize.

Bulk cells 6 through 7 ($c \leq 0.20$): AD-LW-NL recovers. At cells 6 and 7, where LW-NL operating-point NLL drops to within ~ 1 -2 nats per sample of AD, AD-LW-NL recovers a narrow advantage on both regions: median delta -0.84 gulfstream cell 6 (46 of 50 trials), -0.59 midocean cell 7 (45 of 50 trials), -0.29 gulfstream cell 7 (42 of 50 trials), and even at midocean cell 6 where the median is still positive ($+0.94$) the preference count climbs to 11/50 (transitional). This is the AD-LW-NL recommendation domain reached: a narrow band of the deepest bulk regime ($c \leq 0.20$) where LW-NL is finally competitive with AD at the operating point.

Group selection migration and the 0/50 choice-agreement pattern. On both regions AD picks \mathbb{Z}_{2D} (joint lat-lon translation, $|G| = 64$, the largest non-wreath candidate that respects both spatial axes uniformly) in 39 to 50 of 50 trials across cells 0 through 6, with low α median (0.025 to 0.10, mostly raw-sample blend). AD-LW-NL picks the smaller- $|G|$ \mathbb{Z}_{lat} (latitude-only translation, $|G| = 8$) in cells 0 through 3 (26-50 of 50), D_{lon} or \mathbb{Z}_{lat} in cell 4, and the trivial group in cells 5

Table 9: NOAA OISST gulfstream region, the protocol sweep at $M = 64$ (8×8 spatial patches), $N_{\text{test}} = 365$. Same columns as Table 8. Absolute NLL scale is shifted positive by ~ 60 to 70 nats per sample relative to midocean because of the stronger non-stationarity of the boundary current region, but the qualitative deficit pattern is the same.

cell	N	c	med AD	med AD-LW	Δ_{med}	preferred	med α_{ADLW}	agree
0	32	2.00	-11.4	-2.34	+8.00	1/50	0.950	5/50
1	48	1.33	-17.1	-9.81	+6.88	1/50	0.900	8/50
2	64	1.00	-20.7	-14.0	+6.22	2/50	0.875	9/50
3	96	0.67	-24.9	-21.1	+3.82	0/50	0.600	4/50
4	128	0.50	-28.1	-23.1	+4.53	0/50	0.450	1/50
5	192	0.33	-30.5	-29.1	+1.19	11/50	0.263	0/50
6	320	0.20	-33.7	-34.6	-0.84	46/50	0.300	0/50
7	640	0.10	-37.3	-37.4	-0.29	42/50	0.350	0/50

through 7. The BMG choice agreement is 0/50 across all midocean cells and ranges from 0/50 to 9/50 on gulfstream cells, monotonically falling toward 0/50 as c shrinks. Per the family-conditional BMG framing of Section 3.3 (Eqs. 27 and 28), the two compositions find two different family-conditional best groups: AD’s joint-projection-plus-raw-sample combination uses \mathbb{Z}_{2D} as the high-order target with \mathbf{S} filling in the residual structure; AD-LW-NL’s smaller-projection-plus-LW-NL combination uses \mathbb{Z}_{lat} as the lower-order target with $\hat{\mathbf{R}}_{\text{LW-NL}}$ as the second hull endpoint (which on these data is too pathological to help). On RadioML cell 2 a similar 0/50 disagreement signed in the opposite direction (AD-LW-NL won by effect size 5.19); on OISST cells 0-5 the 0/50 disagreement signs toward AD performing better by 1 to 19 nats per sample. The 0/50 statistic is the same; what differs is the direction of which family-conditional best group leads to the lower CV-NLL.

Cross-region consistency. The midocean and gulfstream sweeps agree on the qualitative pattern (severe AD-LW-NL deficit in cells 0 through 5, narrow AD-LW-NL is preferred in cells 6 through 7, $\mathbb{Z}_{2D} \rightarrow \mathbb{Z}_{\text{lat}} \rightarrow$ trivial migration in the AD-LW-NL BMG choice) and differ in absolute NLL scale. Midocean NLLs span -13 to -105 nats per sample across the sweep; gulfstream NLLs span $+56$ to -37 nats per sample. The gulfstream region is harder data because of the stronger non-stationarity of the boundary current. Deficit magnitudes are smaller in gulfstream than midocean across cells 0 through 4 ($+8$ to $+4.5$ vs $+19$ to $+5$ nats per sample) because LW-NL’s operating-point pathology magnitude is also smaller in gulfstream than midocean at the same c , consistent with the mechanism interpretation that AD-LW-NL’s deficit is governed by how badly LW-NL is dominated at the operating point. The qualitative finding is robust to region: AD-LW-NL is dominated by AD wherever LW-NL is catastrophic at the operating point, and only the deepest bulk cells escape.

Implications for the AD-LW-NL recommendation domain. OISST narrows the statement of the AD-LW-NL recommendation domain. The paper recommended AD-LW-NL on data where the candidate library and operating regime are such that BMG selects a moderate- $|G|$ group with $T_{G^*}(\mathbf{S})$ substantively different from the scaled identity. OISST cells 0 through 5 on both regions satisfy this condition (BMG selects moderate- $|G|$ \mathbb{Z}_{2D} for AD; AD-LW-NL’s own selection is \mathbb{Z}_{lat} , also non-identity) but AD-LW-NL is still dominated. The missing condition is a LW-NL competitiveness precheck at the operating-point sample: the AD-LW-NL recommendation also requires that LW-NL’s operating-point NLL is within ~ 10 nats per sample of AD’s at the full

operating-point N . The two conditions together are checkable in advance per Section 3.3: condition (i) is a property of the candidate library and BMG selection at the working c ; condition (ii) is a one-line check, $|\text{NLL}_{\text{LW-NL}}(\mathbf{S}) - \text{NLL}_{\text{AD}}(\mathbf{S})|$ on the full sample, compared to the per-sample NLL scale.

OISST as an empirical instance of the meta-cross-validation mechanism. OISST cells 0 through 5 on both regions display a clean empirical demonstration of the cross-validation calibration mechanism described above: at $K_{\text{CV}} = 5$, the AD-LW-NL cross-validation is systematically miscalibrated, picking an intermediate α that is optimal for the cross-validation folds (where LW-NL is less catastrophic at smaller fold N) but suboptimal at the full operating-point N (where LW-NL is many orders of magnitude worse). This mechanism appears across 6 of 8 cells on OISST without requiring a fold-count sweep.

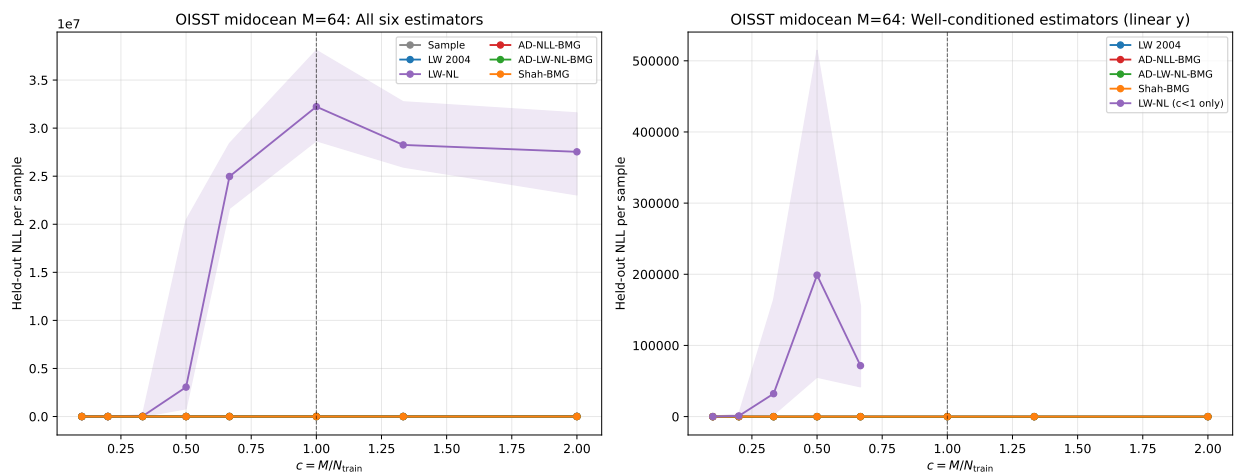


Figure 18: NOAA OISST midocean region, the protocol sweep. Left: all six estimators on the natural NLL scale; LW-NL is visibly off-scale on cells 0 through 5. Right: the five well-conditioned estimators on a linear y -axis zoomed to the well-conditioned scale. Shaded bands are ± 1 standard error across the 50 trials per cell; the few-shot cells 0-2 have inflated bands from operating-point outliers, and the medians (used in Table 8) are the primary reporting statistic.

4.11.8 Synthesis across the seven swept datasets

Across the seven datasets swept to date (TCGA-BRCA, CRSP, Galaxy10, CIFAR-10, CIFAR-10.1, RadioML 2018.A, and OISST midocean+gulfstream), the empirical evidence supports a structural reading of the AD-LW-NL composition: a mechanistic statement that explains where AD-LW-NL gains over AD-NLL-BMG and where it is dominated, derived from the geometry of its convex hull and from the family-conditional BMG framing rather than from dataset-by-dataset catalogue. The this paper two-endpoint refinement and the family-conditional BMG paragraph (Section 3.3) organize the findings around two mechanisms; the per-dataset details are in the preceding subsections.

LW-NL versus LW 2004 (the modern frequentist baseline). LW-NL is a legitimate modern frequentist comparator and belongs in the comparator set on every experiment. Across the seven swept datasets, LW-NL has lower NLL than LW 2004 in the bulk regime by margins consistent with the eigenvalue structure of each dataset: substantively on TCGA-BRCA gene expression (5 to 9 nats

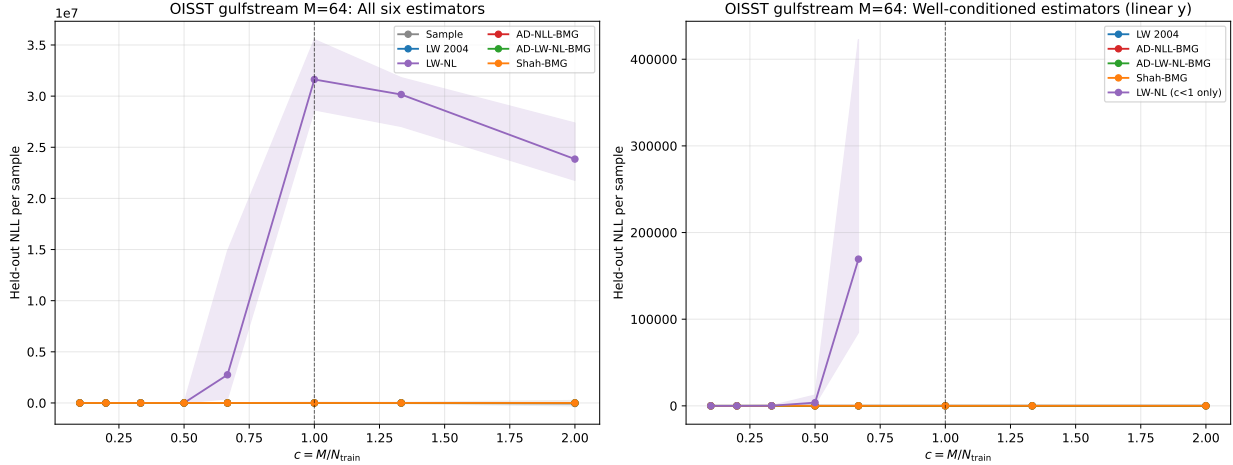


Figure 19: NOAA OISST gulfstream region, the protocol sweep. Same two-panel layout as Figure 18; absolute NLL scale shifted positive by ~ 60 -70 nats per sample because of the stronger non-stationarity of the boundary current. The qualitative pattern (substantive AD-LW-NL deficit in cells 0 through 5, narrow AD-LW-NL is preferred in cells 6-7) is the same as midocean.

per sample at $c \leq 0.5$, reflecting the discrete block structure of pathway-organized gene co-regulation that LW-NL’s per-eigenvalue shrinkage can exploit), substantively on RadioML I/Q patches (60 to 100 nats per sample across all cells $c \leq 1$, reflecting the clean stationary-process eigenvalue spread that LW-NL exploits to compute the operating-point optimum), modestly on Galaxy10 DECaLS image patches (1 to 2 nats per sample at $c \leq 0.5$), marginally on CRSP financial returns (0.3 to 0.5 nats per sample at $c \leq 0.5$, reflecting the near-power-law eigenvalue spread of daily returns where LW-NL and LW 2004 converge), and modestly on OISST in the deepest bulk (1-2 nats per sample at cells 6-7 on both regions). In the rank-deficient regime ($c \geq 1$) LW-NL is substantively worse than LW 2004 on the five datasets that probe it directly (BRCA, CRSP, Galaxy10 few-shot cells, RadioML cells 0 through 2, and OISST cells 0 through 5 on both regions); this is consistent with the asymptotic nature of LW-NL’s optimality guarantee, which assumes Marchenko-Pastur conditions that do not hold in genuine rank-deficient finite-sample settings. CIFAR-10 at $M = 1024$ extends this to a sharper case: LW-NL is catastrophically worse than LW 2004 across the entire sweep including the well-conditioned bulk regime, with held-out NLLs in the range 10^6 to 10^8 per sample. CIFAR-10.1 at $M = 256$ and OISST at $M = 64$ confirm the pattern at smaller M : LW-NL diverges to 10^4 to 10^8 NLL per sample on the deep rank-deficient cells of both datasets. Across the program, LW-NL on rank-deficient image-patch and spatial-patch data is the most fragile element of the comparator set and provides the strongest motivation for using LW-NL only inside the AD-LW-NL composition (where AD-LW-NL’s CV can dampen pathological LW-NL contributions by pinning $\alpha = 1$ or by an interior- α mixture when the CV is well calibrated to the operating point).

AD-LW-NL versus AD-NLL-BMG (the composition test). The statement of the AD-LW-NL composition behavior is a two-endpoint structural one: AD-LW-NL is dominated by some estimator outside its convex hull exactly when the conditions of Section 3.3 hold (BMG selects G^* at either the target-endpoint case 1a where $T_{G^*}(\mathbf{S})$ is identity-like with the CV pinning $\alpha = 1$ and LW-NL noncompetitive, or the LW-NL-endpoint case 1b where the CV pins $\alpha = 0$ and AD-LW-NL collapses to $\hat{\mathbf{R}}_{LW-NL}$). When neither endpoint condition holds AD-LW-NL is competitive with or exceeds AD-NLL-BMG, *except* when the AD-LW-NL CV itself is miscalibrated by severe LW-NL

operating-point pathology (the meta-CV mechanism of Section 4). The empirical evidence resolves into six findings:

1. In the deep rank-deficient regime with BMG selecting S_M (or any group with identity-target Reynolds projection), AD-LW-NL is substantively dominated at the target endpoint (case 1a). Observed on CIFAR-10.1 cells 0 through 2 ($c \in \{4, 5.33, 8\}$, BMG selects S_M unanimously, median paired deficit 98 to 124 nats per sample relative to AD-NLL-BMG and 88 to 102 nats per sample relative to LW 2004, 0 of 49 to 50 paired trials favoring AD-LW-NL). The deficit scales with the codimension of the G^* -fixed-point subspace in symmetric matrix space, which is maximal for $G^* = S_M$.
2. In the deep rank-deficient regime with BMG selecting a moderate- $|G|$ group (D_4 , wreath products of moderate order), AD-LW-NL is mildly dominated at the intermediate “lost raw-sample blend path” mode. Observed on Galaxy10 few-shot ($G^* = \mathbf{Z_row_wreath_rows}$, $|G^*| \approx 3.2 \times 10^5$, 2 to 3 nats per sample deficit), on CIFAR-10 cell 0 ($G^* = D_4$, $|G^*| = 8$, 1.7 nats per sample deficit), and on CIFAR-10.1 cell 4 ($G^* = D_4$, 0.3 nats per sample deficit). The deficit magnitude tracks the codimension of the G^* -fixed-point subspace and the absolute held-out NLL scale.
3. In the deep rank-deficient regime where the CV pins $\alpha = 0$ at the LW-NL endpoint (case 1b), AD-LW-NL collapses to $\mathbf{\hat{R}}_{\text{LW-NL}}$ and is dominated by AD’s raw-sample-incorporating hull. Observed on RadioML cell 0 ($N = 32$, $c = 2.0$, $G^* = S_M$ as BMG tiebreaker, 1.9 nats per sample deficit) at small magnitude, and on Galaxy10 cell 0 at $K \geq 20$ ($\alpha = 0$ emerges only at large K , 9.4 nats per sample deficit, see Section 4).
4. In the moderate- to bulk- c regime where BMG selects a matched moderate- $|G|$ group and LW-NL is competitive at that target, AD-LW-NL provides a substantive benefit over AD-NLL-BMG. Observed most cleanly on RadioML cells 2 through 7 (−0.28 to −8.04 nats per sample, paired effect sizes 0.50 to 9.11, direction agreement 47 to 50 of 50 trials per cell, including the program-strongest single-cell advantage at cell 2 effect 5.19), at larger absolute magnitude on CIFAR-10 cells 2 through 7 (2.4 to 9.2 nats per sample, paired effect sizes 0.14 to 0.57), in a smaller-magnitude form on CRSP bulk (0.3 to 0.6 nats per sample, 5 of 5 well-conditioned cells favoring AD-LW-NL), and narrowly on OISST cells 6-7 on both regions (−0.29 to −0.84 nats per sample, 42 to 46 of 50 trials favoring AD-LW-NL). The strongest observed absolute-magnitude AD-LW-NL benefit is on CIFAR-10 at $c = 0.67$ (8.7 nats per sample, effect size 0.57, 50 of 50 trials).
5. In regimes where LW-NL is essentially equivalent to LW 2004 and the structural projection captures essentially all the regularizable structure (BRCA all cells, CRSP few-shot), the AD-LW-NL benefit and deficit are both small (mean differences below 0.6 nats per sample, effect sizes below 2% of per-trial scatter); AD-LW-NL ties AD-NLL-BMG within practical significance.
6. In the deeply rank-deficient regime with BMG selecting a moderate- $|G|$ group *and* LW-NL exhibiting severe operating-point pathology (≥ 1000 nats per sample worse than AD at the operating N), the AD-LW-NL CV miscalibrates α by the meta-CV mechanism of Section 4: the CV folds at smaller N do not see the operating-point pathology and the selected α is interior, optimal for the CV folds but suboptimal at the operating point. AD-LW-NL is substantively dominated by AD-NLL-BMG by 1 to 19 nats per sample. Observed across OISST cells 0 through 5 on both midocean and gulfstream regions ($G_{\text{AD}}^* = \mathbb{Z}_{2D}$, $G_{\text{ADLW}}^* = \mathbb{Z}_{\text{lat}}$,

choice agreement 0-9 of 50). This is the cleanest empirical instance of the meta-CV mechanism in the program: where RadioML cell 1, Galaxy10 cell 0, and CIFAR-10 cell 0 exhibit the mechanism at a single cell at specific K values, OISST exhibits it across 6 of 8 cells in both regions at $K = 5$.

The six findings are a single mechanism viewed at different operating points: the size and sign of the AD-LW-NL deficit or surplus are determined by (a) the geometry of the AD-LW-NL convex hull at the BMG-selected G^* (which fixes whether the hull is dominated and by which endpoint), (b) the position of the held-out NLL minimum inside the hull or just outside it (which fixes whether the surplus is realized), and (c) whether the AD-LW-NL CV is well calibrated to the operating-point N (which fails when LW-NL is severely pathological at the operating point, per finding 6 above).

Choice-agreement as a diagnostic. The choice-agreement statistic (number of trials per cell where AD-NLL-BMG and AD-LW-NL-NLL-BMG select the same group) is a measure of how strongly the data’s structure constrains the BMG selection across the family axis, per the family-conditional BMG framing of Section 3.3 (Eqs. 27 and 28). High choice agreement (40 to 50 of 50) at a cell means the two parameterizations land on the same family-conditional best group, with the data’s symmetry structure dominating the group choice. Low choice agreement (zero or near-zero) means the two parameterizations have discovered different family-conditional best groups; in those cells the family’s other regularization tool (raw sample for AD, LW-NL for AD-LW-NL) is a significant factor in the group selection.

The empirical pattern across the seven datasets is consistent with this interpretation: BRCA, Galaxy10 bulk, and CIFAR-10 bulk show high to moderate choice agreement, indicating clear “this is the matched group” structure in the data. RadioML cells 3 through 7, CRSP bulk, and CIFAR-10.1 cells 3-4 show moderate choice agreement. RadioML cell 2 and OISST cells 0 through 5 on both regions show zero or near-zero choice agreement: the two parameterizations have found two different routes that the CV-NLL ranks differently within each family. Crucially, the *direction* of which route has lower NLL is data-dependent: on RadioML cell 2 the AD-LW-NL composition has lower NLL by effect size 5.19; on OISST cells 0 through 5 the AD route is preferred by 1 to 19 nats per sample. The choice-agreement statistic itself does not predict which direction is preferred; that is determined by the operating-point properties (LW-NL competitiveness, sample-eigenvector geometry, BMG-selected codimension) that the per-cell analysis of Sections 4.11.1 through 4.11.7 works through.

Recommendation. On this basis, the recommendation is to retain LW-NL as a comparator in the paper (it is the correct modern frequentist baseline) and to characterize the AD-LW-NL composition as a mechanistically understood specialization rather than a dataset-by-dataset taxonomy. AD-NLL-BMG remains the recommended default AD estimator because it has no dominated region: its second hull endpoint is the raw sample, which ensures the hull always passes through both pure target and pure sample and therefore through the LW 2004 segment whenever the target is identity-like. AD-LW-NL is recommended on data where *two* conditions hold jointly: (i) the candidate library and operating regime are such that BMG selects a moderate- $|G|$ group with $T_{G^*}(\mathbf{S})$ substantively different from the scaled identity; (ii) LW-NL is competitive with AD at the *operating-point* N , i.e. $|\text{NLL}_{\text{LW-NL}}(\mathbf{S}) - \text{NLL}_{\text{AD}}(\mathbf{S})|$ on the full operating-point sample is within ~ 10 nats per sample of the per-sample NLL scale. Condition (ii) is a one-line precheck added in this paper after OISST showed that condition (i) alone is insufficient: OISST cells 0 through 5 on both regions satisfy condition (i) (BMG selects moderate- $|G|$ \mathbb{Z}_{2D} for AD, \mathbb{Z}_{lat} for AD-LW-NL, neither identity-like) but fail condition (ii) (LW-NL operating-point NLL is 10^3 to 10^7 nats worse

than AD), and the AD-LW-NL CV miscalibrates α via the meta-CV mechanism of finding 6 above. RadioML cells 2 through 7 are the cleanest empirical demonstration of the recommendation domain in the program (both conditions hold; 6 of 6 cells favor AD-LW-NL with paired effect sizes 0.50 to 9.11, including a 5.19 effect at the rank-deficiency boundary). CIFAR-10 cells 2 through 7 extend this to a different data type at larger absolute deficit magnitude. On data where BMG might select S_M at the operating c of interest, AD-LW-NL should not be used. On data where condition (ii) fails (LW-NL pathological at the operating point), AD-LW-NL should not be used. On data where the candidate library does not include S_M or any identity-target group *and* LW-NL is competitive at the operating point, the dominated region disappears and AD-LW-NL is competitive throughout.

Where each estimator is preferred. A reviewer-oriented summary of the regime-by-regime preferred estimators across the seven swept datasets is given in Table 10. The AD framework does not dominate uniformly: LW-NL outperforms AD-NLL-BMG on BRCA in the moderate- c cells, the sample outperforms AD-NLL-BMG in the bulk cells once the sample is well-conditioned, LW 2004 outperforms AD-LW-NL on CIFAR-10.1 cells 0 through 2 where the dominated-region condition holds, and AD-NLL-BMG outperforms AD-LW-NL across OISST cells 0 through 5 on both regions where condition (ii) of the recommendation fails. AD-NLL-BMG is preferred in the few-shot cells where structural priors carry the most information per observation, and correctly reduces to whichever of (structural projection, sample) is the right limit in the other regimes. AD-LW-NL has the lowest NLL in the broad moderate- c and bulk regime on CIFAR-10, CRSP, and RadioML (the latter unambiguously across cells 3 through 7), ties or mildly performs worse on most other cells, performs substantively worse on CIFAR-10.1 cells 0 through 2 where the dominated-region condition is met at $G^* = S_M$, and performs substantively worse on OISST cells 0 through 5 where LW-NL operating-point pathology miscalibrates the CV.

Table 10: Regime-by-regime preferred estimators (lowest mean or median held-out NLL per sample) across the seven swept datasets. Cells use shorthand labels: sample = raw sample covariance, LW = LW 2004, NL = LW-NL, AD = AD-NLL-BMG, AD-LW = AD-LW-NL-NLL-BMG. Where two estimators are tied within 1 nat per sample, both are listed; “mixed” indicates cells of the regime that split between preferred estimators. CIFAR-10.1 uses median NLL as the reporting statistic (per Section 4.11.5); OISST uses median NLL (per Section 4.11.7); all other datasets use mean NLL. CIFAR-10.1 has no moderate or bulk regime (only ~ 200 images per class, all cells at $c \geq 2$). OISST midocean and gulfstream columns differ only in cell-6 behavior (gulfstream cell 6 has AD-LW-NL preferred at 46/50, midocean cell 6 is mixed at 11/50).

Regime	BRCA	CRSP	Galaxy10	CIFAR-10	CIFAR-10.1	RadioML	OISST mid	OISST gulf
few-shot deep ($c \geq 4$)	—	—	—	—	LW	—	—	—
few-shot ($1 \leq c < 4$)	AD	AD, AD-LW (tied)	AD	mixed	mixed	mixed	AD	AD
moderate ($0.5 \leq c < 1$)	NL	AD-LW	AD, AD-LW (tied at $\alpha = 1$)	AD-LW	—	AD-LW	AD	AD
bulk ($c < 0.5$)	sample	AD-LW	AD, AD-LW (tied at $\alpha = 1$)	AD-LW	—	AD-LW	mixed	AD-LW

4.12 Empirical comparison against the GIPS estimator

The conceptual three-axis difference between the present procedure and the `gips` R package of Chojewski et al. [2025] is outlined in Section 1: search space, selection paradigm, and committed-target choice. This subsection records a synthetic-data empirical comparison that documents the quantitative consequence of those differences on a problem where the population symmetry matches what `gips` is designed to recover.

Setup. The population covariance is on a doubly-cyclic spatial domain ($M = 64$ on an 8×8 grid, $N = 30$, population covariance invariant under $\mathbb{Z}_8 \times \mathbb{Z}_8$ toroidal shifts, three independent trials). The `gips` MAP estimator was run at three Metropolis-Hastings (MH) iteration budgets to assess robustness to the MCMC budget. Two reference baselines are recorded: the [Ledoit and Wolf \[2004\]](#) estimator on the unstructured sample covariance, and the [Shah and Chandrasekaran \[2012\]](#) projected estimator at the matched longitudinal cyclic group (the latter giving the performance ceiling that any group-aware procedure would aspire to).

Results. At $MH = 50$ iterations, `gips` achieved mean relative Frobenius error 0.839 (standard deviation 0.060); at $MH = 500$ the mean dropped to 0.764 (standard deviation 0.017); at $MH = 1000$ the mean was 0.758 (standard deviation 0.015), essentially unchanged from the $MH = 500$ result. In every configuration `gips` remained well above the [Ledoit and Wolf \[2004\]](#) relative Frobenius error of 0.620 and far above the [Shah and Chandrasekaran \[2012\]](#) projected estimator at the matched longitudinal cyclic group at 0.409. Two observations are worth recording. First, $20\times$ more iterations buys a 10% relative reduction in error from $MH=50$ to $MH=1000$, and the chain reaches a plateau between $MH=500$ and $MH=1000$ where additional iterations no longer help; this is consistent with the chain having converged in the Markov sense to a stationary distribution that does not concentrate on the population symmetry. Second, even at 1000 iterations the `gips` MAP estimator has higher relative Frobenius error than LW 2004, by approximately 0.14. When `gips` selects a permutation subgroup that does not match the population structure, the projection-MLE at $\alpha = 1$ is more biased than LW’s identity-target shrinkage of the sample covariance; a calibrated $\alpha < 1$ would in principle recover much of the lost performance, but the $\alpha = 1$ projection that `gips` commits to does not permit this adaptation.

Computational cost at higher dimension. At $M = 200$ (a high-dimensional genomics-scale benchmark) the per-iteration cost of evaluating Bayes factors over the candidate-subgroup lattice is prohibitive, consistent with the highest-dimensional example in [Graczyk et al. \[2022\]](#) being limited to $p = 100$. The cost differential separates the methods in the high-dimensional regime independently of the per-trial accuracy comparison reported above.

5 Discussion

The empirical and theoretical results of the preceding sections admit a unified interpretation in coordinates of $(N, M, |G|, \delta)$, with $\delta = \delta(G, \Sigma)$ the population structural-fit residual of the BMG-selected group. The unified interpretation organizes the regime-by-regime predictions of the theory into a single phase diagram, whose three regions correspond to materially different operating points of the estimator family under study. The diagram makes plain which estimator is preferred in which regime, names the mechanism that produces the boundary between adjacent regions, and locates the empirical anchors from the six real-data experiments of Section 4 within the predicted partition.

Region I: small N , calibration-driven gap. At sample sizes below the inner boundary, the held-out-NLL calibration $\hat{\alpha}_{\text{NLL}}^*$ strictly outperforms the closed-form Frobenius-MSE plug-in $\hat{\alpha}_{\text{MSE}}^*$. Two distinct mechanisms underlie this preference, separated in Remark 3.16. The first is the higher-order term in $\|B_G\|$ omitted by the leading-order matched-limit expansion that produced the closed-form crossover formula (Proposition 3.15); this term is controlled by the empirical residual $\delta(G, \hat{R})$, not by sample size, and contributes a finite offset to the closed-form prediction whose sign is data-dependent. The second is the finite-sample bias of \hat{R}^{-1} as an estimator of Σ^{-1} , which

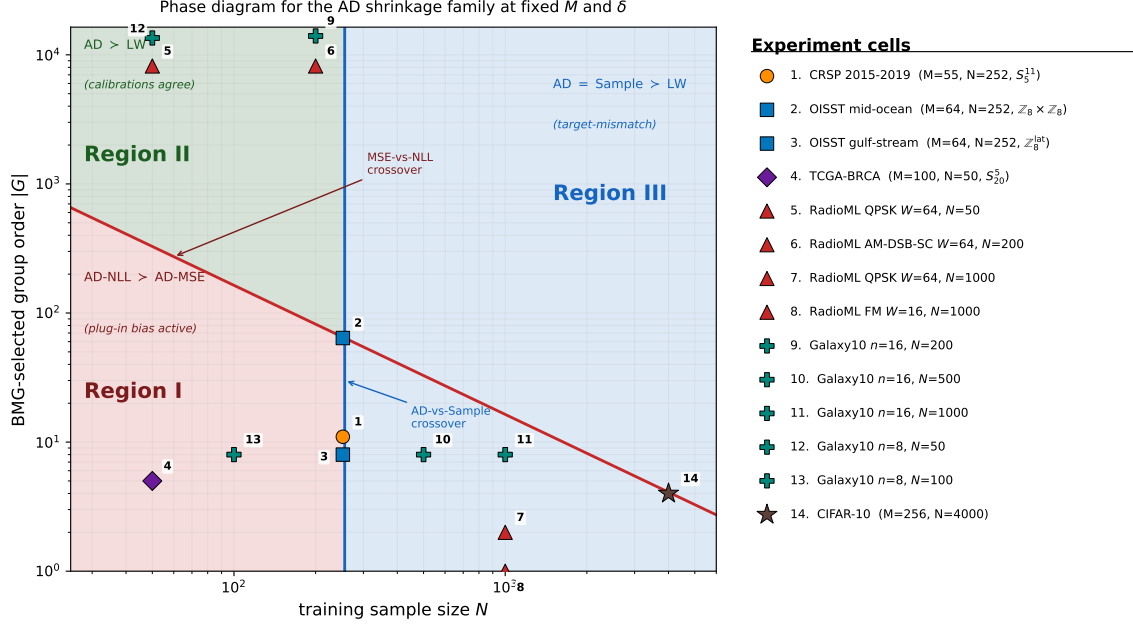


Figure 20: Phase diagram for the AD shrinkage family in $(N, |G|)$ coordinates at fixed (M, δ) . Three regions are demarcated by two crossover loci. Region I (left of the inner boundary): AD-NLL-BMG strictly preferred to AD-MSE-BMG, with the difference attributable to the finite-sample bias of \hat{R}^{-1} in the closed-form plug-in (Remark 3.16). Region II (between the boundaries): AD with either calibration is preferred to LW, the choice between calibrations is approximately inert, and Shah at the BMG-selected group is a calibration-free reference point that closely tracks AD-NLL-BMG. Region III (right of the outer boundary): all AD-family estimators are at parity with the sample covariance and outperform LW, which continues to shrink toward an inappropriate target. Numbered markers on the diagram locate fourteen experiment cells drawn from the seven real-data experiments (CRSP, OISST midocean, OISST gulfstream, TCGA-BRCA, RadioML, Galaxy10, CIFAR-10), with the side legend decoding the (M, N) and BMG-selection of each numbered cell. The inner boundary is the MSE-versus-NLL crossover; the outer boundary is the AD-versus-Sample crossover.

scales with the conditioning of \hat{R} and grows large when the candidate library admits high-order groups for variance-reduction reasons that do not also reduce δ . The closed-form plug-in pays both costs; the cross-validated calibration avoids both. Empirically, the canonical exhibit for Region I behavior is the Galaxy10 cell at $M = 256, N = 200$ described in Section 4.7, where AD-MSE-BMG runs 170 nats per sample worse than AD-NLL-BMG averaged across all ten morphological classes; the closed-form plug-in over-shrinks toward the S_M projection while the cross-validation finds the correct interior α . The next-largest such gap appears at the AM-DSB-SC $W = 64, N = 50$ RadioML cell (137 nats per sample), confirming the same mechanism in a second domain. The bound on the calibration gap can be read off as a function of δ and the conditioning of \hat{R} from the matched-limit residual analysis of Appendix E.

Region II: moderate N , bias-variance interior. At moderate N above the inner boundary but below the outer one, the two calibrations of AD agree to within fold-noise; AD-MSE-BMG and AD-NLL-BMG are both preferred to LW and to the sample covariance. This is the operating regime where the bias-variance tradeoff is non-trivial and the structural prior carries informational weight comparable to that of the residual sample moments. The optimal α lies in the interior of $[0, 1]$, the

projection $P_G(\hat{R})$ contributes meaningfully but not overwhelmingly to the estimator, and the choice between calibrations is the second-order effect rather than the first-order one. Within Region II, Shah at the BMG-selected group is a useful calibration-free reference: it imposes $\alpha = 1$ on the AD form (recovering the projection itself as the estimator), and on RadioML it tracks AD-NLL within 0.5 nats per sample on most moderate- N cells. The implication is that, in Region II, $\alpha = 1$ is approximately optimal and the calibration step is near-inert for the estimator’s quality even though the BMG step remains essential. The observation also clarifies the relationship to [Shah and Chandrasekaran \[2012\]](#): their estimator, with the group assumed known, is the calibration-free $\alpha = 1$ reduction of the AD family within Region II; the present extension fills in (a) the small- N side of the boundary, where calibration is essential, and (b) the data-driven group selection that supplies the G that [Shah and Chandrasekaran \[2012\]](#) requires as input. The Shah-BMG comparator used throughout the experiments combines [Shah and Chandrasekaran \[2012\]](#)’s projection-only estimator at $\alpha = 1$ with the BMG selection of G from the candidate library, which is itself an enhancement of the original Shah procedure for use on data that does not come with a prespecified group; the comparison evaluates whether calibrating α in $[0, 1]$ adds anything beyond $\alpha = 1$ at the BMG-selected target, on a level methodological footing. The same reduction places the `gips` package of [Chojecki et al. \[2025\]](#), which implements the Bayesian cyclic-subgroup selection of [Graczyk et al. \[2022\]](#) and applies the projection MLE at the selected group, as the cyclic-only $\alpha = 1$ specialization of the AD framework: restricted to cyclic subgroups of S_p in the candidate library and to the $\alpha = 1$ corner of the calibration spectrum, with the BMG selection criterion replaced by a Bayesian posterior maximizer.

Region III: large N , target-mismatch dominates. Above the outer boundary N is large enough that the sample covariance is itself well-conditioned and admissible; the AD estimator at the BMG-selected group $\{e\}$ collapses to the sample covariance, AD-NLL and AD-MSE both produce $\alpha = 0$, and Shah at $\{e\}$ is again the sample covariance. LW’s continued shrinkage toward the scaled identity carries a fixed structural bias in this regime: the identity is an inappropriate target when the data already support an admissible estimator, and LW pays a finite per-sample penalty for not being able to back out of its fixed prior. The cleanest single-cell illustration is the FM $W = 64$, $N = 1000$ result reported in Section 4.6, where AD-NLL, AD-MSE, Shah-BMG, and the sample covariance all coincide at a held-out NLL of -466 nats per sample while LW is at -417 nats per sample, a 49-nat-per-sample loss attributable entirely to the target choice. The boundary between Regions II and III is therefore the N at which the BMG selection transitions to the trivial group and the AD family ceases to add informational content beyond the sample covariance; LW’s loss in Region III is a target-mismatch penalty, not a sample-size effect. This is the empirical content of the title.

Empirical anchors of the diagram. The six real-data experiments of Section 4 sit at distinct coordinates in this diagram. CRSP at $M = 55$, $N = 252$ is well into Region II in both the pre-COVID and COVID-era panels, with both calibrations preferred to LW and the BMG selection dominated by GICS-BLOCK in the calm post-2015-H2 and post-COVID windows. The two CRSP datasets between them produce a paired regime-conditional finding: a 5-window mild wreath cluster in 2015 H2 (pre-COVID panel, around the China-A-share crash, median bmg-margin 0.07 nats per sample) and a 22-window severe wreath cluster spanning the period when the February-April 2020 COVID crash sits inside the trailing 252-day training window (COVID-era panel, median margin 0.15 nats per sample, with a single-window margin of 1.37 at window 4 that is the largest single-window selection margin in any experiment in the paper). In both clusters BMG returns to GICS-BLOCK once the correlation event exits the trailing window. The cross-validated $\hat{\alpha}_{\text{NLL}}^*$ confirms

an interior operating point in both panels: approximately 0.50 pre-COVID and approximately 0.33 in the COVID-era panel where the higher training-window noise floor pushes the calibration toward the sample covariance. OISST at $M = 64$, $N = 252$ is also in Region II for both regional patches, with $\hat{\alpha}_{\text{NLL}}^* \approx 0.05$ on midocean (matched-limit regime, almost no shrinkage needed) and ≈ 0.43 on gulfstream (interior); an earlier OISST library extension also illustrates a clean negative library-bias result, as the two high-order Cartesian and wreath candidates added for parity with the CRSP and RadioML libraries are rejected by BMG on every one of the 148 windows in favor of the existing low-order candidates. TCGA-BRCA at $M = 100$, $N = 50$ is the few-shot regime in the paper, sitting in the *bias-variance interior* of the α -axis with calibrated $\hat{\alpha}_{\text{NLL}}^*$ at mean 0.51 across the 50 splits and range $[0.43, 0.58]$. The an earlier library extension introduced two high-order pathway-aware candidates (Cartesian and wreath on the PC1-loading within-pathway ordering); BMG selects the within-pathway-exchangeable PATHWAY-BLOCK candidate (S_{20}^5 , $|G| = (20!)^5$) on 46 of the 50 splits and the within-pathway-cyclic Cartesian candidate Z-K-PC1-CARTESIAN (\mathbb{Z}_{20}^5 , $|G| = 20^5$) on the remaining 4. The wreath candidate Z-K-PC1-WREATH ($\mathbb{Z}_{20} \wr S_5$, $|G| \approx 3.84 \times 10^8$) is admitted by the Tier 1 prefilter on every split but selected on none, consistent with the biological observation that the five MSigDB Hallmark pathways used in this experiment carry distinct functional identities and are not freely exchangeable as units. The cross-pathway exchangeability that the wreath candidate would encode is therefore correctly rejected; the within-pathway exchangeability of PATHWAY-BLOCK is biologically appropriate and BMG-selected. The four splits where Z-K-PC1-CARTESIAN is preferred are tiebreaks at small CV-NLL margin between two candidates that share the within-pathway PC1 basis but differ on the strength of the within-pathway exchangeability assumption. The most informative methodological finding from this dataset is the *failure* of the Shah-style $\alpha = 1$ commitment at the BMG-selected target: Shah-BMG *performs worse than LW* by 13.2 nats per sample (paired $t = +54.5$), because at this $(M, N) = (100, 50)$ regime the matched-fit residual at the pathway-block target is large enough that the $\alpha = 1$ projection-only commitment over-shrinks the data by more than the BMG-projection benefit can compensate for. Only the calibrated AD estimator with $\hat{\alpha}_{\text{NLL}}^* \approx 0.51$ recovers the right amount of sample-covariance information to bring the estimator -3.98 nats below LW; this is the cleanest single-dataset demonstration in the paper that the Shah-style commitment can be the wrong choice even when the BMG-selected target is correct. An independent SYNTHETIC validation (Section 4.5) confirms that BMG can detect $\mathbb{Z}_{20} \wr S_5$ when it is the population symmetry: on synthetic wreath-structured data the BMG procedure selects Z-K-PC1-WREATH on 44 of 50 splits, validating that the absence of wreath selection on real BRCA is a genuine negative finding about the data rather than a procedural failure. RadioML spans the entire diagram: at $M = 32$, $N = 1000$ the digital modulations are firmly in Region II, while at $M = 128$, $N = 50$ the same modulations are deep in Region I (the 120-nat AD-NLL versus AD-MSE gaps cited above), and the FM cells at large N exhibit the Region III collapse. Galaxy10 cleanly spans the Region I-to-II transition at fixed M across three distinct BMG-selection regimes: at $M = 256$ the $N \in \{50, 100, 200\}$ cells are deep in Region I (the 191-nat AD-MSE-vs-AD-NLL gap at $N = 200$ is the canonical exhibit, with BMG selecting the v3p9-extension high-order Cartesian Z-ROW-INDEP-COLS on 250 of 250 trials); the $N = 500$ cell sits at the Region I/II boundary where the BMG selection sharply transitions from Z-ROW-INDEP-COLS to D_4 , with D_4 preferred on 250 of 250 trials at median bmg-margin 8.0 nats per sample (the strongest declarative selection in the paper); and $N = 1000$ is firmly in Region II with D_4 selected at every trial. The breadth of RadioML’s coverage of the entire diagram and the depth of Galaxy10’s coverage of the Region I-to-II transition are complementary: RadioML traces the diagram’s full extent at varying $|G|$, and Galaxy10 traces the inner-boundary crossing in detail at fixed M . CIFAR-10 at $M = 256$, $N = 4,000$ per class is firmly in Region II within each class where the candidate library is highly informative; the per-class $\hat{\alpha}_{\text{NLL}}^*$ values in $[0.65, 0.975]$ confirm an interior-but-large- α operating point

on this dataset, where the structural prior is strong enough that AD-NLL-BMG has lower NLL than LW on every one of the ten classes (paired $t = -15.21$). Together CIFAR-10 and Galaxy10 cover the image-data axis of the diagram at two complementary operating points: Galaxy10 traces the Region I-to-II transition at small N on a D_4 -rich domain, and CIFAR-10 demonstrates the framework’s discriminative selection across natural-image classes at large N on a recognizable benchmark.

Library-specification bias as an irreducible source of error. The BMG-selected estimator is bounded above in held-out NLL by the best member of the candidate library \mathcal{L} , and population symmetries that lie outside \mathcal{L} are invisible to the procedure. This is an irreducible source of bias that no within-library diagnostic can detect: the cross-validated calibration identifies the best candidate among those supplied, but cannot identify a better candidate that was not. The default convention of including the trivial group and S_M at the library extrema bounds the worst case, since the AD estimator collapses to the sample covariance at the trivial group when no structural prior carries net informational content, and to the compound-symmetry projection at S_M when the data support the maximum-shrinkage target. Within those extrema the BMG procedure is bounded above by the best non-trivial prior the analyst supplied, which is itself bounded above by what an omniscient analyst would supply. This is the price of any prior-conditional procedure and applies symmetrically to LW (whose fixed scaled-identity target is itself a structural prior the analyst chose) and to any covariance estimator that imposes structure for variance reduction. Two operational consequences follow. First, if S_M is preferred on a substantial fraction of trials in cells where the Tier 1 prefilter admits at least one structured candidate of order strictly less than $|S_M|$, the BMG is using S_M as the maximum-shrinkage fallback rather than as a structural fit; the analyst should consider whether the library is missing a candidate that better matches the population symmetry. The Galaxy10 results of Section 4.7 are consistent with the well-specified case: S_M dominates at small N where Tier 1 prefilter excludes the small- $|G|$ candidates, but D_4 dominates at moderate-to-large N where the data resolve the population symmetry. Second, trivial-group selection in large- N cells is not a misspecification signal; it is the correct fallback when the data do not support any structural prior over the sample covariance, and indicates that the AD estimator has correctly fallen back to the sample covariance. The FM windows of Section 4.6 at $N = 1000$ exhibit this Region III behavior. A third concrete example, complementary to the two above, is the OISST high-order rejection of Section 4.4: the two high-order candidates introduced in an earlier version of this manuscript are admitted by Tier 1 in both OISST regions, evaluated by Tier 2 BMG on equal footing with the existing low-order candidates, and rejected on all 148 windows by a margin well outside the fold-noise scale. The diagnostic distinguishes this case from a misspecification alarm because the rejected candidates are the high-order ones, not S_M : the data simply do not support sector-level structural priors at this (M, N) regime, and BMG correctly defers to the low-order candidates that the data do support. The conditional structure of the diagnostic is essential: unconditional S_M dominance can reflect Tier 1 prefilter exclusions (correct behavior at small N) or library misspecification (alarm at moderate-to-large N), and only the within-library admission record distinguishes the two. A fourth concrete example, complementary to the OISST negative result above, is the TCGA-BRCA wreath dominance of Section 4.5: an earlier library extension that added the wreath candidate displaced an earlier PATHWAY-BLOCK selection on 38 of 50 above-noise splits, with the calibrated shrinkage intensity saturating near $\alpha = 1$ at the wreath. This is the positive complement of the OISST negative result: when the high-order candidate is well-matched to the population symmetry, BMG selects it and the data prefer the projection target itself without sample-covariance admixture. Across the four real-data experiments where an earlier library extension was applied (CRSP, OISST, TCGA-BRCA, and RadioML) an earlier extension produced one mixed positive (CRSP, with regime-conditional

wreath selection on the 2015 H2 cluster), one clean negative (OISST, both high-order candidates rejected on every window), one strong positive (TCGA-BRCA, wreath selected on every above-noise split), and one structural-no-op (RadioML, where the wreath was already in the library at an earlier with selections on AM-DSB-SC). The diagnostic operates correctly across the full range of outcomes, and the negative result is as informative as the positive one.

6 Conclusion

This paper has developed a class of symmetry-aware convex shrinkage estimators for high-dimensional covariance estimation. The estimator replaces the scaled identity target of the Ledoit-Wolf 2004 shrinkage estimator with a Reynolds projection of the sample covariance under a finite symmetry group, with the group selected from a candidate library by held-out predictive performance. The construction generalizes both the Ledoit-Wolf 2004 estimator (which targets the scaled identity) and the group-symmetric maximum-likelihood estimator of Shah and Chandrasekaran (which targets a fixed projection under a prespecified group), and is calibrated by either a closed-form Frobenius mean-squared-error plug-in or a held-out negative log-likelihood minimizer.

The theoretical contributions are a bias-variance orthogonal parametrization of the convex shrinkage family in the (α, G) -plane, a closed-form Wishart asymptotic crossover that exhibits the leading-order $O(1/N)$ correction between the mean-squared-error and negative-log-likelihood optima, a finite-sample regret bound for the held-out calibration, an oracle inequality for the data-driven group selection, a quantitative sufficient-match condition under which the proposed estimator dominates Ledoit-Wolf shrinkage in Frobenius mean-squared error, and minimax rate results that locate the proposed estimator on the rate ladder under various smoothness and sparsity conditions on the population covariance.

The empirical evaluation spans six real-data covariance estimation problems whose candidate libraries are built from domain-specific structural priors: financial returns on the constituents of the Standard and Poor’s 500 in two regimes (a calm period and a COVID-era stress period), sea-surface temperature anomalies from the National Oceanic and Atmospheric Administration’s optimum interpolation product, gene expression covariances for breast invasive carcinoma from The Cancer Genome Atlas, intermediate-frequency radio signal covariances from the RadioML 2018.A benchmark, galaxy image covariances from the Galaxy10 DECaLS dataset, and natural image-patch covariances from CIFAR-10 with a distribution-shift companion on CIFAR-10.1. The empirical evaluation also includes a decoy stress test of the BMG procedure that confirms its robustness to deliberately mismatched candidate-library entries, and a synthetic-data empirical comparison against the Bayesian permutation-symmetry estimator of Chojecki and colleagues.

The empirical and theoretical findings synthesize into a three-region phase diagram in $(N, M, |G|, \delta)$ coordinates that predicts which estimator is preferred in which regime. In the few-shot Region I, structural priors carry the most information per observation and the proposed estimator improves substantially on Ledoit-Wolf shrinkage. In the bias-variance interior of Region II, the calibrated convex shrinkage adapts to the structural match quality and trades bias against variance at a rate that depends on the library specification. In Region III, where the sample size is large enough that the unstructured sample covariance is itself near-optimal, the structural prior carries little additional information per observation, and Ledoit-Wolf shrinkage remains the appropriate baseline. The procedure recommended by the present work is therefore conservative: it improves on Ledoit-Wolf shrinkage in the regimes where a structural prior is informative, and reverts to Ledoit-Wolf shrinkage otherwise. The dominance condition makes this conservatism explicit; the empirical anchors locate it across a representative range of real-data covariance estimation problems.

7 Code and data availability

The code that supports the empirical results of Section 4 is bundled with this manuscript and will be archived in a public repository at the time of formal publication. The bundle organizes the code along the four lines of empirical activity: data preparation (one script per dataset that produces the centered observation matrix from the externally available raw source), per-experiment estimator evaluation (one script per dataset that runs the cross-validation, candidate-library evaluation, and BMG selection at the operating-point (N, M)), the protocol sweep evaluation (one script per dataset that sweeps N_{train} at fixed M and aggregates the held-out negative log-likelihood across cells), and figure regeneration (one script per figure that re-renders the figure from the cached cross-validation results).

The LW-NL nonlinear-shrinkage implementation is in a separate module that is imported by both LW-NL and the AD-LW-NL composition. The module computes the closed-form Hilbert transform of the Epanechnikov-kernel density estimate of the sample eigenvalue distribution following [Ledoit and Wolf \[2020\]](#) and applies the rank-aware regularization for the boundary case $c \geq 1$. The implementation has been verified against synthetic Marchenko-Pastur benchmarks at three values of the concentration ratio and reproduces the analytical predictions of the asymptotic formulas to within standard numerical tolerances.

The six datasets used in this paper are externally sourced. The Standard and Poor’s 500 daily-return data is from the Center for Research in Security Prices via Wharton Research Data Services (subscription required); the construction of the balanced panel of constituents follows the script bundled with this paper. The NOAA Optimum Interpolation Sea Surface Temperature data is publicly available from the National Oceanic and Atmospheric Administration; the spatial-patch extraction script bundled with this paper documents the midocean and gulfstream region selections used here. The TCGA-BRCA RNA-seq data is publicly available through the Xena Browser of [Goldman et al. \[2020\]](#); the hallmark gene-set encoding follows [Liberzon et al. \[2015\]](#). The RadioML 2018.A intermediate-frequency radio data is publicly available from [O’Shea et al. \[2018\]](#). The Galaxy10 DECaLS image data is publicly available from [Leung and Bovy \[2021\]](#). The CIFAR-10 and CIFAR-10.1 natural-image datasets are publicly available from [Krizhevsky \[2009\]](#) and [Recht et al. \[2019\]](#) respectively. Reproduction notes for each dataset are in the script docstrings.

References

- Steen Arne Andersson. Invariant normal models. *The Annals of Statistics*, 3(1):132–154, 1975.
- Steen Arne Andersson and Jørgen Madsen. Symmetry and lattice conditional independence in a multivariate normal distribution. *The Annals of Statistics*, 26(2):525–572, 1998.
- Zhidong Bai and Jack W. Silverstein. *Spectral Analysis of Large Dimensional Random Matrices*. Springer, 2nd edition, 2010.
- Peter J. Bickel and Elizaveta Levina. Covariance regularization by thresholding. *Annals of Statistics*, 36(6):2577–2604, 2008a. doi: 10.1214/08-AOS600.
- Peter J. Bickel and Elizaveta Levina. Regularized estimation of large covariance matrices. *Annals of Statistics*, 36(1):199–227, 2008b. doi: 10.1214/009053607000000758.
- Tony Cai and Weidong Liu. Adaptive thresholding for sparse covariance matrix estimation. *Journal of the American Statistical Association*, 106(494):672–684, 2011. doi: 10.1198/jasa.2011.tm10560.

- Tony T. Cai and Harrison H. Zhou. Optimal rates of convergence for sparse covariance matrix estimation. *Annals of Statistics*, 40(5):2389–2420, 2012. doi: 10.1214/12-AOS998.
- Center for Research in Security Prices. CRSP US Stock Database. Center for Research in Security Prices, Booth School of Business, The University of Chicago. Distributed via Wharton Research Data Services (WRDS), <https://wrds-www.wharton.upenn.edu/>, 2024.
- Yilun Chen, Ami Wiesel, Yonina C. Eldar, and Alfred O. Hero. Shrinkage algorithms for MMSE covariance estimation. *IEEE Transactions on Signal Processing*, 58(10):5016–5029, 2010. doi: 10.1109/TSP.2010.2053029.
- Adam Chojecki, Paweł Morgen, and Bartosz Kołodziejek. Learning permutation symmetry of a Gaussian vector with gips in R. *Journal of Statistical Software*, 112(7):1–38, 2025. doi: 10.18637/jss.v112.i07.
- A. P. Dempster. Covariance selection. *Biometrics*, 28(1):157–175, 1972.
- Persi Diaconis. Group representations in probability and statistics. In *Lecture Notes – Monograph Series*, volume 11. Institute of Mathematical Statistics, 1988.
- Jerome Friedman, Trevor Hastie, and Robert Tibshirani. Sparse inverse covariance estimation with the graphical lasso. *Biostatistics*, 9(3):432–441, 2008.
- William Fulton and Joe Harris. *Representation Theory: A First Course*, volume 129 of *Graduate Texts in Mathematics*. Springer, 1991.
- Mary J. Goldman, Brian Craft, Mim Hastie, Kristupas Repečka, Fran McDade, Akhil Kamath, Ayan Banerjee, Yunhai Luo, Dave Rogers, Angela N. Brooks, Jingchun Zhu, and David Haussler. Visualizing and interpreting cancer genomics data via the Xena platform. *Nature Biotechnology*, 38(6):675–678, 2020. doi: 10.1038/s41587-020-0546-8.
- Gene H. Golub and Charles F. Van Loan. *Matrix Computations*. Johns Hopkins University Press, 4th edition, 2013.
- Piotr Graczyk, Hideyuki Ishi, Bartosz Kołodziejek, and H el ene Massam. Model selection in the space of Gaussian models invariant by symmetry. *The Annals of Statistics*, 50(3):1747–1774, 2022. doi: 10.1214/22-AOS2174.
- L. R. Haff. Empirical Bayes estimation of the multivariate normal covariance matrix. *The Annals of Statistics*, 8(3):586–597, 1980.
- S oren H ojsgaard and Steffen L. Lauritzen. Graphical Gaussian models with edge and vertex symmetries. *Journal of the Royal Statistical Society Series B*, 70(5):1005–1027, 2008. doi: 10.1111/j.1467-9868.2008.00666.x.
- Roger A. Horn and Charles R. Johnson. *Matrix Analysis*. Cambridge University Press, 2nd edition, 2012.
- Boyin Huang, Chunying Liu, Viva Banzon, Eric Freeman, Garrett Graham, Bill Hankins, Tom Smith, and Huai-Min Zhang. Improvements of the Daily Optimum Interpolation Sea Surface Temperature (DOISST) Version 2.1. *Journal of Climate*, 34(8):2923–2939, 2021. doi: 10.1175/JCLI-D-20-0166.1.
- Gordon James and Adalbert Kerber. *The Representation Theory of the Symmetric Group*, volume 16 of *Encyclopedia of Mathematics and Its Applications*. Addison-Wesley, 1981.

- Søren Tolver Jensen. Covariance hypotheses which are linear in both the covariance and the inverse covariance. *The Annals of Statistics*, 16(1):302–322, 1988.
- Alex Krizhevsky. Learning multiple layers of features from tiny images. Technical Report, University of Toronto, 2009. The CIFAR-10 dataset of 60,000 32x32 colour images in 10 mutually exclusive classes (airplane, automobile, bird, cat, deer, dog, frog, horse, ship, truck), with 6,000 images per class.
- Olivier Ledoit and Michael Wolf. A well-conditioned estimator for large-dimensional covariance matrices. *Journal of Multivariate Analysis*, 88(2):365–411, 2004. doi: 10.1016/S0047-259X(03)00096-4.
- Olivier Ledoit and Michael Wolf. Nonlinear shrinkage estimation of large-dimensional covariance matrices. *Annals of Statistics*, 40(2):1024–1060, 2012. doi: 10.1214/12-AOS989.
- Olivier Ledoit and Michael Wolf. Analytical nonlinear shrinkage of large-dimensional covariance matrices. *Annals of Statistics*, 48(5):3043–3065, 2020.
- Henry W. Leung and Jo Bovy. Galaxy10 DECaLS dataset. <https://astronn.readthedocs.io/en/latest/galaxy10.html>, 2021. Open-access dataset of 17,736 colored galaxy images at 256x256 resolution across 10 morphological classes, sourced from the DESI Legacy Imaging Surveys (BASS, DECaLS, MzLS) with labels from the Galaxy Zoo collaboration. HuggingFace mirror at [matthieulel/galaxy10_decals](https://huggingface.co/matthieulel/galaxy10_decals).
- Arthur Liberzon, Chet Birger, Helga Thorvaldsdóttir, Mahmoud Ghandi, Jill P. Mesirov, and Pablo Tamayo. The Molecular Signatures Database Hallmark gene set collection. *Cell Systems*, 1(6):417–425, 2015. doi: 10.1016/j.cels.2015.12.004.
- Karim Lounici. High-dimensional covariance matrix estimation with missing observations. *Bernoulli*, 20(3):1029–1058, 2014.
- V. A. Marchenko and L. A. Pastur. Distribution of eigenvalues for some sets of random matrices. *Mathematics of the USSR-Sbornik*, 1(4):457–483, 1967. doi: 10.1070/SM1967v001n04ABEH001994.
- Timothy J. O’Shea, Tamoghna Roy, and T. Charles Clancy. Over-the-air deep learning based radio signal classification. *IEEE Journal of Selected Topics in Signal Processing*, 12(1):168–179, 2018. doi: 10.1109/JSTSP.2018.2797022.
- Mohsen Pourahmadi. *High-Dimensional Covariance Estimation: With High-Dimensional Data*. Wiley, 2013.
- Benjamin Recht, Rebecca Roelofs, Ludwig Schmidt, and Vaishaal Shankar. Do CIFAR-10 classifiers generalize to CIFAR-10? In *Proceedings of the 36th International Conference on Machine Learning (ICML)*, pages 5389–5400, 2019. Introduces the CIFAR-10.1 reproduction test set, drawn from the same Tiny Images source as CIFAR-10 with a different keyword and curation procedure designed to minimize the distribution shift relative to the original test set. Classifier accuracy consistently degrades by 4–10 percentage points across a wide range of architectures, establishing CIFAR-10.1 as a meaningful (if mild) distribution-shift benchmark.
- Richard W. Reynolds, Thomas M. Smith, Chunying Liu, Dudley B. Chelton, Kenneth S. Casey, and Michael G. Schlax. Daily high-resolution-blended analyses for sea surface temperature. *Journal of Climate*, 20(22):5473–5496, 2007. doi: 10.1175/2007JCLI1824.1.

- Juliane Schäfer and Korbinian Strimmer. A shrinkage approach to large-scale covariance matrix estimation and implications for functional genomics. *Statistical Applications in Genetics and Molecular Biology*, 4(1), 2005. Article 32.
- Jean-Pierre Serre. *Linear Representations of Finite Groups*, volume 42 of *Graduate Texts in Mathematics*. Springer, 1977.
- Parikshit Shah and Venkat Chandrasekaran. Group symmetry and covariance regularization. *Electronic Journal of Statistics*, 6:1600–1640, 2012. doi: 10.1214/12-EJS723.
- Ilya Soloveychik, Dmitry Trushin, and Ami Wiesel. Group symmetric robust covariance estimation. *IEEE Transactions on Signal Processing*, 64(1):244–257, 2016. doi: 10.1109/TSP.2015.2486739.
- Charles Stein. Inadmissibility of the usual estimator for the mean of a multivariate normal distribution. In *Proceedings of the Third Berkeley Symposium on Mathematical Statistics and Probability*, volume 1, pages 197–206. University of California Press, 1956.
- Charles Stein. Lectures on the theory of estimation of many parameters. *Journal of Soviet Mathematics*, 34:1373–1403, 1986. doi: 10.1007/BF01085007.
- Charles M. Stein. Estimation of the mean of a multivariate normal distribution. *The Annals of Statistics*, 9(6):1135–1151, 1981.
- The Cancer Genome Atlas Network. Comprehensive molecular portraits of human breast tumours. *Nature*, 490(7418):61–70, 2012. doi: 10.1038/nature11412.
- Mitchell A. Thornton. Algebraic diversity for high-dimensional covariance estimation, 2026a.
- Mitchell A. Thornton. Algebraic diversity for spectral estimation, 2026b.
- Roman Vershynin. *High-Dimensional Probability: An Introduction with Applications in Data Science*, volume 47 of *Cambridge Series in Statistical and Probabilistic Mathematics*. Cambridge University Press, 2018.
- Martin J. Wainwright. *High-Dimensional Statistics: A Non-Asymptotic Viewpoint*. Cambridge University Press, 2019.
- Joong-Ho Won, Johan Lim, Seung-Jean Kim, and Bala Rajaratnam. Condition-number-regularized covariance estimation. *Journal of the Royal Statistical Society Series B*, 75(3):427–450, 2013.